UNIVERSITA' DEGLI STUDI DI PADOVA
Dipartimento di Ingegneria Industriale DII
Corso di Laurea Magistrale in Ingegneria Aerospaziale

Implementation and validation of a numerical model for dynamic stall simulation in helicopter airfoils

Autore:	Christopher Ciavarella
Numero di matricola:	1020318
Relatore:	Ernesto Benini
Correlatore:	Dominik Schicker

April 2013

Statement of Authorship

I, Christopher Ciavarella, confirm that the work presented in this thesis has been performed and interpreted solely by myself except where explicitly identified to the contrary. All verbatim extracts have been distinguished by quotation marks, and all sources of information have been specifically acknowledged. I confirm that this work has not been submitted elsewhere in any other form for the fulfillment of any other degree or qualification.

Garching, Wednesday 10th April, 2013

Abstract

Dynamic stall is one of the most complex aerodynamic phenomenon and it affects the performance of a wide variety of fluid machinery. The loading of an airfoil during dynamic stall can be evaluated in terms of an extra lift and a related increase in drag and negative pitching moment. Although main features of dynamic stall have been identified, a computational prediction is still a challenging task. Previous works show a lack of reliability and accuracy in the development of a stable CFD prediction model, mainly due to the large computational effort in terms of cost and time, as well as a need of in-depth analysis of the ideal spatial and temporal discretization. In the present work the purpose is the implementation and validation of a numerical model for an accurate prediction of airloads on a bidimensional airfoil (OA209) under dynamic stall, using the DLR TAU code. Accuracy and reliability of the solution are the two key points on which this thesis focuses on. First, CFD validation is performed under steady conditions, pointing out the importance of grid generation and the influence of various solver parameters. Results are obtained with both Spalart-Allmaras turbulence model and Reynolds Stress Model. Then, unsteady computations, preceeded by temporal resolution studies, reveals the need of several changes in the modelling approach, in order to have an accurate prediction. Examining in depth the phenomenon, a further step to improve prediction accuracy is the adoption of a model which takes into account also the boundary layer transition. With this purpose, the recent developed four-equations γ-Re_θ transition model is adopted, leading to new interesting considerations.

Estratto

Lo stallo dinamico è uno dei fenomeni aerodinamici più complessi e influenza le prestazioni di un'ampia varietà di macchine a fluido. Durante lo stallo dinamico, valutando il carico sul profilo alare si può notare la presenza di un extra portanza, con un conseguente aumento di resistenza e diminuzione del momento torcente. Sebbene molte caratteristiche dello stallo dinamico siano state già identificate, una previsione numerica rimane un compito altamente impegnativo. I precedenti studi nel campo hanno evidenziato una mancanza di affidabilità e accuratezza nello sviluppo di un modello CFD, principalmente a causa del grande sforzo computazionale richiesto in termini di costo e tempo, così come la necessità di un'analisi approfondita della perfetta risoluzione spaziale e temporale. Nella presente opera, lo scopo è l'implementazione e la validazione di un modello numerico per un'accurata previsione dei carichi aerodinamici su un profilo bidimensionale (OA209) in condizioni di stallo dinamico, utilizzando il software DLR TAU. L'accuratezza e l'affidabilità della soluzione sono i due punti chiavi sui quali questa tesi si focalizza. In primo luogo, viene eseguita una validazione CFD in condizione statiche, facendo notare l'importanza della generazione della mesh e l'influenza di diversi parametri del solutore. I risultati sono ottenuti utilizzando entrambi i modelli di turbolenza Spalart-Allmaras e Reynolds Stress Model. Quindi, le simulazioni non stazionarie, precedute da uno studio sulla risoluzione temporale, rivelano la necessità di ulteriori cambiamenti nell'approcio di modellazione del fenomeno. Tale variazioni sono indispensabili per ottenere una previsione ad alta accuratezza. Infine, analizzando a fondo il fenomeno aerodinamico, risulta chiaro come sia necessario utilizzare un modello che tenga conto anche della transizione all'interno dello strato limite. A tal fine è stato adottato il modello a quattro equazione γ-Re_θ di recente sviluppo, portando a nuove interessanti considerazioni.

Contents

Abbreviations and Symbols

Abbreviations

DES	Detached Eddy Simulations
DLR	German Aerospace Centre
LEV	Leading Edge Vortex
LEVOG	Leading Edge Vortex Generator
LU-SGS	Lower-Upper Symmetric Gauss-Seidel
ONERA	French Aerospace Lab
RANS	Reynolds-averaged Navier-Stokes
RSM	Reynolds Stress Model
SAE	Spalart-Allmaras Model with Edwards modification
SAM	Spalart-Allmaras Model
SARC	Spalart-Allmaras model with rotational correction
SIMCOS	Advanced Simulation and Control of Dynamic Stall
SST	Shear Stress Transport

List of symbols

C_L	mean blade lift coefficient
C_T	blade thrust coefficient
F_{length}	function to control transition length
Ma	Mach number
O	centre of rotation
R	blade radius
Re	Reynolds number
$Re_{\theta c}$	momentum thickness Reynolds number where the intermittency starts to increase

$Re_{\theta t}$	momentum thickness Reynolds number where the skin friction starts to increase
T	temperature
T_b	blade thrust
T_{cycle}	period fo the oscillating cycle
Tu	turbulence intensity near the airfoil
Tu_{ff}	turbulence intensity at the farfield boundary
U_∞	freestream velocity
V	forward flight speed
V_T	hover tip speed
Δt	time step size
α	angle of attack or AoA
α_0	mean angle of attack
α_L	amplitude of oscillation
η	advance ratio
γ	intermittency
μ	molecular viscosity
μ_t	turbulent viscosity
$\overline{R}$	gas constant
ψ	azimuth angle
ρ	density
σ	solidity; standard deviation
τ_ω	wall shear stress
b	blade span
c	chord length
c_W	torsional damping factor or D.F.
c_d	section drag coefficient
c_f	skin friction coefficient
c_l	section lift coefficient
c_m	section pitching moment coefficient
e	root cutout ratio
f	frequency
k	reduced frequency
n	number of blades
n_t	number of time steps
r	blade radial location
y^+	dimensionless wall distance

List of Figures

List of Tables

1 Introduction

The term "dynamic stall" refers to unsteady flow separation occuring on aerodynamic bodies, such as airfoils and wings, which execute an unsteady motion. This phenomenom has been widely known to significantly affect the performance of a large variety of fluid machinery, as for example helicopters, highly manoeuvrable fighters, gas turbines and wind turbines. In all cases dynamic stall is a limiting factor for high speed and maneuver flight capabilities or power production.
As LEISHMAN states in his book [39] "dynamic stall occurs on any airfoil or other lifting suface when it is subjected to time-dependent pitching, plunging or vertical translation, or other type of non-steady motion, that takes the effective angle of attack (AoA or α) above its normal static stall angle". In this context, the physics of the flow and the development of stall show a completely different evolution compared to static conditions. This difference is caused by the rapid variation of the incidence experienced by the airfoil, and the first effect is a delay in the onset of the flow separation. The delay results in higher AoA encountered by the airfoil and leads to a substantially favorable larger lift for a short period of time than can be obtained in steady state. The flow around the leading edge allows the initialization, growth, convection and shedding of an intense vortex disturbance, known as Leading Edge Vortex (LEV). As long as this vortex remains over the airfoil suction side, it enhances the lift produced. Yet, this vortex is not stable and grows quickly along the upper surface. Short time later it sheds into the wake, causing a rapid aft movement of the center of pressure. The undesirable effect described results in a suddenly breakdown in lift (c_l) and pitching moment (c_m) and a rapid increase in drag (c_d). This represents the main adverse characteristic of dynamic stall. During the downstroke phase of the pitching cycle, a secondary vortex forms and causes a new peak in the lift, referred to as *second stall*, but this event has received little attention until now. After the second peak, the decrease of AoA and the subsequent reattachment shows hysteresis loops in the aerodynamic coefficients versus α, due to the strong irreversibility of the phenomenon. Finally, the boundary layer generally attaches from front to rear and the aerodynamic coefficients return to unstalled values.

Although many studies have been published recently about this topic, the details of dynamic stall flow characteristics are not fully unterstood yet, mainly due to its strongly nonlinear unsteadiness. Many extensive experiments have been performed by different researchers, and the shedding of LEV has been well represented in many works. Most important, it has been found that the flow behavior is strongly influenced by a number of parameter, such as shape of the airfoil, mean angle of attack (α_0), amplitude of oscillation (α_L), reduced frequency (k), and in particular the Reynods (Re) and Mach numbers (Ma).

Due to the complicated flow physics of the dynamic stall phenomenon, the industry has been primarily forced to use empirical and semi-empirical approaches for its prediction. Despite these methods provide good results, they are always delimited by validation with experimental data, which require extensive wind tunnel testing. Since experimental data are not easy to obtain, empirical methods can be really used under the same conditions set during previous validation procedure, leading to heavy limitations [39]. However, a more detailed knowledge of the dynamic stall effects is needed for dynamic response, aeroelastic stability and noise generation and propagation analyses. Fortunately, computational fluid dynamics has seen a rapid development during last years, thanks to advances in computational methods, computing power and improved capability in modeling turbulent and transitional flows. In spite of this, dynamic stall remains a particularly challenging problem for engineering analyses. The major difficulties result by the presence and interaction of many phenomena, each of whom is still being researched. Unsteadiness, turbulence, compressibility, flow transition from laminar to turbulent, 3D effects, large areas of separated flow, fluid-structure interaction are some of the most complex matters in CFD analyses, and all of them are involved in dynamic stall.

It is the objective of this thesis to improve two-dimensional dynamic stall prediction with computational methods. The validation of the model is performed with reference to the joint German/French project Advanced Simulation and Control of Dynamic Stall (SIMCOS) (2001) between German Aerospace Centre (DLR) and French Aerospace Lab (ONERA), which provides a good starting point for dynamic stall prediction. At the beginning of this project, it has been decided to select the ONERA 209 airfoil section as a candidate for common numerical and experimental investigations. SIMCOS investigated both low-speed and high-speed conditions, but the present thesis focuses only on one test case. In particular, the matter in hand involves a strong dynamic stall event, called *deep dynamic stall*, at Re=$1.15x10^6$ and Ma=0.31. Computational investigations are perfomed using the CFD software TAU, developed by DLR. The procedure adopted to achieve final accurate results in airloads prediction follows some fundamental steps. First, the model validation under steady conditions is performed: after grid generation and spatial resolution study, the influence of several solving parameters is pointed out. Moreover, two different approaches in turbulence modelling are compared, using the one-equation Spalart-Allmaras model and the more elaborate Reynolds Stress Model. Second, unsteadiness in the flow and airfoil motion are introduced, including temporal resolution study and leading to different changes in the model in order to reach accurate results under unsteady conditions. Then, since boundary layer transition from laminar to turbulent plays a key role in dynamic stall evolution, the γ-Re_θ transition model is adopted, figuring out the importance of transition in CFD dynamic stall prediction.

2 The Dynamic Stall Phenomenon

2.1 Flow Morphology of Dynamic Stall

It is well known that the lift properties of an airfoil are directly related with its AoA. Usually, the correlation between lift coefficients and AoA follows a quasi-linear trend, where higher AoA involves higher c_l. At a certain AoA value, referred to as *static stall angle of attack*, a further increase of incidence causes a drop in the lift and pitching moment coefficients, while the drag coefficient drastically grows. This phenomenon, well known as *static stall*, occurs, as the name suggests, when the AoA is statically increased and airloads are measured or computed at each single incidence value, without a time history. As previously mentioned, wind-tunnel experiments have shown that an airfoil oscillating in a certain range of incidence can experience an unusual trend of load coefficients, due to particular aerodynamic events occurring in the flowfield. More specifically, if the pitching motion is wide enough to exceed the static stall AoA, no stall event is noticed at this value, but the lift coefficient keeps growing and the airfoil experiences an extra-lift. This happens due to a delay in the onset of flow separation. The flow remains attached to the upper surface of the airfoil to an AoA much higher compared to what happens under quasi-steady conditions, exceeding the static stall angle and yielding a higher maximum lift. This lag in flow separation is caused by the occurence of three primary unsteady phenomena, here briefly described:

- When the AoA varies with respect of time there is an unsteady circulation, departing from leading edge and shedding into the wake at trailing edge, which leads to a reduction in lift and pressure gradients [39].

- Pressure gradients and leading edge pressure are further reduced by a positive pitch rate, due to the kinematic induced camber effect [3][11][19][20][28][46].

- Unsteady effects occur also within the boundar layer, such as flow reversals without any significant flow separation. Altough these effects are still not fully understood, they have been quantitatively examined by many authors [45][47][56][65].

Unsteady boundary layer effects and pressure gradient reductions result in delayed flow separation.

In order to present a clear description of what happens, it is often usefull to summarize the dynamic stall process in five stages as illustrated in fig. 2.1, where the arrows indicate the proceeding direction of the cycle. Firstly (1), the airfoil can exceed its static stall angle, due to the delay in the onset of flow separation described before. Hence (2), a vortex (LEV) starts to develop near the leading edge and swepts downstream across the chord, while AoA rapidly increases above the static stall value. The LEV induces a suction which provides additional lift as long as the vortex remains over the upper surface. However this is not the only effect, but the vortex shedding causes also an aft movement of the centre of pressure, resulting in significant increase in nose-down pitching moment (*moment stall*). Many researches have investigated LEV characteristics, and it has been found that its strenght and its distance from the surface influence the magnitude of the lift increase, which can be between 50% and 100% higher than the static maximum lift [39]. It has been also documented that the speed at which the LEV convects downstream is between one third and one half of the free stream velocity [2][55], and the streamwise movement depends on airfoil shape and pitch rate. When the LEV passes into the wake (3), a sudden break in the lift coefficient occurs (*lift stall*), while the drag coefficient rapidly increases and the pitching moment reaches its minimum value. Now the flow over the airfoil is fully separated (4) and remains stalled until α has decreased sufficiently to enable flow reattachment (5).

Always with reference to fig. 2.1, unsteady airloads show a large degree of flow hysteresis when plotted as function of the AoA. This behavior occurs because the flow around the airfoil is not associated to the airfoil angular configuration. Stall evolution during the incremental phase is completely different from what happens when incidence is decreasing, contrary to what occurs under static conditions. It is apparent that the AoA must decrease well below its normal static stall value to obtain a fully attached flow, due to a significant lag in the whole process, investigated by GREEN and GALBRAITH [24]. There is a general lag in the flow reorganization and a lag caused by the kinematic induced camber effect on the leading edge pressure gradient, mentioned above. The amount of hysteresis and the shape of the hysteresis loops have a highly non-linear dependence on three airfoil oscillation parameters: the mean AoA α_0, the oscillation amplitude α_L and the reduced frequency k. A good investigation about these dependences has been carried out by LEISHMAN in his book [39].

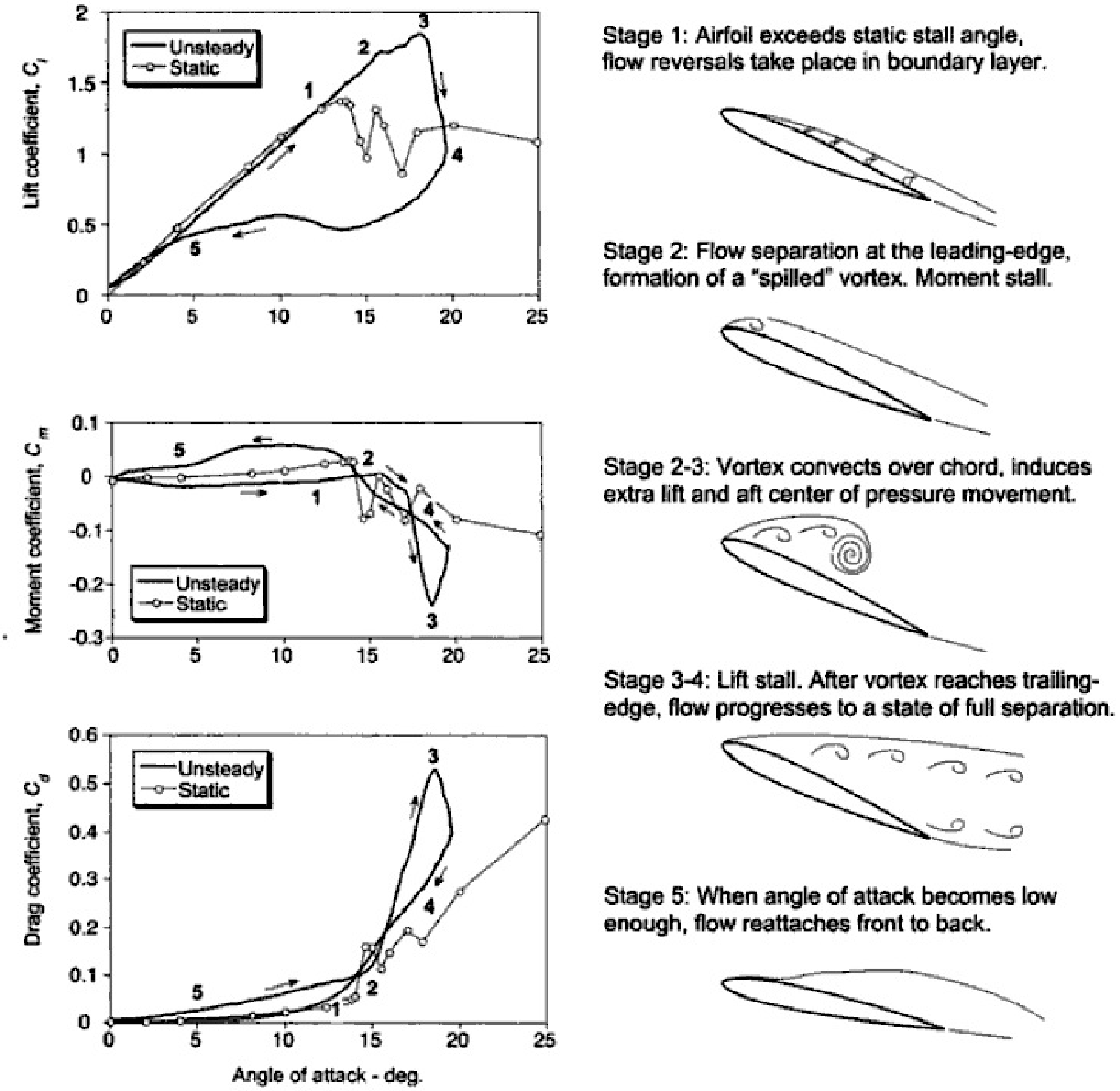

Stage 1: Airfoil exceeds static stall angle, flow reversals take place in boundary layer.

Stage 2: Flow separation at the leading-edge, formation of a "spilled" vortex. Moment stall.

Stage 2-3: Vortex convects over chord, induces extra lift and aft center of pressure movement.

Stage 3-4: Lift stall. After vortex reaches trailing-edge, flow progresses to a state of full separation.

Stage 5: When angle of attack becomes low enough, flow reattaches front to back.

Figure 2.1: Essential flow morphology and lift, drag, and moment characteristics of an airfoil during dynamic stall [39].

2.1.1 Possible Operating Modes of an Oscillating Profile

As previously mentioned, dynamic stall is influenced by some flow properties and airfoil oscillation parameters. During operating cycle, dynamic stall may occur in several ways, with different strenght and effects. Many experimental investigations [48][49] have shown that there is an evolution of flow state as AoA increases, from nominally attached conditions, through "light" dynamic stall and then into"deep" dynamic stall. Considering this, four possible operating modes have been identified, shown and numbered in fig. 2.2:

1. *No stall*: Airfoil oscillation are so small as not to cause flow separation. The airfoil behavior is well reproduced by linear theory.

2. *Stall onset*: The amplitude of airfoil oscillation gives rise to a small stall zone, which does not involve a lift drop.

3. *Light stall*: A part of the cycle involves separated flow, while in the remaining part the flow is attached to the airfoil surface and the airfoil behavior is still linear. Airfoil oscillation is high enough to cause a stronger LEV and airloads more typical of dynamic stall. In these conditions the maximum lift coefficient is not much higher than the static value but the nose-down pitching moment is more significant [39]. A clockwise loop is visible in the pitching moment curve, introducing a negative aerodynamic damping, which is the subject of the next section. Moreover, the viscous length scale remains of the order of the airfoil thickness and this dynamic stall type is more dependent by section shape and motion characteristics [42].

4. *Deep stall*: Airfoil oscillation is such that airfoil operates always under separated flow conditions, leading to larger hysteresis effects. Both increases in lift and nose-down pitching moment are very significant, and a large counterclockwise loop is introduced into the pitching moment curve giving a return to high torsional damping [39], as described further on. The viscous length scale is wider, reaching the order of the section chord, while airfoil shape and motion characteristics have less impact on deep dynamic stall [42].

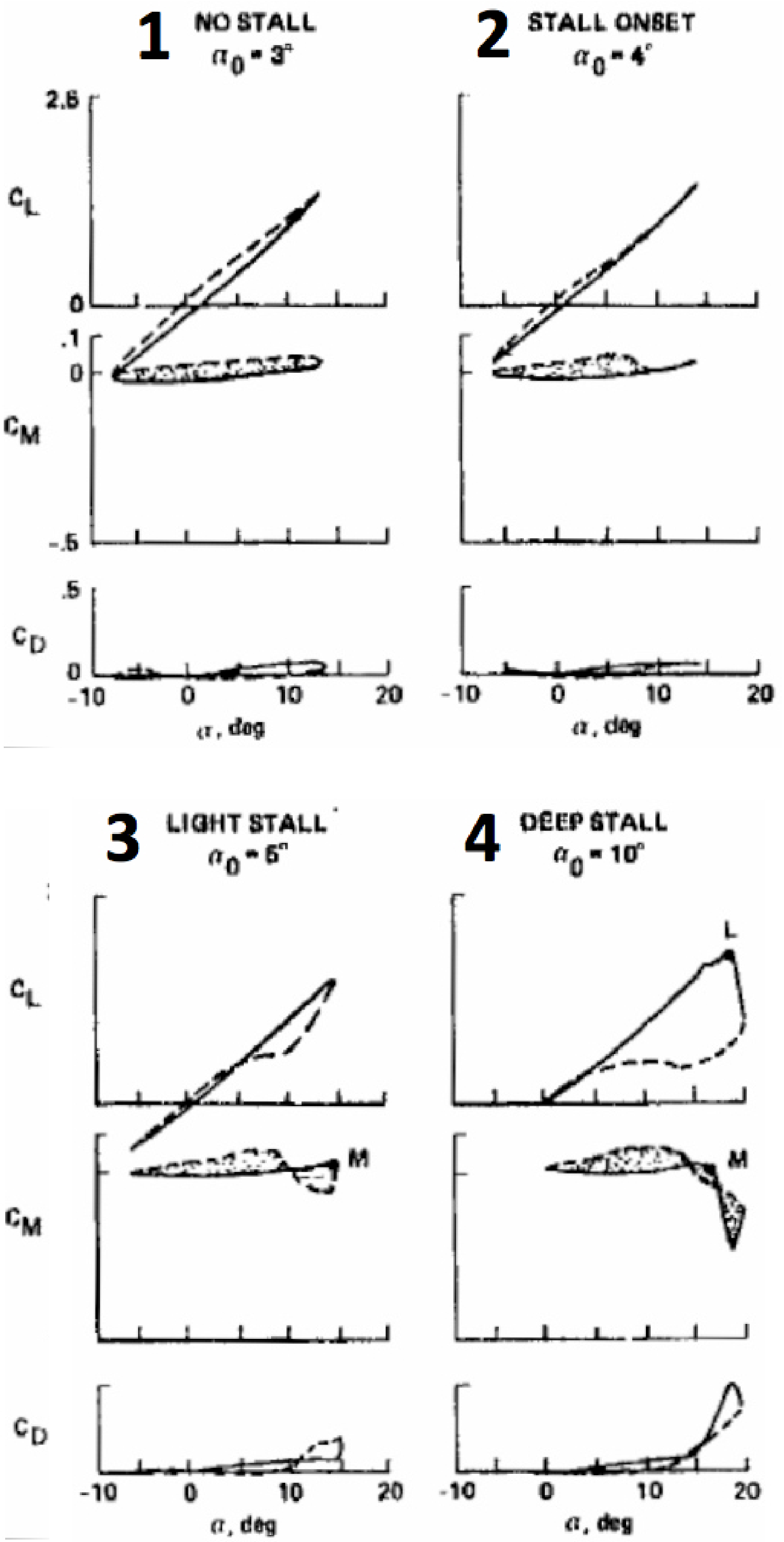

Figure 2.2: Airloads plot of different operating modes of an oscillating airfoil [48]

2.1.2 Structural Effects and Stall Flutter

This chapter has given a good overview on dynamic stall, at least regarding the fluid dynamic phenomenon. However, it has long been notice that nonlinear effects introduced by dynamic stall are associated with other structural problem, as they give rise to high blade stresses, vibrations and control loads. What researchers first observed during their experiments was that when flow separation is present, an otherwise stable elastic blade mode may become unstable, changing into a divergent or high amplitude oscillation cycle [39]. This is caused by the negative aerodynamic damping, extensively studied in literature and whose definition is the foundation of aeroelasticity. Briefly, when a structure is sourrounded by a fluid, there may occur an interaction and a related exchange of energy between structure and fluid. If a structure is vibrating in a fluid, then energy can be transferred from the structure to the fluid, acting like any other type of damping to reduce the amplitude of the motion (*positive aerodynamic damping*). Conversely, energy can be tranferred from the fluid to the structure, causing increasing vibrations (*negative aerodynamic damping*). This is commonly known as *flutter*. The causes of this nonlinear phenomenon may be different, but if vibrations are induced by flow separation occuring when an airfoil stalls, it is defined as *stall flutter*. From a structural point of view, since this structural instability is not caused by resonance between structural oscillation and dominant harmonics in the aerodynamic forcing function, typical technical solution are not available. Stall flutter cannot be eliminated by avoiding a critical structural frequency or staying away from the specific velocity related with the resonant aerodynamic frequency [21]. Stall flutter is indeed present at all frequencies where negative aerodynamic damping exists. As ERICSSON and REDING state, the only solution is to decrease the negative aerodynamic damping until it is lower in magnitude than the structural damping. In this case the structure dissipates energy at the same rate as the airstream delivers energy to the airfoil [21].

Stall flutter is a serious aeroelastic instability for rotating machineries, particularly relevant for the torsional mode. CARTA [10] refers to a torsional damping factor (c_W):

$$D.F. = c_W = \oint c_m(\alpha)\mathrm{d}\alpha \tag{2.1}$$

This factor is defined to be positive when it corresponds to a counterclockwise loop in the (c_m,α) diagram. Under this condition the fluid receives energy from airfoil movement, otherwise it transfers energy to the airfoil, promoting an aeroelastic divergence.

Although all oscillation parameters affect the torsional damping value, it has been noticed that especially mean AoA and reduced frequency influence this damping [39].

Regarding the main AoA, its increase affects the progressive change of the torsional damping. In fig. 2.3 three different airload conditions corresponding to as many mean AoA variations are illustrated. As shown in the top figure, when dynamic stall occurs a clockwise loop is introduced, which gives a negative contribution to the damping. Gradual increase in mean AoA results in a larger area of the second loop, visible in the central figure, until moment stall occurs while AoA is still increasing. Under this deep stall condition a third loop appears, clear in the last figure, this time clockwise, which contributes to recover more positive damping.

Differently, the effect of increasing the reduced frequency is observed in fig. 2.4, where three

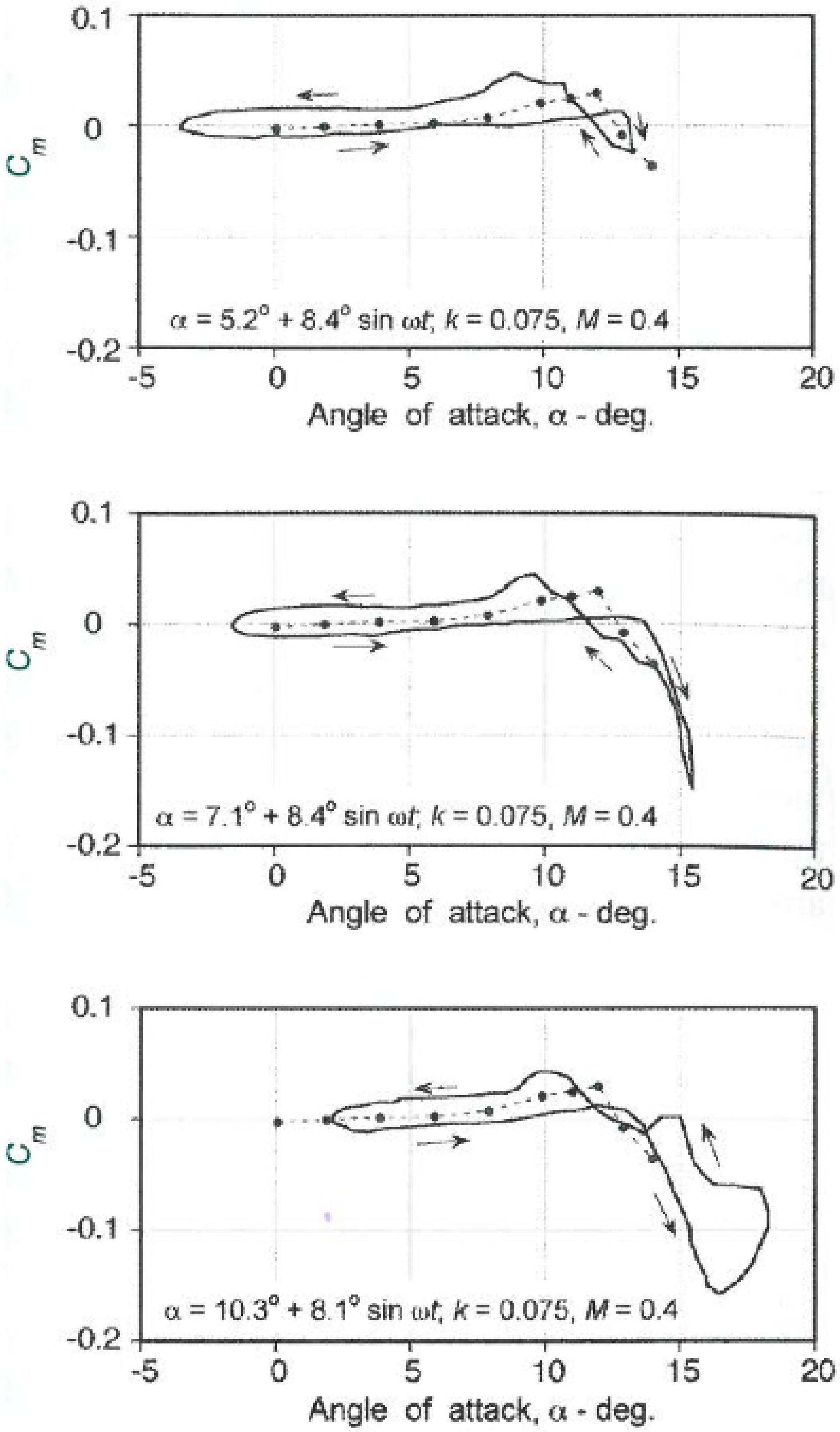

Figure 2.3: Effects of increasing mean AoA on pitching moment coefficient [39]

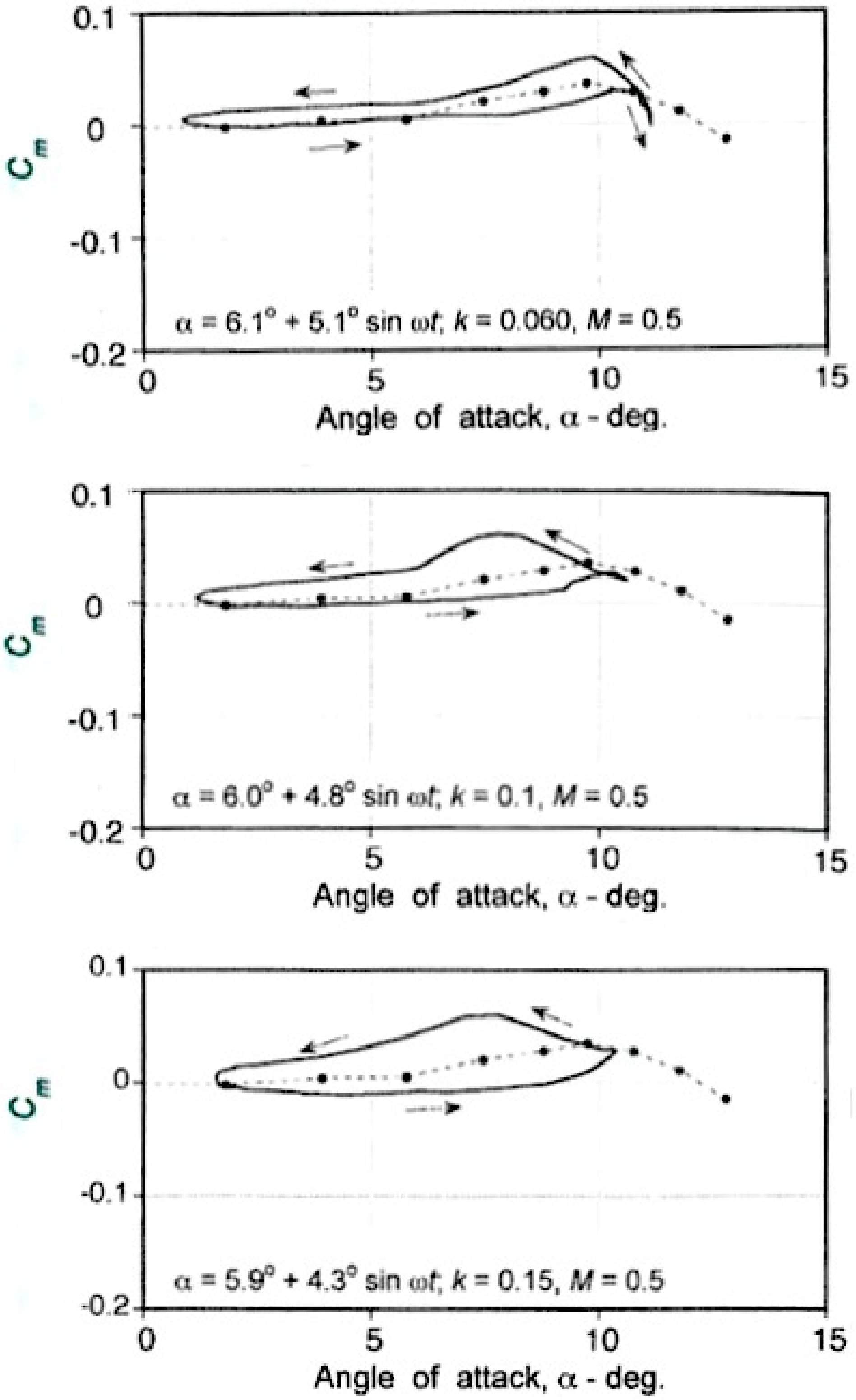

Figure 2.4: Effects of reduced frequency on the pitching moment coefficient [39]

different values of reduced frequency and their effects on c_m are illustrated. In the top figure, results are shown for a relatively low reduced frequency and for an AoA history just sufficient to produce stall onset or light dynamic stall. In the other two cases, the reduced frequency has been increased, keeping the same nominal AoA forcing. It may be noted that vortex shedding is delayed with increasing reduced frequency until it finally occurs at the maximum AoA achieved during the cycle. At the same time, also the onset of the flow reattachment is delayed, if flow separation occurs. Especially in the last figure, it is apparent that a high enough reduced frequency can be attained to prevent flow separation occurrence at any point of the cycle, with a consequent reduction of the negative damping. Moreover, this expedient can be used also if the mean AoA is increased further, by increasing in turn the reduced frequency.

2.2 The Dynamic Stall Phenomenon in Helicopter Technology

Altough the relationship between the characteristics of dynamic stall and the rapid variation of the incidence had long been observed by KRAMER [31], the importance of this phenomenon was first identified and emphasized in the helicopter community. In the 1960s helicopter design engineers were confused by the extra lift gained on the helicopter rotor in the retreating phase [69].

It is well known that the thrust of a helicopter rotor is directly related to the lift that the blade airfoil section can provide. In forward flight the thrust of one blade (T_b) can be expressed as follows [7]:

$$T_b(\psi) = \frac{1}{2}\rho c V_T^2 \int_e^R c_l(r,\psi)[\frac{r}{R} + \eta \sin\psi]^2 \, \mathrm{d}r \tag{2.2}$$

where ψ is the azimuth angle, r radial location, ρ density, V_T hover tip speed, c_l section lift coefficient, R blade radius, e root cutout ratio and η advance ratio, that is the ratio of forward flight speed to the speed of the rotor tip (η=V/V_T). The thrust of the rotor is then obtained summing all blades (n).

In hover, it is possible to define a mean blade lift coefficient (C_L) that is not dependent upon r or ψ:

$$C_L = \int_e^R c_l(r,\psi)[\frac{r}{R} + \eta \sin\psi]^2 \, \mathrm{d}r \tag{2.3}$$

Thanks to this, eq. (2.2) can be simplified as follow:

$$T_b = \frac{1}{2}\rho c V_T^2 R C_L \tag{2.4}$$

Now the blade thrust can be summed over the n blades. The classical result in terms of the blade thrust coefficient (C_T) and the solidity (σ) is obtained:

$$\frac{C_T}{\sigma} = \frac{1}{6} C_L \tag{2.5}$$

In forward flight $c_l(r,\psi)$ in eq. (2.2) is affected by the advance ratio and, with the assumption that roll moment balance must be maintained at the rotor thrust limit, the blade thrust coefficient can be expressed as

$$\frac{C_T}{\sigma} = \frac{C_L}{6} \left(\frac{1 - \eta^2 + 9\eta^4/4}{1 + 3\eta^2/2} \right) \tag{2.6}$$

In many works modern airfoil static C_L and C_T have been measured during experimental test [50][67]. The problem of relating rotor thrust capabilities to airfoil section characteristics seems to be solved by this theory, but becomes more complex when it is recognized that the rotor thrust limit is not dependent upon the maximum static airfoil lift, but there is also an unsteady or dynamic component which increases the thrust capability [14]. Through many experimental research it has been demostrated that the rotor is able to provide more thrust than would be calculated using just the quasi-static conditions, due to the phenomenon of dynamic stall. The fundamental problem for rotor designers is to find how the airfoil design affects the rotor's thrust capability and, probably more important, the increased pitching moment and power that accompanies the increased lift associated with dynamic stall.

2.2.1 Retreating Blade Stall

In helicopter flight, the dynamic stall problem usually occurs on the rotor when the helicopter flies at high forward speed or during particular maneuvers which lead to high load factors. It has long been known that the high speed characteristics of rotary wing aircraft are limited by two factors: transonic flow at the tip of the advancing blade and dynamic stall at the retreating blade. From the schematic view of a helicopter in forward flight of fig. 2.5, it is possible to notice that, while at the advancing blade rotational and forward speeds add, the retreating blade operates at lower Mach and even faces reverse flow. In particular, increasing the flight speed involves a reduction of the effective airspeed experienced by the retreating blade. It is clear that the retreating blade must produces an amount of lift equal to that of the advancing blade. Therefore, the decrease of the effective airspeed is compensated by higher AoA, in order to equalize lift throughout the rotor disk area. Then, the AoA needs to change depending on the position of the rotor blade, and this is possible performing a pitching motion. The limitation within this solution is that increasing the flight velocity above a certain threshold implies values of the AoA so high as to approach the stall region.

The situation decribed so far is more complicated when it is considered that the lift pattern of a helicopter rotor changes when a forward speed exists. As illustrated in fig. 2.6, in hover the area with an appreciable lift, called *no-lift area*, is located at the rotor centre. As forward

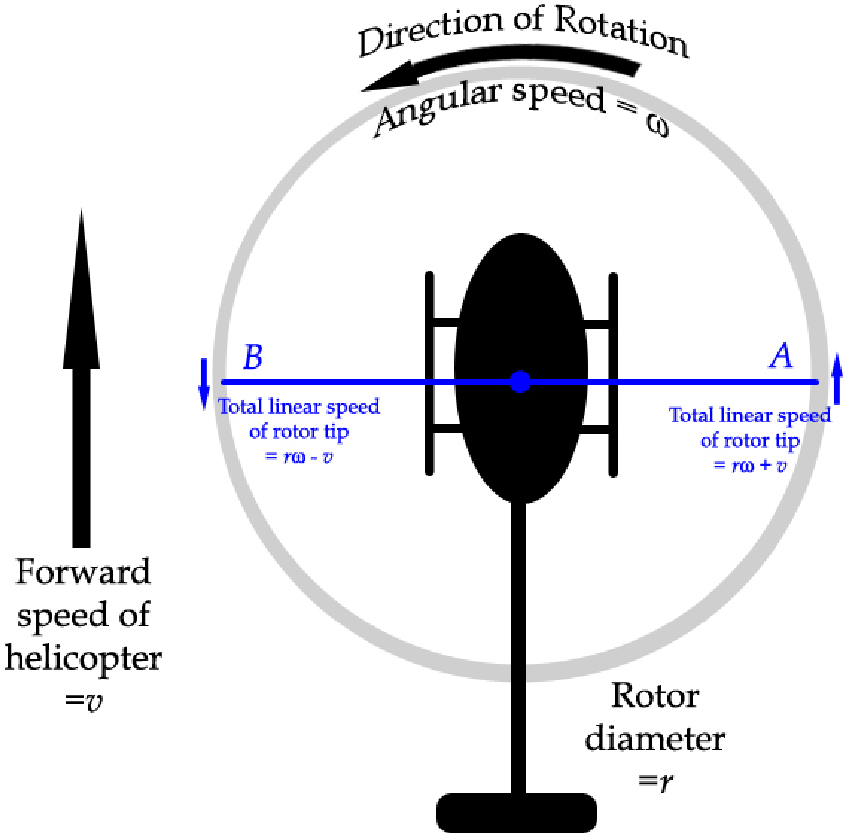

Figure 2.5: Dissymetry of velocity distribution on rotor blades [1]

airspeed increases, this area affects mainly the left side of the rotor, and covers more of the retreating blade sectors. In cruise this area can be divided in three different regions. In the *reversed flow area* the blade section has a rotational velocity lower than the aircraft airspeed and air flows from trailing edge to leading edge. In the *negative stall area* the rotational velocity of the airfoil is faster than the aircraft airspeed and air flows from leading edge to trailing edge. However blade flapping is not sufficient to produce a positive AoA, due to the relative arm and the induced flow. Conversely, in the *negative lift area* blade flapping and rotational velocity produce a positive AoA, but not to a value that yields appreciable lift.

Under these conditions the lift of the small outer retreating blade portions must produce more lift to compensate for the loss of lift of the inboard retreating sections, always in order to balance lift across the rotor disc. Then, near the tip it is necessary to have an even higher AoA, leading to a distribution such as in fig. 2.7. Here is assumed that the stall angle is 14°and AoA distribution is shown at eight positions in the rotor. Although blades are classically twisted, so pitch decreases from root to tip, the AoA is higher at the tip beacuse of induced flow [1]. As incidence exceeds the stall value, a stall region develops as marked.
When blade stall occurs, it results in a considerable vibration of the helicopter, followed by

---

[1] Source: en.wikipedia.org

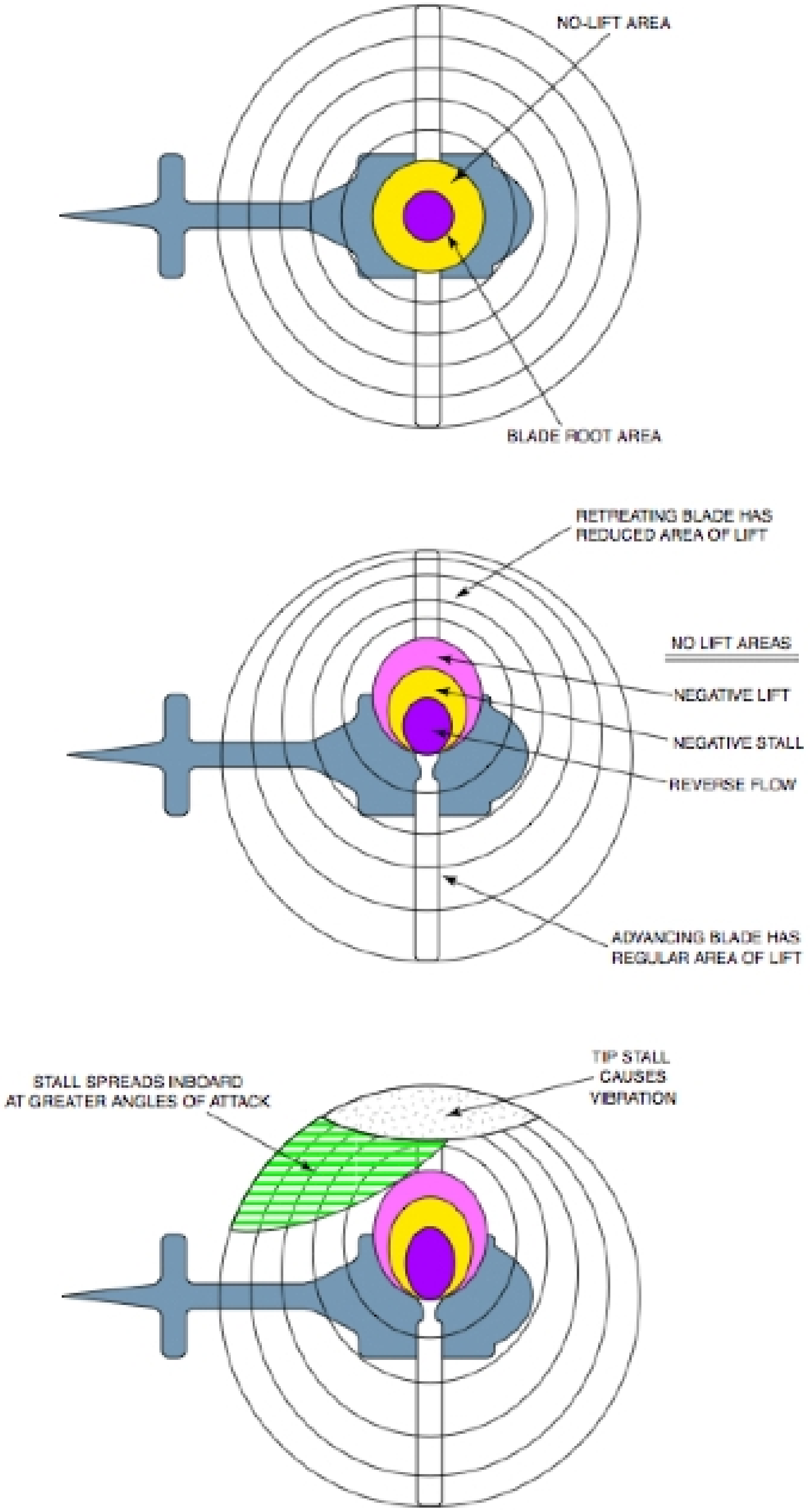

Figure 2.6: Lift pattern of a helicopter for hover, cruise, and critical forward flight speeds [53]

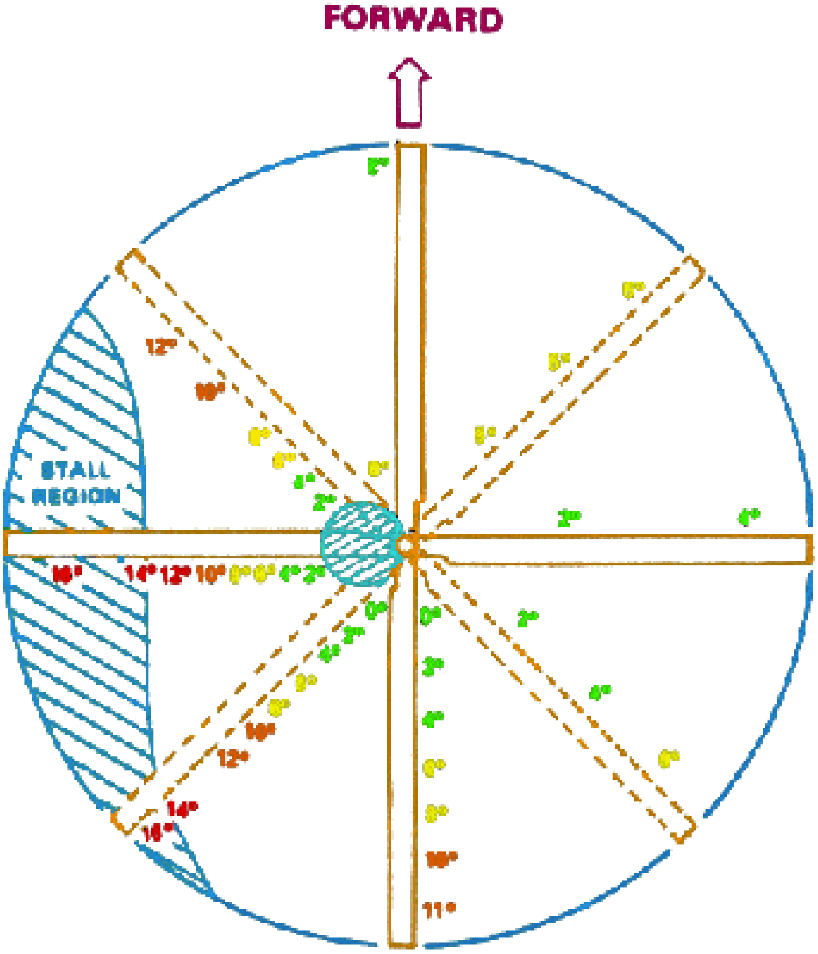

Figure 2.7: Angle of attack distribution during retreating blade stall [1]

both a rolling and a pitching up tendency. This condition may be aggravated if the cyclic stick is held forward and collective pitch is not reduced or even increased, manifesting ever greater vibrations and a loss of control [1]. It is clear then how with the aerodynamic phenomenon also structural problems occur. The rotor blades experience large torsional airloads and vibrations, that can quickly exceed the fatigue or endurance limits of rotor and control system. Usually a small amount of stall can be endured by the rotor, but because the rapid growth of these structural loads, dynamic stall is still a limiting factor in the flight envelope of helicopters [39].

2.2.2 Three-dimensional Effects in the Rotor Environment

In this chapter dynamic stall has been introduced, providing a good basic overview of the physics behind this phenomenon. However, it is important to notice that much of what is known today about dynamic stall has been obtained from experiments on idealized two-dimensional airfoils, but reality is quite different. When dynamic stall occurs on helicopter rotors, several radial and azimuthal parts can simultaneously experience its effect, showing many three-dimensional characteristics. This problem has been investigated by BOUSMAN [6] and ISAACS & HARRISON [26], providing a good in-flight documentation through flight test measurements. In particular, results by BOUSMAN reported in fig. 2.8 show the time history of the lift and pitching moment at various radial positions on the blade of a UH-60 helicopter during a pull-up maneuver (η = 0.3 and C_T/σ = 0.17). Results are presented in terms of the nondimensional quantities M^2C_l and M^2C_m, normalized by the speed of sound rather than the local section velocity, giving a global representation of airloads on a blade. Characteristic features of dynamic stall appear on several locations of the rotor. In fig. 2.8a, lift stall is most clearly observed for the radial stations from $r = 0.775$ to $r = 0.92$. Strong stall events are evident in two points (marked with L), between 273° and 278° and between 51° and 54° extending from $r = 0.675$ to the tip. Several additional peaks indicative of lift stall may be seen. A limited area of lift stall is visible at about 5° towards the tip. One peak is also noticeable at about 330°, more prominent outboard. Moreover, there are suggestions of lift at about 190° at $r = 0.225$ and at about 190° at $r = 0.40$. In fig. 2.8b the section moments are shown. At the inboard stations, moment stall is observed at 164° at $r = 0.225$ and at 166° at $r = 0.40$. At the outboard portions, from $r = 0.775$ to $r = 0.92$, moment stall associated with a first daynamic stall event is seen at 45° (marked with M), but disappears near the tip. A second stall cycle, again labeled with M, occurs from 252° to 263°. A third cycle is also apparent from $r = 0.675$ to the tip, occurring between 320° and 330°.

What turns out to be evident in this short comment is that dynamic stall is really complex to be evaluated on a complete helicopter rotor. both with experimental investigations and computational models. Fortunately, modern progress in advanced CFD leads to achieve good results even under these complex conditions.

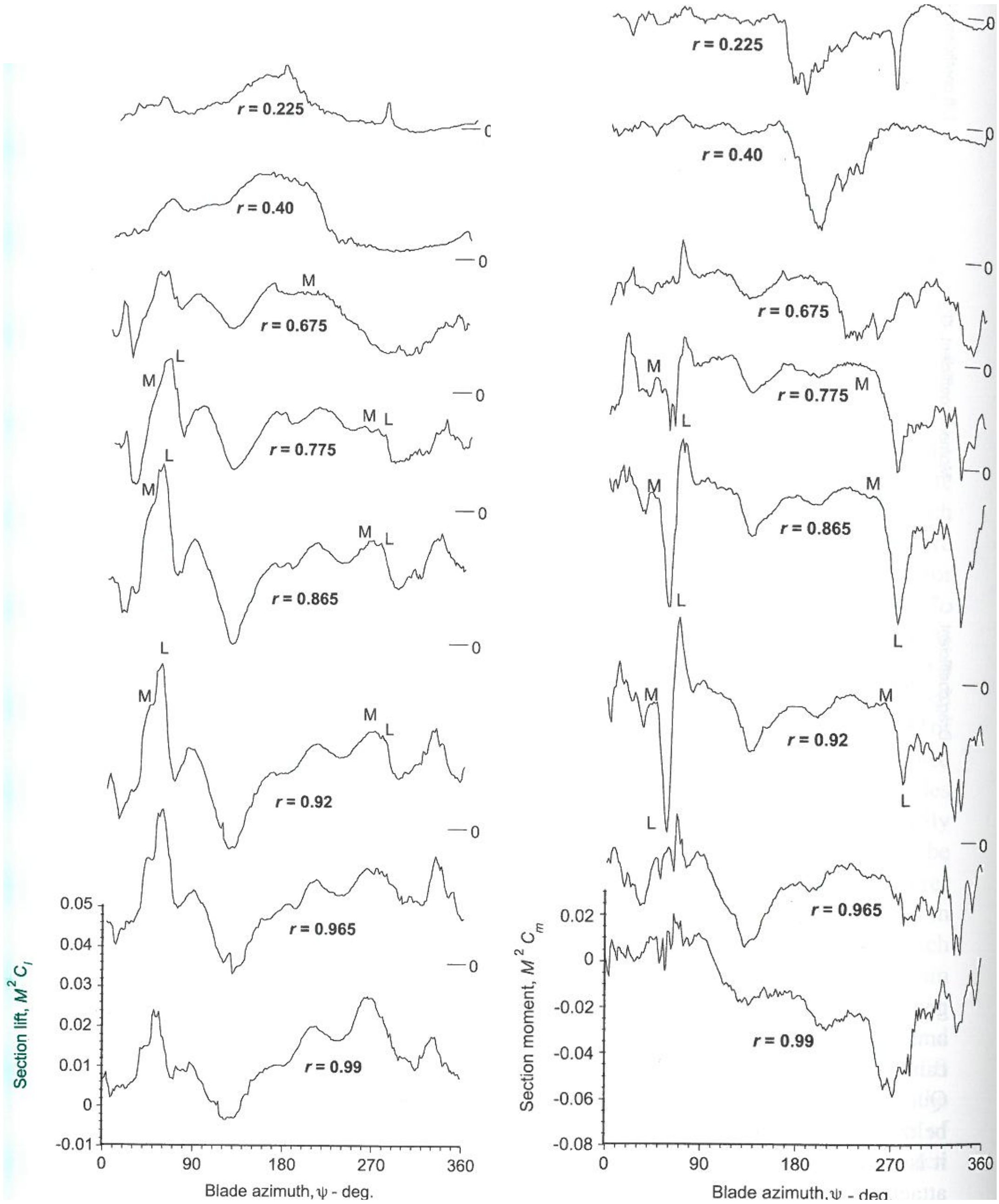

(a) Lift variation **(b)** Pitching moment variation

Figure 2.8: In-flight measurements of c_l and c_m operating at high thrust in forward speed [39]

3 CFD Theory

After more than 60 years of researches, dynamic stall prediction is still a challanging topic, even with the most modern CFD techniques. In this thesis computational investigations have been performed with the hybrid RANS solver DLR TAU, which today has reached a high level of maturity and reliability. It is commonly used in the German aerospace industry and it has been established at all European Airbus sites as the standard hybrid flow solver for complex applications [61]. In this chapter the code and some fundamental theoretical notions are briefly introduced.

3.1 The DLR TAU code

TAU is a modern software system designed for predicting flows around complex aerospace configurations on hybrid unstructure grids, from the low subsonic to the hypersonic flow regime. The system is composed of a number of modules and libraries to allow easier development, maintenance and reuse of the code or parts of it. Among many advanced features, TAU shows a high efficiency on parallel computation and a good optimization for cache processors. Parallelization is based on domain decomposition and the message passing concept using the communication protocol MPI. The different modules of TAU are grid partitioner, pre-processor, various solvers, grid adaption, grid deformation, CHIMERA technique, transition and turbulence modeling and utilities for post-processing. It is apparent how TAU is a highly advanced code, and it is not the purpose of this thesis to describe all these modules. Nevertheless, some basic informations about the solver are usefull to better unerstand how TAU works.

The standard solver uses an edge-based dual-cell approach in a vertex-centred finite volume formulation. Convective terms are computed using either first- and second-order upwind or central discretization with artificial scalar or matrix dissipation. Viscous terms are computed with a second-order central scheme instead. For the solution of the discrete equations both explicit and implicit schemes are available, with residual smoothing and several convergence acceleration strategies, such as local time stepping and multigrid. The turbulence models implemented in TAU include linear and nonlinear eddy viscosity models. The standard turbulence model is the Spalart-Allmaras Model (SAM) with Edwards modification, which yields highly satisfactory results for a wide range of applications while being numerically robust, but other SAMs are available. Furthermore a number of different two-equation models are implemented, especially k-ω like Menter SST, Wilcox and Kok-TNT. Besides these, Reynolds stresses can be directly computed using several RSM configurations. Finally, there are options to perform Detached Eddy Simulations (DES) based on the Spalart-Allmaras or the Menter SST model.

3.2 Key Concepts in CFD analysis

Subject of this section is to provide a brief explanation of some concepts which will be relevant during this work. It has long been known how the generation of high-quality computational grids for viscous simulations of complex configuration is identified more and more as a key technology for industrial CFD. Besides the grid generation, solver settings define quality and convergence speed of the solution.

3.2.1 Grid Importance

The partial differential equations governing fluid flow are not usually amenable to analytical solutions, which are applicable only to symplified problems. Therefore, in order to analyze fluid flows, the domain where the flow is computed, or *physical space*, is divided into a large number of smaller subdomains, called *grid cells*, and discretized governing equations are solved inside each of these portions. The process of creating an appropriate grid (or mesh) is termed *grid generation*, and has long been considered a bottleneck in the analysis process due to its strong influence in obtaining a good solution. It is well known that a good grid helps the computational fluid dynamics solver to converge to the correct answer while minimizing the computer resources expended. Stated differently, most every decent solver will yield an accurate answer with a good mesh, but it takes the most robust of solvers to get an answer on a bad mesh. This gives prominence to the importance of the mesh generation process, which in time has proved to be not an easy task.
Basically, there exist two different types of grids:

Structured grids: A structured grid is characterized by regular connectivity that can be expressed as a two or three dimensional array. This restricts the element choices to quadrilaterals in 2D or hexahedra in 3D.

Unstructured grids: An unstructured grid is characterized by irregular connectivity and is not readily expressed as a two or three dimensional array in computer memory. This allows for any possible element that a solver might be able to use. Compared to structured grids, the storage requirements for an unstructured grid can be substantially larger since the neighborhood connectivity must be explicitly stored.

The main advantage of structured grids follows from the easy and univocal definition of grid points. This property allows to access the neighbours of any grid point very quickly and easily. Through this expedient, the evaluation of gradients, fluxes and also the treatment of boundary conditions are greatly simplified [5]. However, there are also disadvantages, first of all the difficulty of generating a structured grids for complex geometries. In order to simplify the grid generation, several methodologies have been developed, like the *multiblock approach* [59][60] and the *Chimera technique* [4][29], but problems still exist. Concerning the unstructured grids, they offer the largest flexibility in the treatment of complex geometry [66]. The main advantage is the possible automatic grid generation by setting some parameters appropriately, independently of the complexity of the domain. Moreover, the number of grid cells, edges, faces and possibly grid points can be reduced and the time required to build an unstructured grid is significanly lower than what it is necessary for a multiblock structured grid. Mentioning also the disadvantages of an unstructured grid, one of them is the necessity to employ sophisticated data structures within the flow solver, leading to reduced computational efficiency [5]. Furthermore, unstructure grids have shown to be unsuitable with boundary layer resolution, as opposed to structured grids.

To exploit the advantages of both structured and unstructured grid, modern approaches ground on hybrid grids, which contain structured and unstructured portions. They consist of a mix of quadrilaterals and triangles in 2D and of hexahedra, tetrahedra, prisms and pyramids in 3D. This type of grids allows to adopt structured grid where it is necessary, especially near the wall in order to correctly resolve the boundary layer, and unstructured grid for the remaining flowfield.

Beside the coice of the grid type, there are many guidelines to follow during the grid generation. Care must be taken to ensure proper continuity of solution across the common interfaces between two subdomains, avoiding holes or overlapping, so that the approximate solutions inside various portions can be put together to give a complete picture of fluid flow in the entire domain. Additionally, the elements should be as regular as possible, the grid should be smooth, without any abrupt change in the volume of the grid cells or in the stretching ratio, and fine enough to correctly solve the flowfield and catch all flow features existing in the system.

All the guidelines listed so far must be always borne in mind to generate a high-quality grid, but this is not enough. It has long been noticed that a good grid is always associated with the physics of the problem that it tries to solve. Changes of boundary conditions, load conditions, analysis types, or flow models, may turn a good grid into a bad grid. Good grid needs to resolve physics, not just respect geometrical rules or follow the CAD model. This implies that is possible to generate a good grid only if the physics of the problem is well known, leading to different approaches. This considerations will turn out to be fundamental also in this work.

3.2.2 Iterative Methods

The first choice in the solver setting concerns the scheme to solve the discrete equations. Various explicit Runge-Kutta schemes are available in TAU, so called multi-stage time-stepping

schemes, where the solution is advanced in several stages and the residual is evaluated at intermediate states. They are widely know as numerically cheap, with small memory requirements, but stability limitations restrict significantly the maximum time step permitted. Particularly in the case of viscous flow, highly streched grids or complex equations systems, such as using turbulence models, the convergence to steady state slows down substantially. Furthermore, explicit schemes can become unstable or lead to spurious solutions. Several convergence acceleration methods have been introduced, such as local time stepping or multigrid. The multigrid method, the last and probably the most important convergence acceleration technique, is very well implemented in TAU, based on agglomerated coarse grids generating by the pre-processing. Multigrid method represents a valid help to get a good solution and it was often demonstrated that multigrid can accelerate the solution of the Navier-Stokes equation by a factor between 5 and 10 [5].
Nevertheless, it is often helpfull to use large time steps without dampering the stability of the time integration process. Then implicit schemes are the best solution, due to their superior robustness and convergence speed when it is necessary to solve stiff equation systems. Obviously, faster and more robust implicit schemes require higher computational effort per time step or iteration. In the TAU code the Lower-Upper Symmetric Gauss-Seidel (LU-SGS) iterative scheme has been selected because its low memory requirements, low operation counts and a relatively easy parallelization possibiity. It has been shown that LU-SGS can converge approximately twice as fast as the Runge-Kutta scheme, resulting in a reduction of the overall calculation time by a factor of 2.5 [61].

3.2.3 Spatial Discretization Schemes

A further basic choice concerns the numerical methods used to perform the spatial discretization of the convective term, while the viscous fluxes can be reasonably discretize only employing a central difference schemes due to their physical nature. The central scheme is the most widespread due to its convenience in terms of numerical effort required, and hence CPU time per evaluation, its stability and the relatively easy achievement of a second order solution. As well presented by BLAZEK in his book [5], the basic idea behind this scheme is to compute the convective fluxes at a face of the control volue from the arithmentic average of the conservative variables on both sides of the face. This method introduces odd-even decoupling problems (generation of two independent solutions of the discretised equation) and overshoots at shocks, so an artificial dissipation has to be added for solution stability. A scalar dissipation scheme is the first option, leading to a less accurate resolution of discontinuities and boundary layers than the upwind scheme, but with a considerably save in computational costs. It is also possible to improve accuracy using different strategies, such as the matrix dissipation approach, without increasing the computational effort. Even though these central difference schemes have proven to be reasonably effective in many cases, there are strong motivations for reducing the numerical dissipation being produced. The dissipative character of the artificial terms is important because it influences both stability and accuracy. For example, if the

dissipation is too large at a solid boundary, an artificial boundary layer is created in an inviscid flow, and the effective Reynolds number for a viscous flow is altered. Moreover, by appropriate reduction of the artificial dissipation, shock wave representation and boundary layer definition (especially the wall shear stresses) can be improved on coarse meshes. However, it has been observed that on unstructured or hybrid grids the explicit Runge-Kutta time-stepping scheme sometimes becomes unstable if combined with the conventional central scheme [5].
On the other hand, there are more advanced spatial discretization schemes which are based on the physical property of the Euler equations. Because they distinguish between upstream and downstream, they are termed *upwind schemes*. They are numerous, often divided into four main groups, but the most popular and widely employed on hybrid grids is certainly the flux-difference splitting scheme of Roe. It provides higher resolution of boundary layers and lower sensitivity to grid distortions in comparison with the central scheme. Obviously, improved performance corresponds to higher computational costs, but this is not the only disadvantage. For second- or higher-order spatial accuracy the generation of spurious oscillations near strong discontinuities may occurs. To avoid this problem limiter functions have to be employed, increasing considerably the computational effort, particularly on hybrid grids. Moreover, small oscillation in the solution must be taken into account.

3.2.4 Turbulence Models

Finally some considerations about turbulence models are necessary, since dynamic stall involves complex turbulent flows. The Spalart-Allmaras one-equation turbulence model represents the easiest way to approximate the Reynolds stresses in the Reynolds-averaged Navier-Stokes (RANS) equations. This approach provides a reasonably accurate prediction of turbulent flows with adverse pressure gradients and is capable of smooth transition from laminar to turbulent flow at user specified locations. Furthermore, SAM has some numerical advantages: it is robust, with fast convergence to steady-state and requires a moderate grid resolution near the wall. It can be also easily implemented on hybrid grids, since it is defined as a "local" model, namely equation at one point does not depend on the solution at other points. Besides, second-order equations are widely used and k-ω Shear Stress Transport (SST) turbulence model represent the state of art. All these models, named first-order closures, are based on Bousinessq or nonlinear eddy-viscosity models. Although two-equation models can be superior to one-equation models, without modification they still fail to capture many of the features associated with complex flows [34]. While these models can be modified to improve their predictive accuracy, the modifications cannot be easily generalized [70]. Moreover, in the case of strong separation even the modified two-equation models were shown to fail to predict flow physics due to their isotropic nature [64]. Therefore, anisotropic models are necessary for accurate prediction of complex separated flows, discarding the eddy-viscosity approach and computing directly the Reynolds stresses.
The RSM, or second-order closure, is a a high level turbulence model, as well as the most elaborate, where the exact equations for the Reynolds stresses has been derived. Since the RSM

accounts for the effects of streamline curvature, swirl, rotation, and rapid changes in strain rate in a more rigorous manner than one- and two-equation models, it has a greater potential to give accurate predictions for complex flows [38]. The modeling of the pressure-strain and dissipation-rate terms is particularly challenging, and often considered to be responsible for compromising the accuracy of RSM predictions[37]. Moreover, RSM are much more complex and computationally expensive than eddy-viscosity model, as well as less stable.

Concluding this chapter, it should be noticed that a turbulence model which can predict reliably all kinds of turbulent flows does not exist. As BLAZEK states in his book [5], each model has its strengths and weaknesses, and the most modern strategies do not always give the best results. Therefore, differing modelling strategies are evaluated within this thesis to show how different turbulence models and solver parameters affect the solution of the problem considered. The final target is the identification of the best strategies and setting to achieve the best results.

4 Model and Test Case

As mentioned in the introduction, the airfoil investigated is the ONERA 209, actually in use on a variety of flying helicopter (fig. 4.1). This blade section is characterized by a chord length c of 0.3 m, a maximum thickness of 9% located at 29.3% of the chord and a maximum camber of 1.6% at 17.1% of the chord. The airfoil ends with a blunt trailing edge, which suggests a carefull discretization of the structured grid in this region.

The test case chosen for this work is characterized by inflow properties presented in table 4.1. The flow considered is dry air at room temperature and the operating Reynolds number reveals the necessity of modelling the viscosity. The Mach number adopted implies the invalidity of hypotesis of incompressible flow, so that compressibility must be considered and no simplifications are introduced in Navier-Stokes equations. However, strong discontinuities like shock waves are not expected.

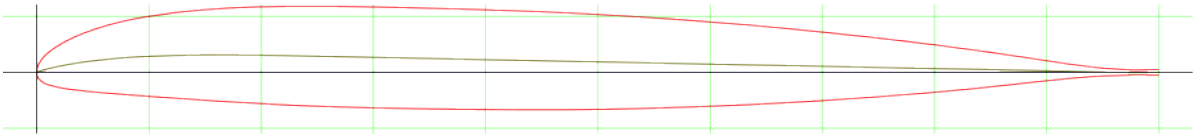

Figure 4.1: Airfoil OA209[1].

Table 4.1: Properties of the incoming flow

INFLOW PROPERTIES		
Parameter	Symbol	Value
Reynolds number	Re	$1.15x10^6$
Gas constant [J/kgK]	$\overline{R}$	287.053
Reference Mach number	Ma	0.31
Reference temperature [K]	T	300
Freestream velocity [m/s]	U_∞	107.64

---

[1] Source: www.AirfoilTools.com

4.1 Test Facility

Experimental investigations have been conducted in the German DNW-TWG wind tunnel located at DLR-Göttingen [23][58]. A carbon-fiber OA209 model with a span of b = 1.0 m was used in the 1m X 1m adaptive-wall test section of the DNW-TWG, visible in fig. 4.2a. Adaption of top and bottom walls was performed to reduce wall interferences at the position of the model. The wall shapes were adapted to the steady airfoil flow at the static mean AoA and kept constant while the model was pitching, as an unsteady dynamic wall adaption was not possible.

The model was equipped with a total of 45 miniature high-speed pressure trasducers (Kulites) along the model mid-span, and two accelerometers were installed to control model distortion. The aerodynamic coefficients were then integrated from the surface pressures measured by sensors; the accuracy of the pressure measurement was estimated to ±0.5% of the stagnation pressure. Results were recorded for 160 oscillatory cycles of the blade motion with 128 samples per cycle.

PIV recordings were also taken for each single test point where unsteady pressures were measured. To cover a larger area on the airfoil upper surface with a sufficient spatial resolution two cameras have been used in combination. With this arrangement almost 75% of the airfoil upper surface could be reached. Fig. 4.2b shows a sketch of the camera-views, airfoil and light sheet arrangements.

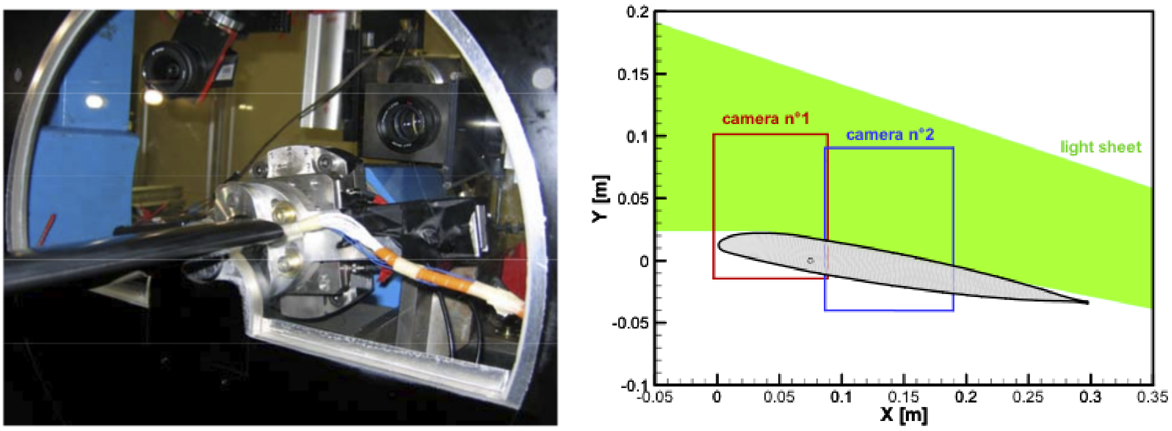

(a) Model and suspension in TWG-Test Section

(b) Illustration of PIV set-up

Figure 4.2: Test facility details [23]

4.2 Experimental Data

In tab. 4.2, the characteristics of the airfoil pitching motion are presented. The wall adaption was performed at the mean AoA as described before, and the airfoil oscillates around the centre of rotation, located at the quarter-chord, with an amplitude described by α_L. This value in the test case is sufficiently wide to imply a deep dynamic stall. The information about oscillation frequency is included in the reduced frequency parameter, commonly used in pitching airfoil problems, defined as $k = 2\pi f c / U_\infty$. To give a clearer first view of the motion, the frequency is also computed in the table.

The experimental data acquired are then reported in fig. 4.3, where the comparison between the steady polar and the unsteady cycle of the lift coefficient is shown. The steady polar is defined by 27 measurements of the lift coefficient while the AoA increases. The curve has the typical trend commonly known in aerodynamics, with a maximum lift coefficient equal to c_l = 1.426, corresponding to a static stall angle α = 13.878°. After this value, the c_l collapses and the lift loss is clearly visible.

Table 4.2: Set of parameters describing the airfoil pitching motion

AIRFOIL MOTION PARAMETERS		
Parameter	Symbol	Value
Mean angle of attack	α_0	12.87°
Amplitude of oscillation	α_L	±7.13°
Reduced frequency of rotation	k	0.1
Frequency [Hz]	f	5.71
Centre of rotation	O	25% c

The grey pattern defines the range of c_l values observed in several experimental cycles. It is apparent that, when the lift coefficient linearly increases with the AoA, all the cycles exhibit the same behavior and the range of variation observed in the c_l is negligible. Nevertheless, when first stall occurs and the flow begins to separate from the airfoil, the differences among measured cycles are more evident, and the c_l varies in a wide range due to the very nature of the post-stall flow. This tendency does not allow to define a precise AoA at which first and second stall occur, and especially the reattachment phase is described with a quite high level of uncertainty until the reattachment process is completed. Despite this, all dynamic stall features described previously in section 2.1 are visible. The lift coefficient rises with the AoA until first stall occurs at an AoA significantly higher then the static stall one: the extra lift generated is ≈ 30% of the maximum static lift. Also the second stall event is recognized in a further c_l peak. Then, when the AoA decreases, the flow reattachment follows a totally different path, generating a large hysteresis cycle, as expected after the deep dynamic stall present this test case.

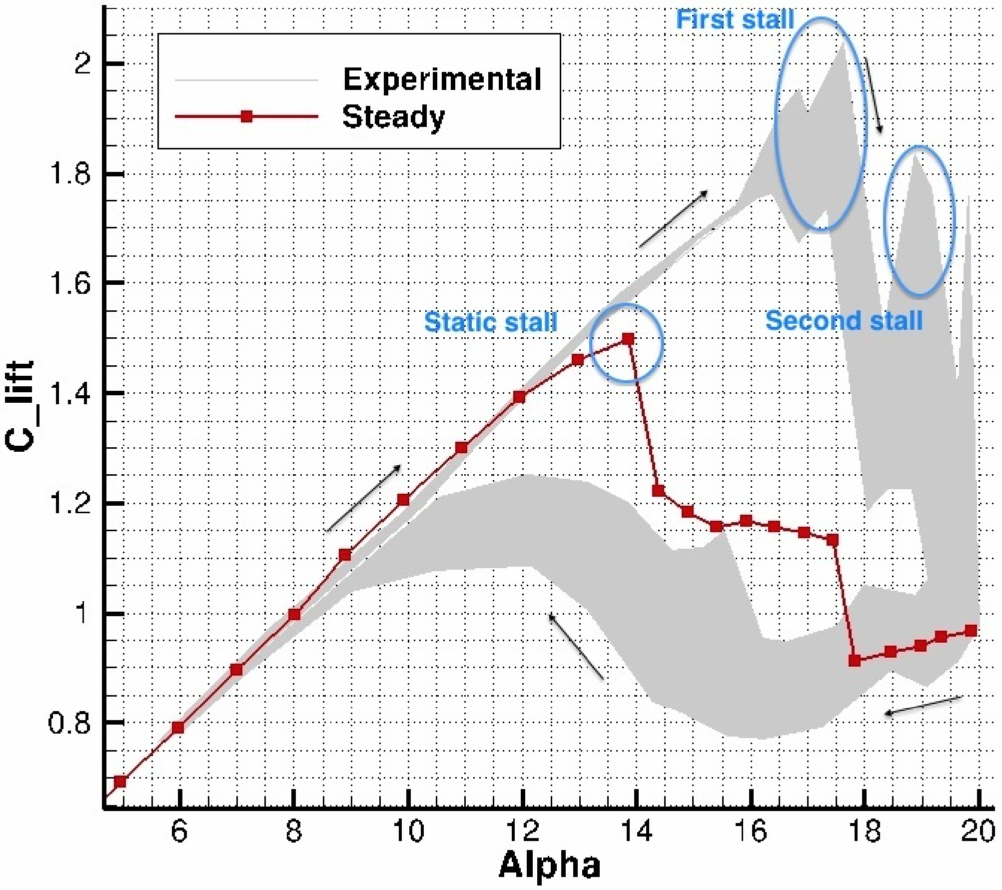

Figure 4.3: Experimental static polar and unsteady cycle of the lift coefficient

4.3 Wall effects in airfoil experiments

During experimental investigations it was noticed a discrepancy between 2D CFD simulations and experiment. Measurements are affected by wind tunnel wall interferences, which tend to decrease the lift measured as shown in fig. 4.5. The problem was noticed in all experimental investigations about dynamic stall [23][58][68]. This drawback was overcome in every previous work by simply adopting a correction in the lift coefficient measured. A suitable constant correction was found by the difference between numerically predicted lift and measured lift at $\alpha = 0$ in steady conditions and at the static mean AoA for unsteady computations. In this work, this means a correction of $\Delta c_l = 0.15$ for steady data and $\Delta c_l = 0.2225$ for unsteady data. It is as well evident the difference in slope between the lift coefficient curves in the steady case. Recent research have deeply invesigated this problem through 3D wind tunnel simulations, pointing out several causes [57]. First, boundary layers on wind tunnel walls have to be considered in CFD simulations. Second, the gap between model and wind tunnel side wall has large influence: model mounted without gap exhibits a better behavior then with gap. Moreover, 3D side wall influence tends to reduce lift in the center section, where 2D data are measured. All these considerations can be deduced by fig. 4.4, where several models are presented.

Having said this, in the present thesis only the first constant correction is adopted, reporting results of 2D simulations.

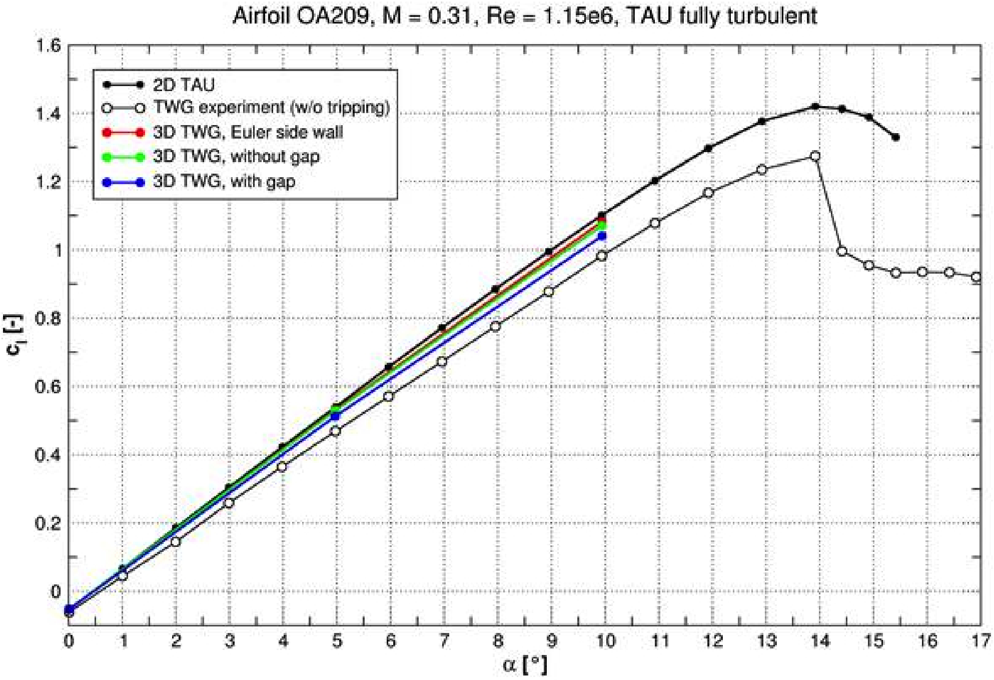

Figure 4.4: Lift coefficient versus AoA for three types of 3D wind tunnel simulations: Euler side wall, no-slip side wall without model gap and no-slip side wall with model gap [57]

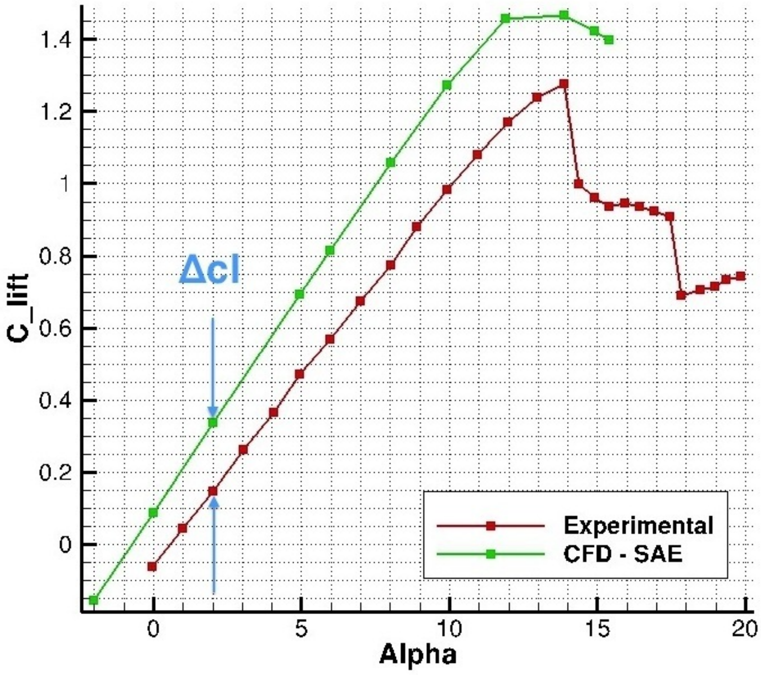

(a) Steady case

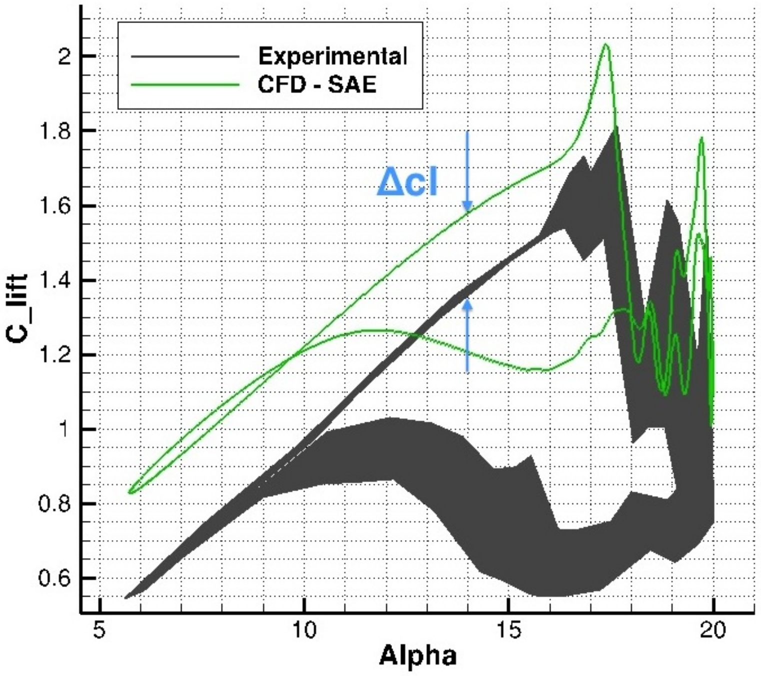

(b) Unsteady case

Figure 4.5: Δc_l introduced by wind tunnel wall effects

5 Static CFD Validation

The first step in the dynamic stall study is to compute airloads under static conditions and fully developed turbulent flow. Grid influence is investigated and several numerical methods are adopted and compared, in order to provide an accurate evaluation of every parameter which might affect the problem resolution. The purpose of this section is to find a good grid and setup, which can be used to compute the unsteady case. Effectively, good residuals convergence ($<10^{-6}$) and results accuracy under steady conditions will yield a good starting point when unsteadiness is introduced. Among the numerous turbulence models provided by TAU, this thesis is focused on the use of SAM and RSM.
Concerning the computational power, computations are performed on 128 domains of the LRZ Linux Cluster.

5.1 The Generation of the Grid

It is well known that the generation of high-quality computational grids is of primary importance in CFD studies. While TAU comprises modules for grid modification, namely the adaptation and the deformation module, it does not include grid generation. In this thesis grid generation is performed with the ANSYS ICEM-CFD software. First of all, as stated in section 3.2, the grid generation should begin from an analysis of what happens in the flow field. It is clear that, since the topic of this thesis is based on a stall event, the boundary layer separation has a fundamental role in the problem and the region near the airfoil must be accurately discretized. Second, the grid should have a higher density in the flowfield area affected by flow separation after stall occurrence.
The best approach has been recognized in the use of a hybrid grid, allowed by TAU code, consisting of a structured layers for the resolution of the boundary layer shown in fig. 5.1b, and an unstructured region in the outer flowfield, as visible in fig. 5.1a. The definition of an additional area with a size of ≈ 3 chords allows a higher element concentration where the flow is affected by the presence of the airfoil. This hybrid approach is computationally advantageous. It is well known that assuming a larger farfield distance results in a minimization of the farfield boundary influence and an accurate freestream simulation. Adopting structured grid this approach is usually impracticable, yielding to unacceptable costs in terms of computational time and forcing to set more complex boundary conditions. Through the hybrid approach, large farfield distances can be used without significantly increasing the number of

grid nodes, as well as the computational effort. The practical advantage is a significant reduction of the computational time which, although might appeared not so important in this step. It leads to a really advantage in view of unsteady computations. Another not less important advantage is the possibility to use the automatic mesh generation algorithm embedded in the ICEM-CFD software. This allows an easy modification of the structured region through a few parameters and an automatic generation of tri-elements.

Considering the spatial resolution of the hybrid TAU grid, three characteristics are mainly individuated: wall normal resolution, wall parallel resolution and outer field resolution. Concerning the wall normal resolution, it is mostly influenced by the number of structured boundary layers created. Altough in the static problem convergence may be reached using 20 layers, this resolution should be increased as suggested in the DLR report [58]. Some flow features occuring during the multiple vortex shedding after main stall or during flow reattachment take place inside the structured grid. Then, a special resolution of the velocity profile is necessary. A good compromise between accuracy and stability of the simulation has been found using 60 layers [58].

Fixed the number of structured layers used, after few simulations it is apparent how each turbulence model requires different first layer height. As the problem involves complete flow separation, evidently wall functions cannot be employed and a very low first cell height is necessary. For many turbulence models, as typical of SAM, this value is kept so that $y^+ \approx 1$. Nevertheless, it is commonly recognized that using RSM a lower value is required, resulting in $y^+ \approx 0.2$. Then, two different grids are generated and employed for each turbulence model, leading sometimes to different considerations. The wall parallel resolution, or surface resolution, will be investigated during further grid resolution studies, but it should be pointed out the strong relationship between surface resolution and height ratio in the structured layer when the grid is generated. The blunt trailing edge introduces some complications when associated to the automatic grid generator, and sudden changes in grid cell areas are present at the trailing edge. Hence, every time that the number of grid points on the airfoil surface or the height ratio change, a further calibration of the other parameter is necessary to overcome the problem shown in fig. 5.2a. Generally speaking, when one of these two values increases, the other one must decrease to have a grid with an acceptable smoothness, like in fig. 5.2b.

Regarding the outer field resolution, thanks to the unstructured meshing tool provided by ICEM it is possible to set the farfield condition far away from the airfoil, at a distance of 1000 chords and delimited by a circumference. As previously mentioned, thanks to the definition of an additional area it is possible to concentrate the elements in the flow region mostly affected by the presence of the airfoil. The curve which delimits such area has been approximate with a circle, and this configuration yields good results for many models. Nevertheless, when the number of grid points used is increased with the purpose to have a higher elements concentration, a strange growth of the unstructured grid is observed, especially in the downstream region as visible in fig. 5.3. The consequent poor grid quality is unacceptable, and this problem has been solved only using a C-grid shown in the next section, which better suits the blunt trailing edge.

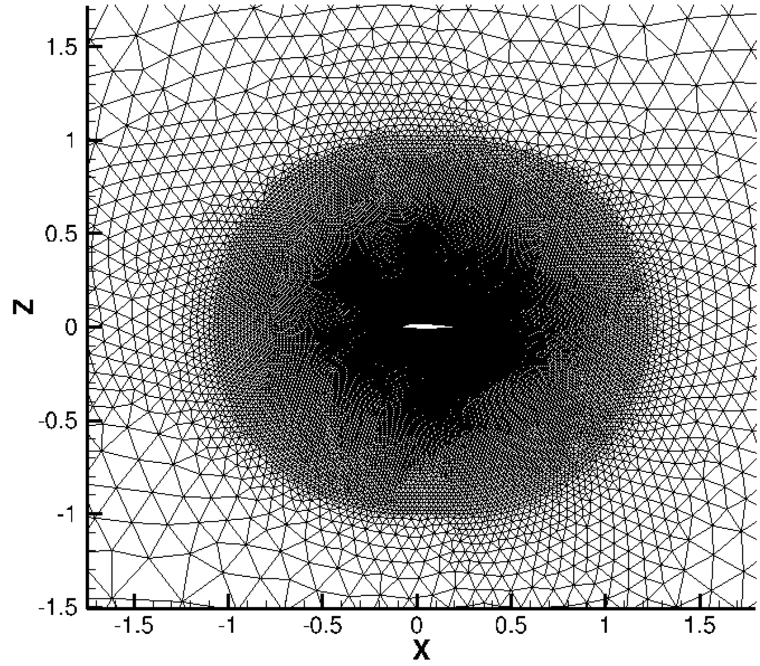

(a) Unstructured grid

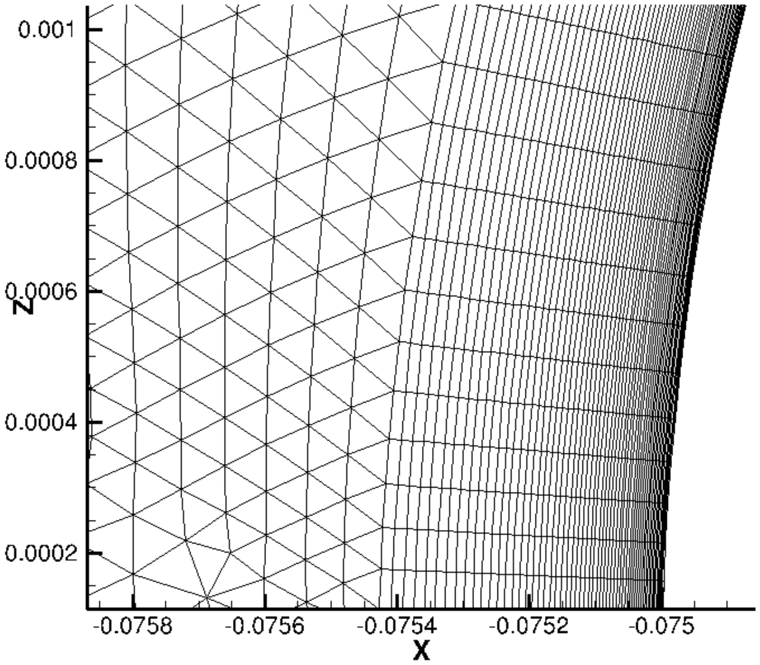

(b) Structured boundary layer

Figure 5.1: Hybrid grid created with ANSYS ICEM-CFD

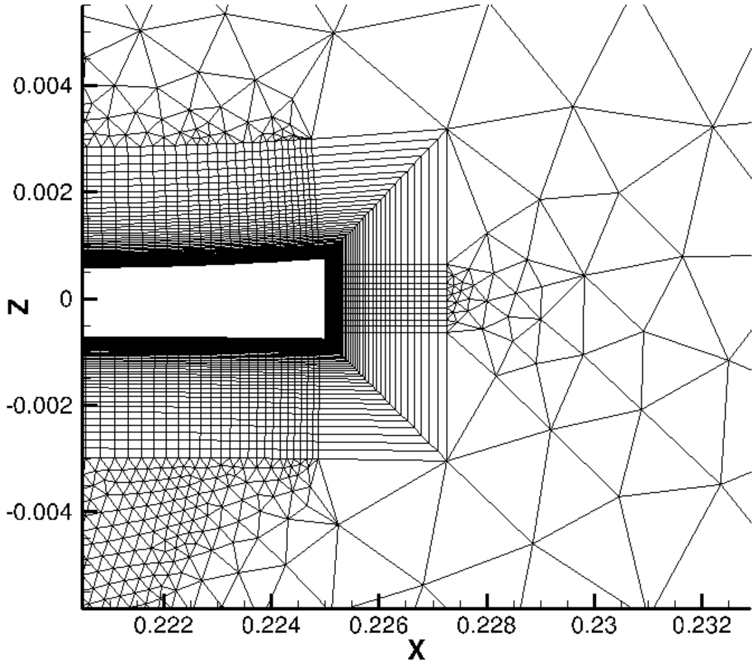

(a) Trailing edge grid problem (height ratio = 1.06)

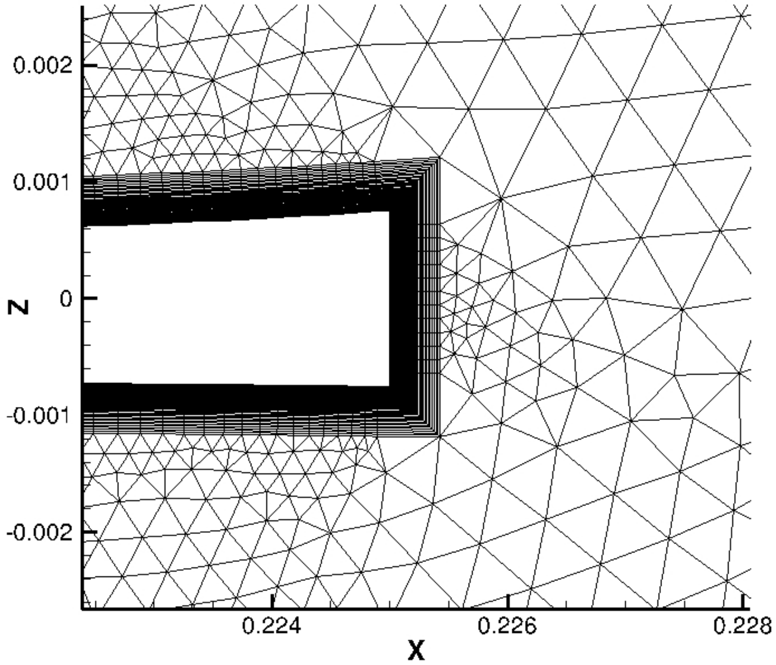

(b) Acceptable smoothness (height ratio = 1.04)

Figure 5.2: Grid generation problem at trailing edge

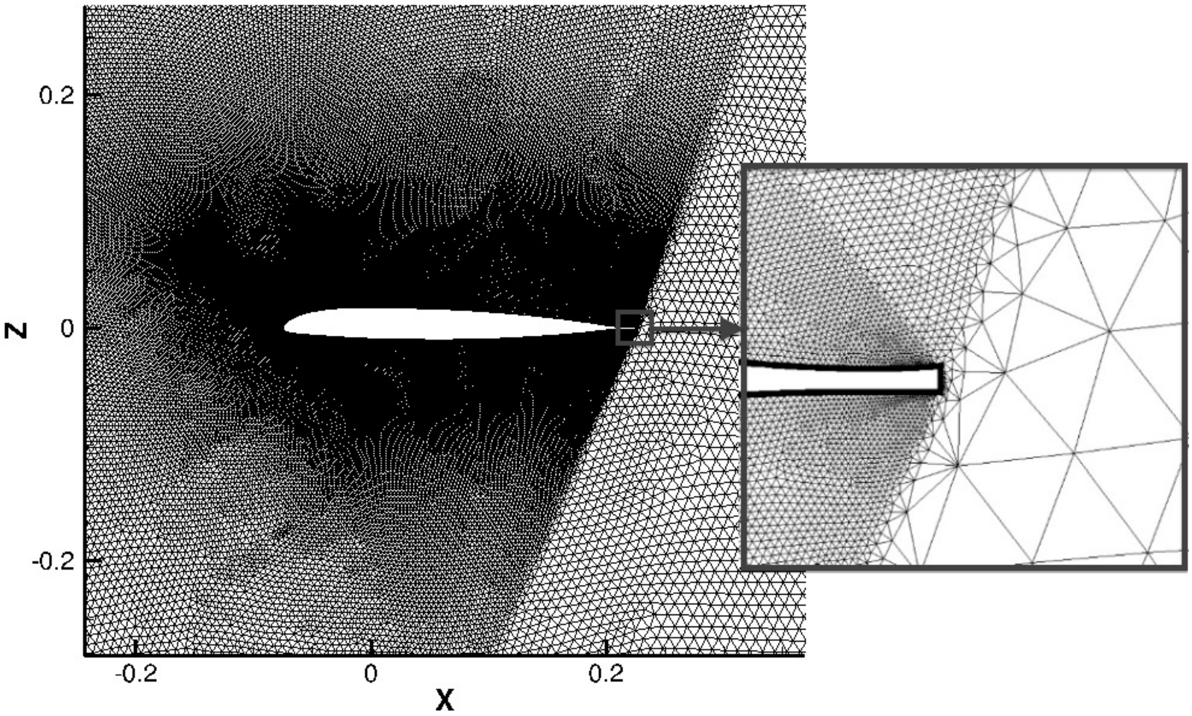

Figure 5.3: Problem with automatic unstructured grid generation

5.1.1 Grid Resolution Study

In tab. 5.1 three different grids are defined. It is necessary to say that, concerning the grid called *Coarse Mesh*, the adjective "coarse" does not really reflect the quality of this grid, which is already quite fine, but denotes the first grid created. In the grid generation process all considerations made in the previous section have been keeping in mind. In *Fine1* the surface resolution is increased through the doubling of the grid points on the airfoil, as apparent by comparing the plot of both grids in fig. 5.4. As previously mentioned, this involves a reduction of the height ratio and consequently of the entire structured region. In *Fine2* also the outer field resolution is increased, resulting in a significantly higher number of elements. In order increase the number of elements used, the C-grid approach has been used to define the elements concentration area, as clearly visible in fig. 5.5.

Fig. 5.6 shows the comparison among the lift coefficients versus the AoA. It is apparent that no improvement is introduced in the linear portion of the polar, where the three grids show the same behavior. When approaching the stall and the slope of the curve begins to decrease, the second grid better suits experimental data, introducing an improvement of $\approx$ 2.5% at α = 9.92°and of $\approx$ 6% at the static stall angle. The third grid does not exhibit a behavior better enough to justify the increase in computational effort due to the high number of elements used.

Considering that computing resources employed in this thesis are rarely available, the best compromise between accuracy and computational cost is provided by the *Coarse Mesh*, which

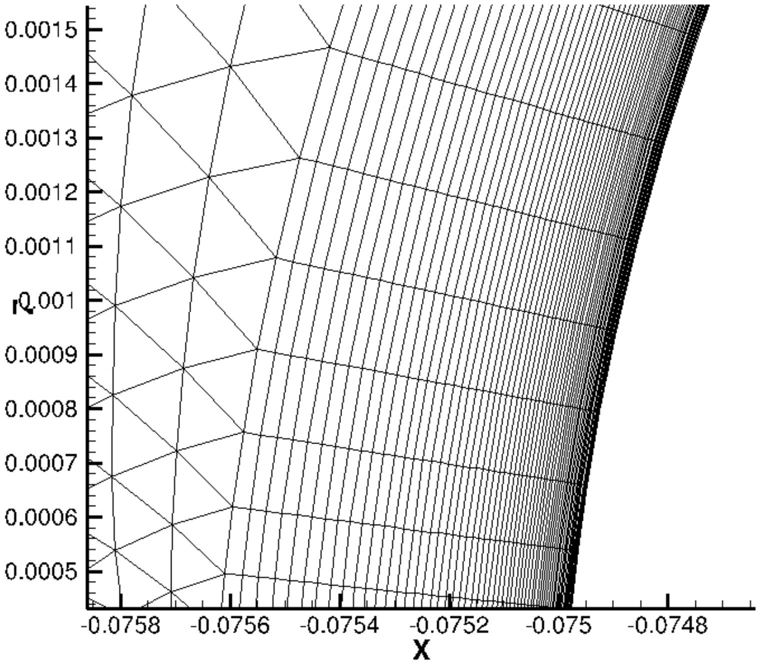

(a) *Coarse mesh*

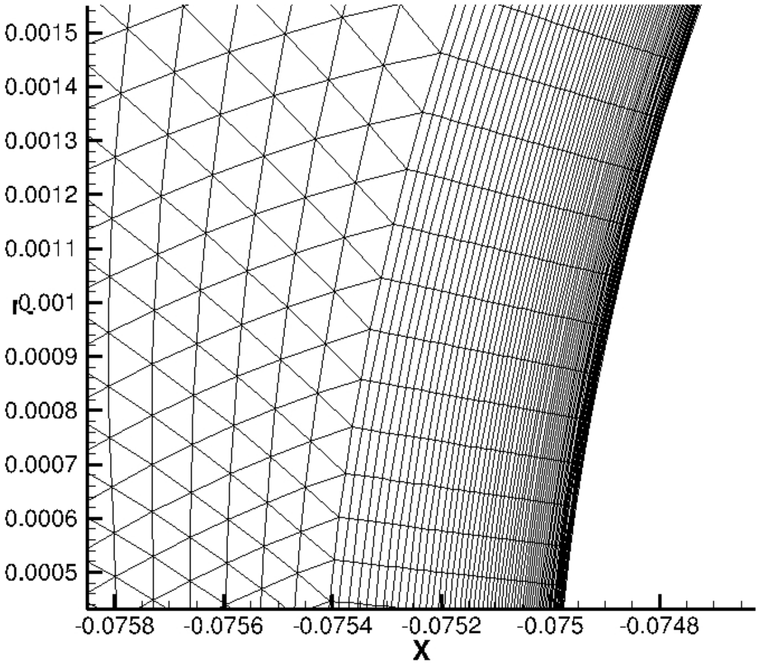

(b) *Fine1*

Figure 5.4: Surface resolution difference between *Coarse mesh* and *FIne1*

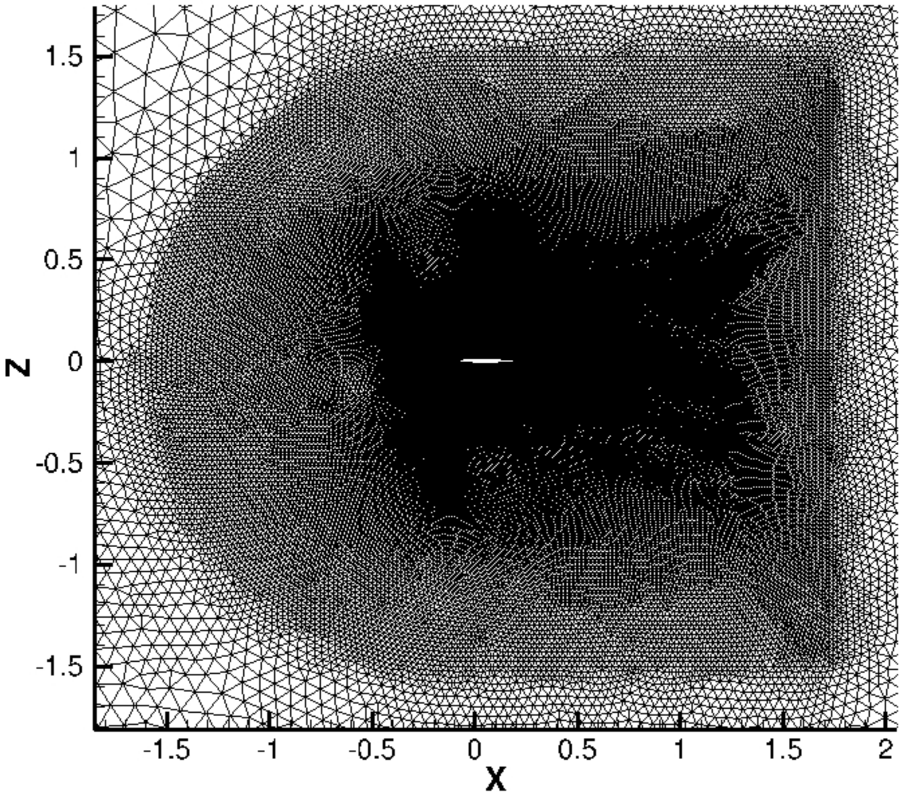

Figure 5.5: C-grid approach in *Fine2*

Table 5.1: Characteristics of three grids computed with SAM

GRIDS CHARACTERISTICS			
PARAMETER	Coarse Mesh	Fine1	Fine2
Surface resolution	0.5%	0.25%	0.25%
Number of nodes (2D)	89701	117894	189247
Number of elements (2D)	154611	186632	329510
Computational time (50 iterations)	2.12 [s]	2.51 [s]	3.23 [s]

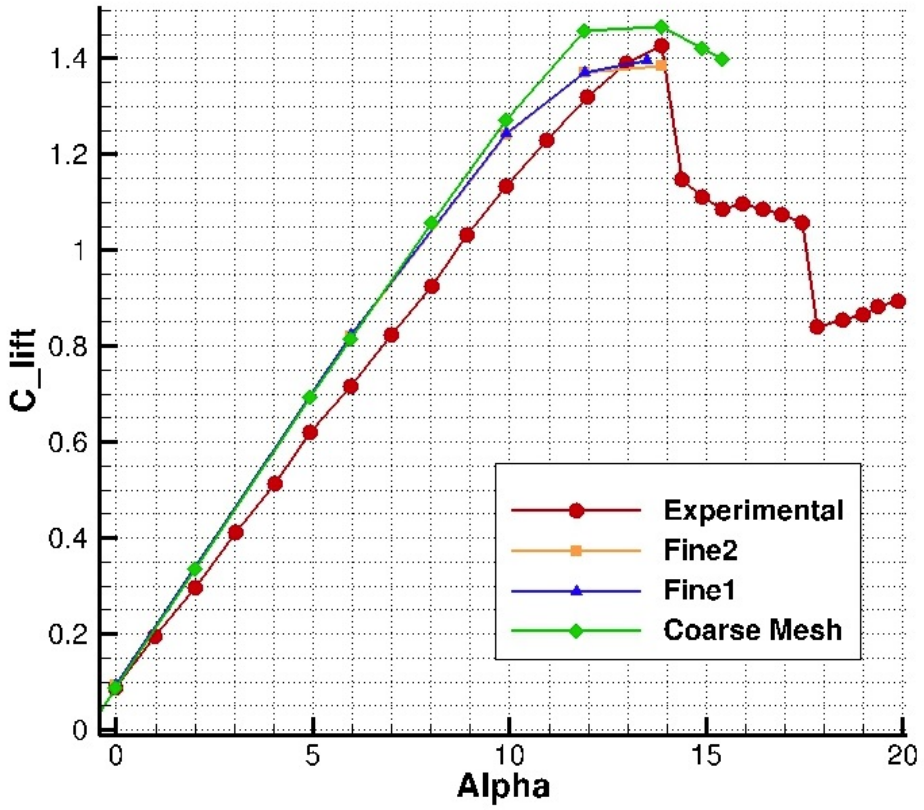

Figure 5.6: Comparison of c_l versus AoA for three grids, using the Spalart-Allmaras with Edwards modification turbulence model

seems to be promising for unsteady computation. Nevertheless, also the other grids will be compute under unsteady condition. Everything said so far has been observed employing the Spalart-Allmaras turbulence model, but similar considerations may be made using RSM.

5.2 Solver Settings

After the creation of the grid, solution parameters are set in the *Parameter File*, read by TAU. Concerning the choice of the time-stepping method, two approaches have been investigated: the explicit 4-stages Runge-Kutta scheme and the implicit backward Euler scheme. As mentioned in section 3.2, several problems have been observed when explicit schemes are used to solve particularly complex problems, exhibiting slow convergence or even instability. Since the problem at issue involves the solution of stiff equation systems, it is expected that implicit schemes will provide the best answer. The comparison between results obtained with the two discretization schemes are shown in fig. 5.7. Among all turbulence models, the Spalart-Allmaras with Edwards modification model has been chosen due to its reliability and robustness. Moreover, it was the only turbulence model which exhibited a sufficiently good behavior when coupled with the explicit scheme. As visible in fig. 5.7a, the oscillation of the lift coefficient are definitely larger with the implicit scheme. Convergence in c_l may be noticed after 600 iterations using the Runge-Kutta scheme, while the backward Euler scheme needs about 2000 iterations to show a sufficient oscillation reduction. This can be summarized by saying that the explicit method aims more quickly to the exact solution. Nevertheless, observing the residual behavior in fig. 5.7b, it may be notice that after a first rapid decrease, Runge-Kutta scheme shows a slower convergence compared to backward Euler scheme. Altough several acceleration techniques have been adopted, the achievement of a residual value under 10^{-5} is practically impossible. Through some other computation, it has been observed that this behavior worsens when the angle of attack increases and flow separation complicates the solution, resulting even in completely unstable results. Furthermore, it should be remembered that explicit schemes lead to significant restrictions in the maximum timestep permitted when unsteady computations will be performed. For these reasons, the implicit backward Euler schemes is definitively adopted from now on in all models.

Acceleration techniques are also used with the implicit scheme, and especially multigrid method improves significantly the covergence speed. This technique was originally developed by Brandt for elliptic partial differential equations [8] and later applied to the Euler equations by Jameson [27]. After that, it was employed to solve the Navier-Stokes equations [43][30]. Since a comprehensive definition of multigrid method may be easily found in literature, here the purpose is just to give a short description about how it works. This particular acceleration technique is based on the solution of the governing equations on a series of successively coarser grids. The decribed procedure allows to drive the solution on the finest grid faster to steady state, thanks to two effects:

- It is possible to employ larger timesteps on the coarser grids, with a consequent reduction in numerical effort [5]. Advantages in rapid convergence and lower computational time are obtained due to the distribution of the work for determining a new solution over the coarser grids.

- It is well known that almost all explicit and implicit time-stepping and iterative scheme reduces efficently the high-frequency components of the solution error, while the low-frequency components are barely damped [5]. The outcome is a slow convergence to the steady state after the elimination of the largest errors at the beginning. Using the multigrid method, the low-frequency components on the finest grids becomes high-frequency components on the coarser grids and are successively damped, reducing very quickly the entire error and significantly accelerating the convergence.

The multigrid method has proved to be in many cases a very powerful acceleration technique,

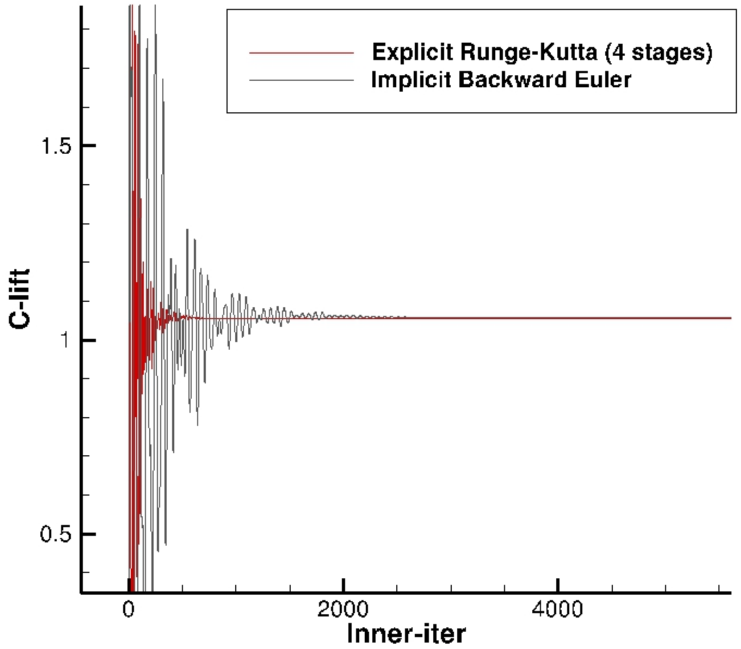

(a) Lift coefficient versus number of iterations

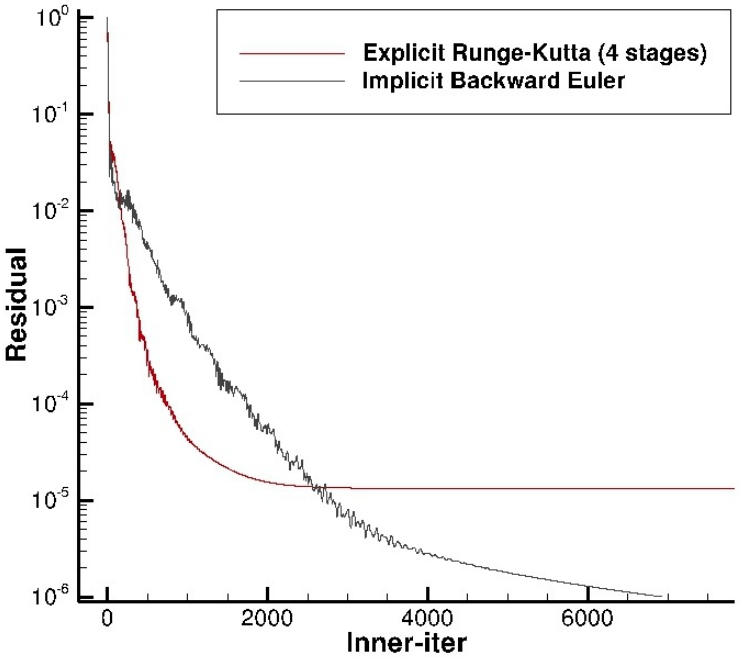

(b) Residual versus number of iterations

Figure 5.7: Comparison between explicit (4-stages Runge-Kutta) and implicit (Backward Euler) discretization schemes, at α = 8.01°and Spalart-Allmaras with Edwards modification turbulence model

and it reveals to be very helpfull in the solution of dynamic stall problem. TAU provides different predefined V- or W-cycle from one up to five level. The best results are obtained with the 3w++ cycle, that makes quite a lot of smoothing step on the 3rd level and reach a convergence rate in many cases even better than of a 4w cycle by approximately the same costs, which is at least true in parallel mode. It should be noticed that in parallel mode this can be advantageous because the lowest level contains more grid points which increase the parallel efficiency [15]. The use of the 3w++ cycle have shown significant advantage in terms of convergence speed in all steady computations, so it has been permanently adopted.

Crucial in convergence history is the spatial discretization scheme adopted for the convective term. As mentioned in the last chapter, central and several upwind schemes are available in TAU. Actually, upwind differencing schemes seem to have gained much more popularity on unstructured and hybrid grid than the central scheme [5]. Hence, first-order upwind scheme can be consider a valid first step in the solution process, and it has been used in this work, reaching a fast convergence. Nevertheless, since the purpose is the accurate prediction of the unsteady case, higher accuracy is required and a second-order upwind scheme is employed, reducing numerical diffusion associated with first-order upwind schemes. As mentioned in section 3.2, it is commonly known that in the solution of complex flows problems upwind scheme becomes sometimes unstable. This is what has become clear from first computations, when convergence has not been easily obtained, especially at high AoA. Conversely, as suggested by previous studies [23][58][68], central scheme provides a good solution and a fast convergence, thanks to the artificial dissipation introduced in the flow which acts as a damper in the solution process. This tendency is even more evident in fig. 5.8a, which represents a typical residuals behavior of these discretization schemes.

The most stable and efficient solver configuration under steady conditions has proven to be the central scheme for the convective flux discretization, matched with the second-order Roe upwind scheme for the convective fluxes of the turbulence equations. In spite of this, many efforts have been made to have an acceptable convergence in aerodynamic coefficients using the second-order upwind scheme, which introduces significant improvements when associated with RSM, as visible in fig. 5.8b. In particular, the upwind scheme describes more accurately the trend of the c_l curve when separation begins, predicting with higher precision the slope changes of the curve. All efforts have been done bearing in mind that stall behavior is difficult to describe under steady conditions, and there was no desire to discard solutions that may prove promising in unsteady study.

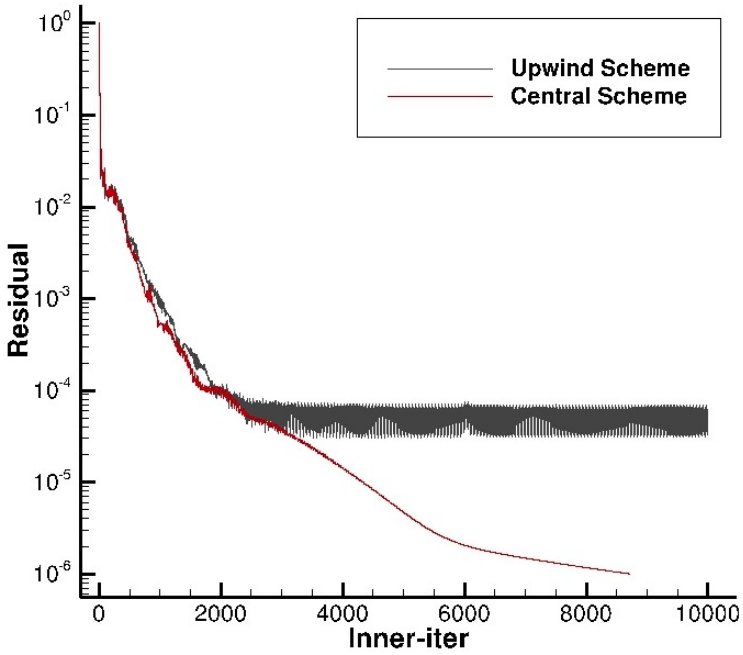

(a) Residual behavior using central and upwind schemes, at α = 13.5°and Spalart-Allmaras with Edwards modification turbulence model

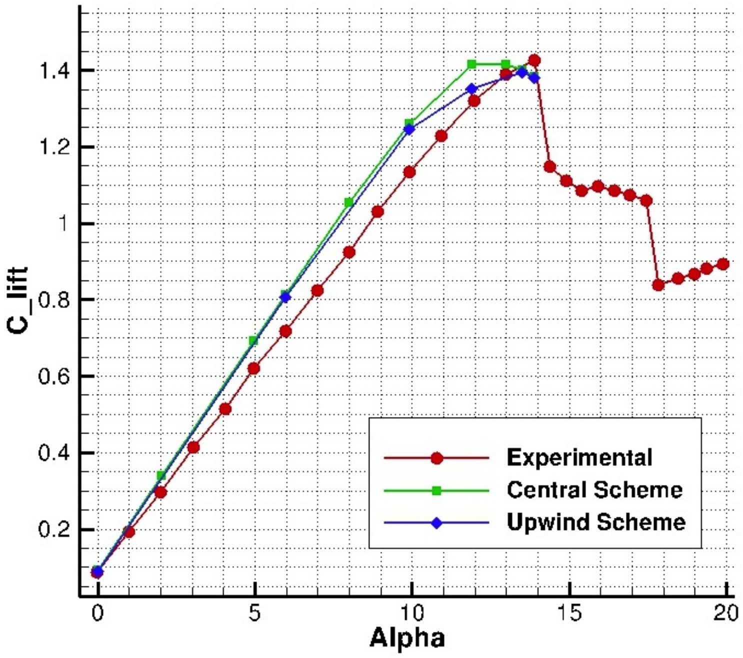

(b) Lift coefficient versus AoA using RSM, respectively with central and upwind schemes

Figure 5.8: Comparison between central and upwind schemes

5.3 Results

Concerning the Spalart-Allmaras turbulence model, two different version have been adopted: the original version and the model with Edwards modification. The differences relate mainly to the modeled near-wall behavior. The Edwards formulation avoids negative values of vorticity and is commonly identified as numerically more stable [17]. As apparent in fig. 5.9a, both models give approximately the same results. The stall angle and the maximum c_l is well described, with a further characterization of the post-stall flow. Also the plot of the lift coefficient versus the drag coefficient in fig. 5.9b is in agreement with the experimental curve. It is remarkable that these are the only configurations which under steady conditions are stable enough to describe the post stall behavior and to show the drop in the c_l of fig. 5.9a. This might be caused by the combination of the stable one-equation turbulence model and the *Coarse Mesh*, which probably solves only the biggest vortices without further complications in the solution of the smaller ones. Due to the higher numerical stability mentioned earlier, the version with Edwards modification will be adopted in unsteady computations.

5.3.1 Reynolds Stress Model

Regarding the RSM, several version have been adopted: RSM-SSG/LLR-ω with Menter Baseline, Wilcox stress-ω with Wilcox ω-equation and with Kok ω-equation (TNT model). As apparent in fig. 5.10, the RSM-SSG/LLR-ω with Menter Baseline version shows the best behavior, while the Wilcox stress-ω with Wilcox ω-equation reaches the desired convergence after many oscillations and with a double number of iterations, and the Wilcox stress-ω with Kok ω-equation does not get down under 10^{-5}. Thus, the first model version will be adopted from now on. Defined the RSM version used, it has been noticed that the residual was really hard to drop when AoA increases, resulting sometimes even in completely divergence. Further modifications of the *Coarse Mesh* has been performed trying to figure out the problem. In particular, it has been really useful the employment of the smoothing tool provided in ICEM-CFD, which after a quality check increases automatically the quality of worse elements. Obviously, new grids needed to be carefully inspected and further parameters to be set. At the end of this procedure, the grid shown in fig. 5.11 has led to good result in the description of the near-stall region. As it may be noticed in the figure, the smooth mainly introduced modified the spatial discretization in the rear region of the airfoil, increasing the total height of the structured layer. This detail will reveal to be important performing unsteady computation. In fig. 5.12 results obtained with this grid are displayed, exhibiting a better description when the static stall angle is approached compared with SAE results, though a slight anticipation of the stall event is visible both in lift and drag coefficients prediction. In fig. 5.12a, at $\alpha = 13°$ the improvement in c_l is $\approx 8\%$, while the use of upwind scheme further enhances the solution and the description of the slope variation. This is evident also in fig. 5.12b, where models using RSM are closer to the experimental curve.

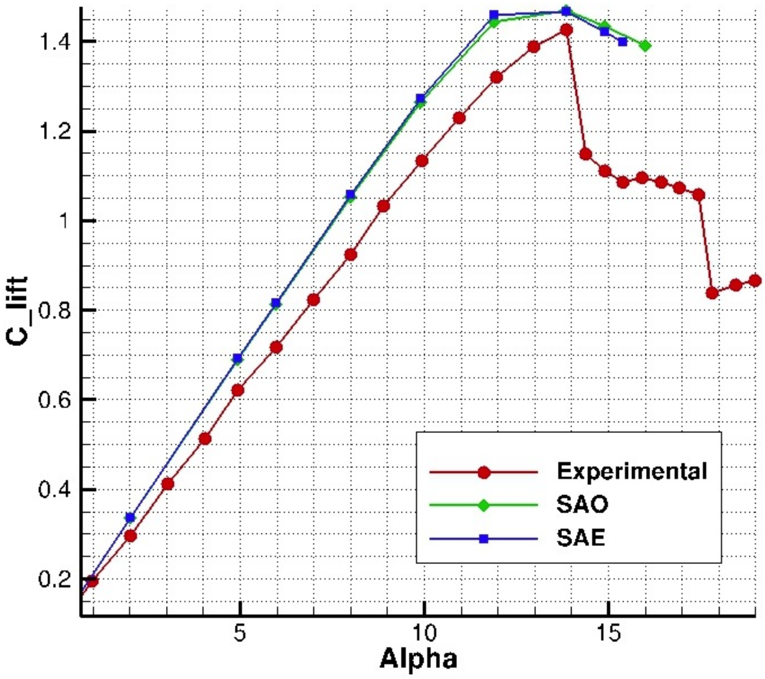

(a) Lift coefficient versus AoA

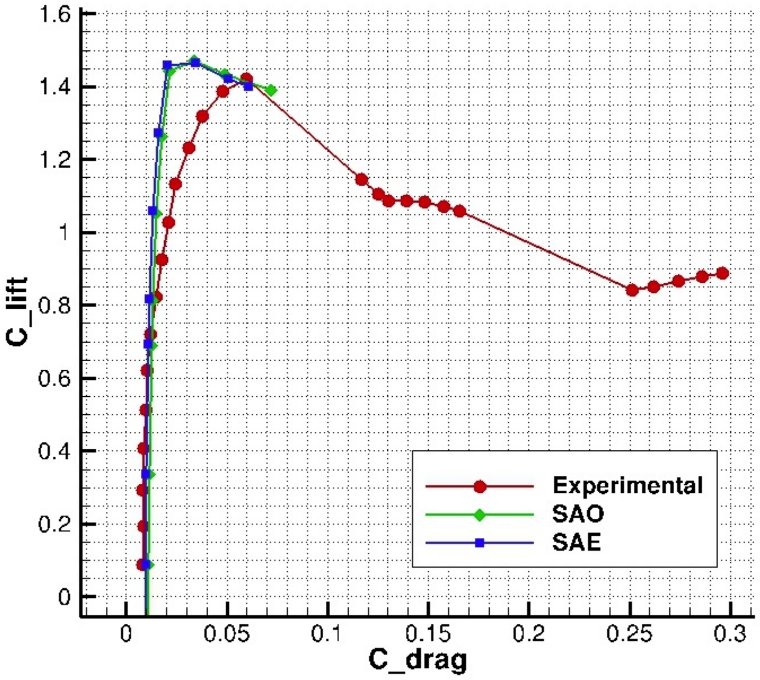

(b) Lift coefficient versus drag coefficient

Figure 5.9: Comparison between the original Spalart-Allmaras turbulence model (SAO) and the version with Edwards modification (SAE)

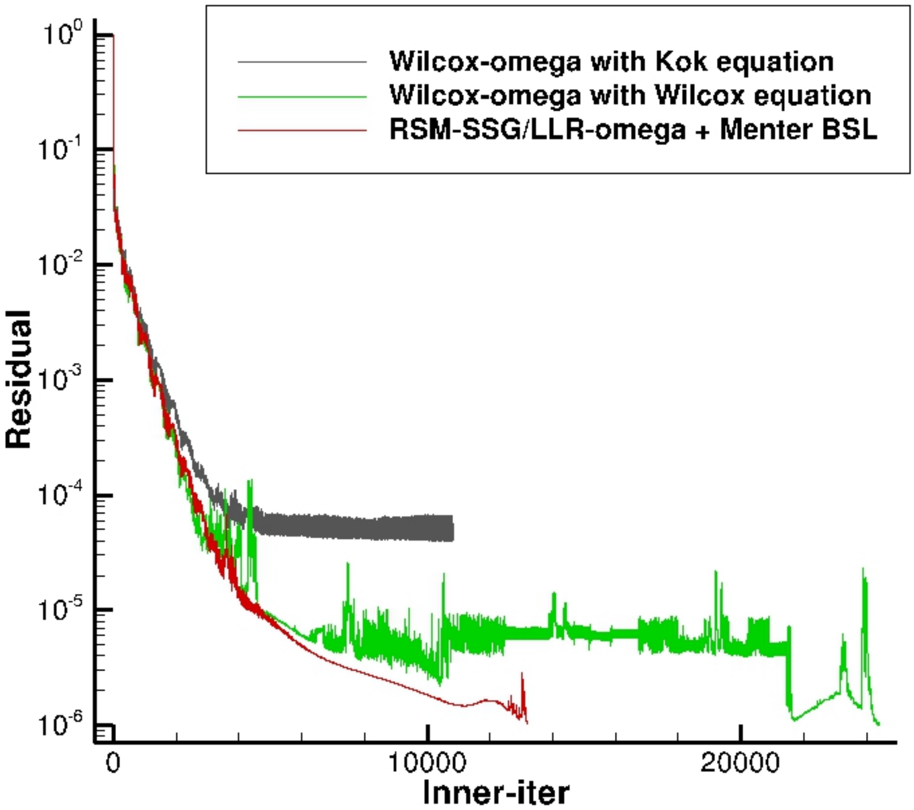

Figure 5.10: Residuals behavior of different RSM versions at $\alpha = 5.74°$

Results with *Fine1* grid are plotted in fig. 5.13, taking into account previous considerations about computational effort. The stall behavior is evidently better described by the RSM also with this grids, even though the percentage improvement is not so high as the previous case. Using a finer grid results in capturing smaller vortices, whose behavior is more difficult to describe under the restrictive conditions of steady flow. That might be the reason why the definition of the exact stall values of AoA and c_l has not been obtained using this grid. Nevertheless, the curves trend both in fig. 5.13a and 5.13b clearly respect the physical phenomenon.

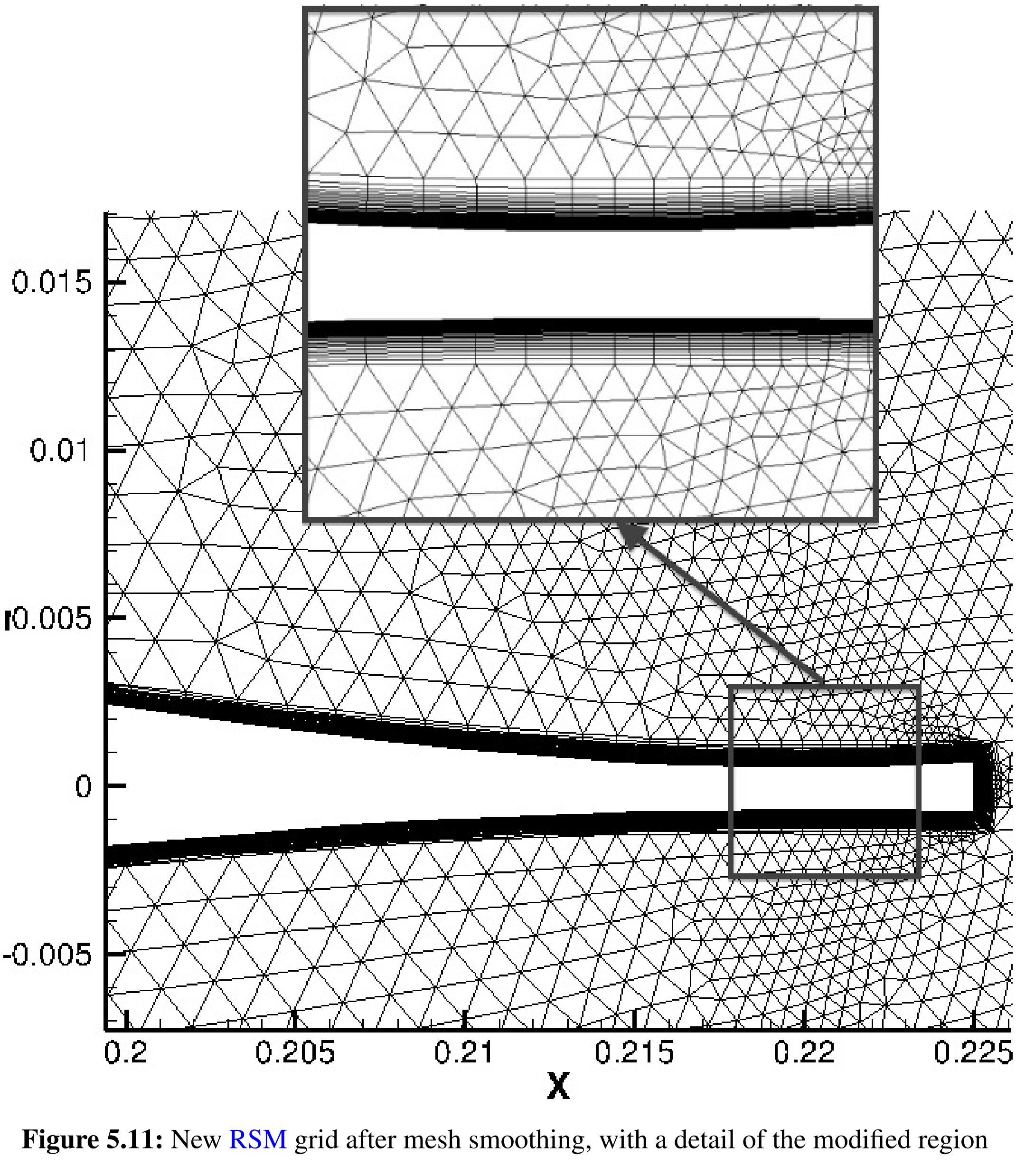

Figure 5.11: New RSM grid after mesh smoothing, with a detail of the modified region

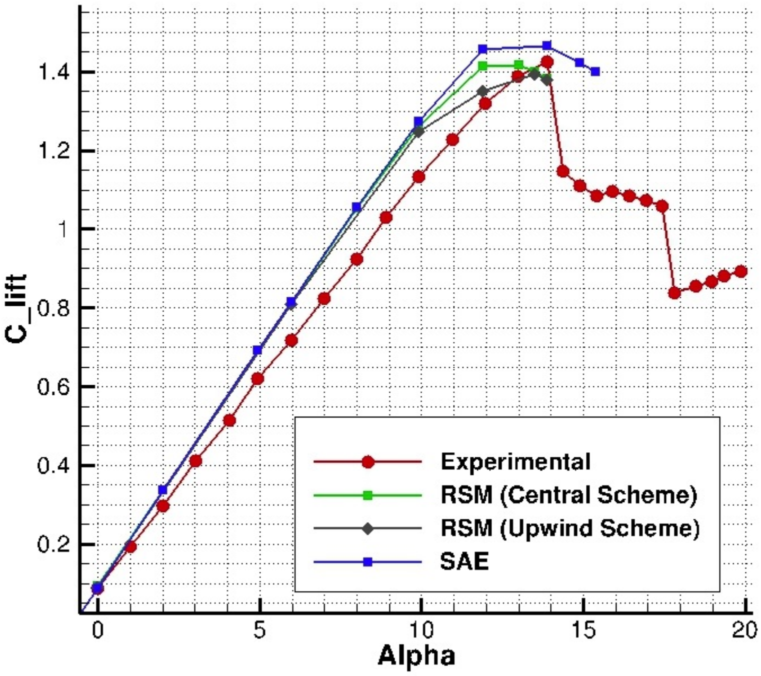

(a) Lift coefficient versus AoA

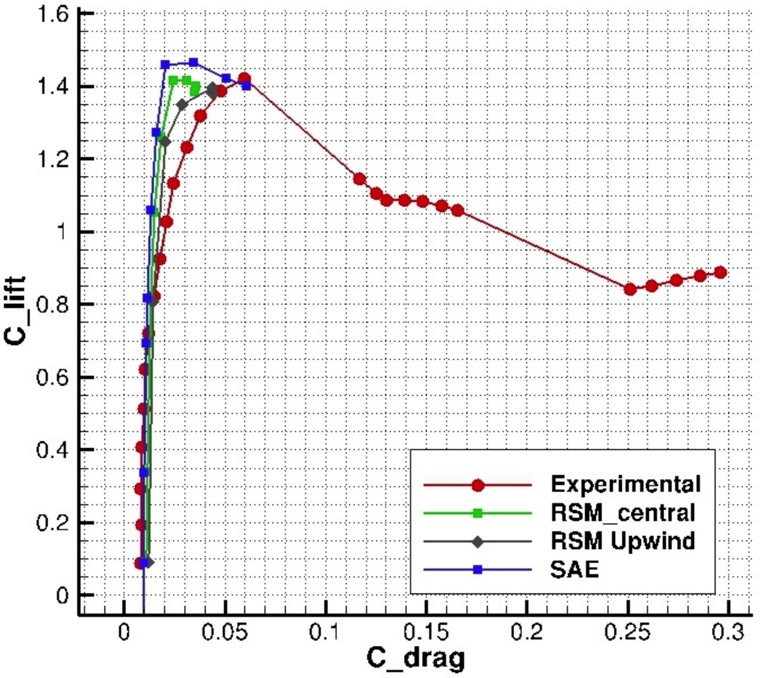

(b) Lift coefficient versus drag coefficient

Figure 5.12: Prediction of static stall with *Coarse Mesh* and different turbulence models

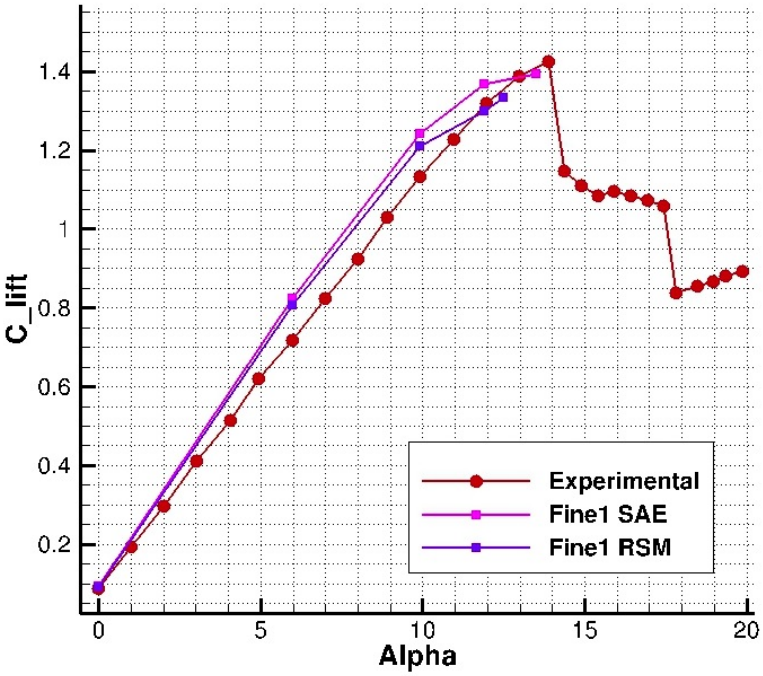

(a) Lift coefficient versus AoA

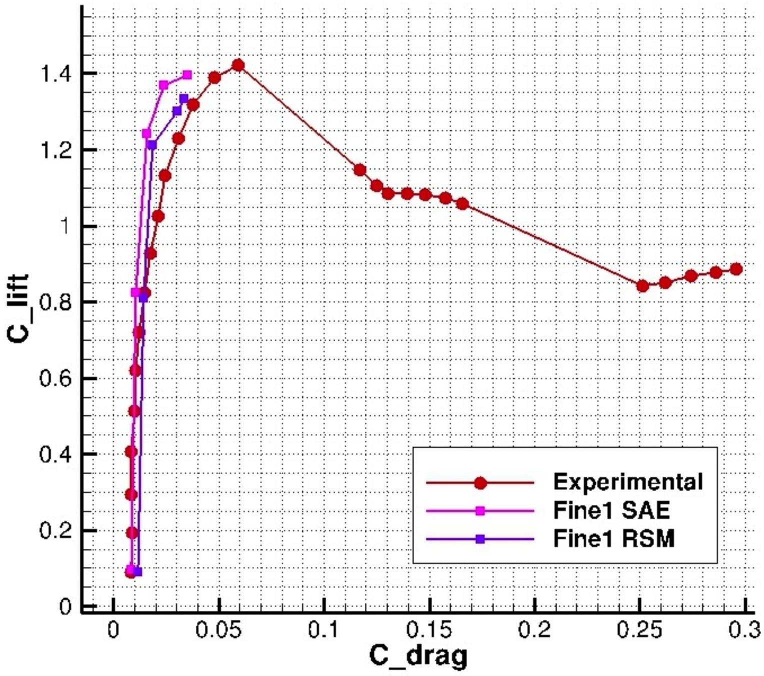

(b) Lift coefficient versus drag coefficient

Figure 5.13: Prediction of static stall with *Fine1* and different turbulence models

5.3.2 Flow Behavior

A visualization of the flow at four AoA is shown in fig. 5.14, where axial velocity and flow streamlines are plotted. As apparent, as the AoA increases, the velocity of the flow over the upper side of the airfoil (suction side) firstly increases and then decreases with respect to the well known airfoil theory. The flow is well attached to the airfoil until the static stall AoA is reached and detachment begins at α = 13.878°in fig. 5.14c. A low-speed region is now visible near the trailing edge, as well as the formation of a vortex due to flow recirculation. At α = 16.0°in fig. 5.14d, the flow is completely separated over more than the second half of the airfoil, and the recirculating region sheds from the trailing edge towards the leading edge.

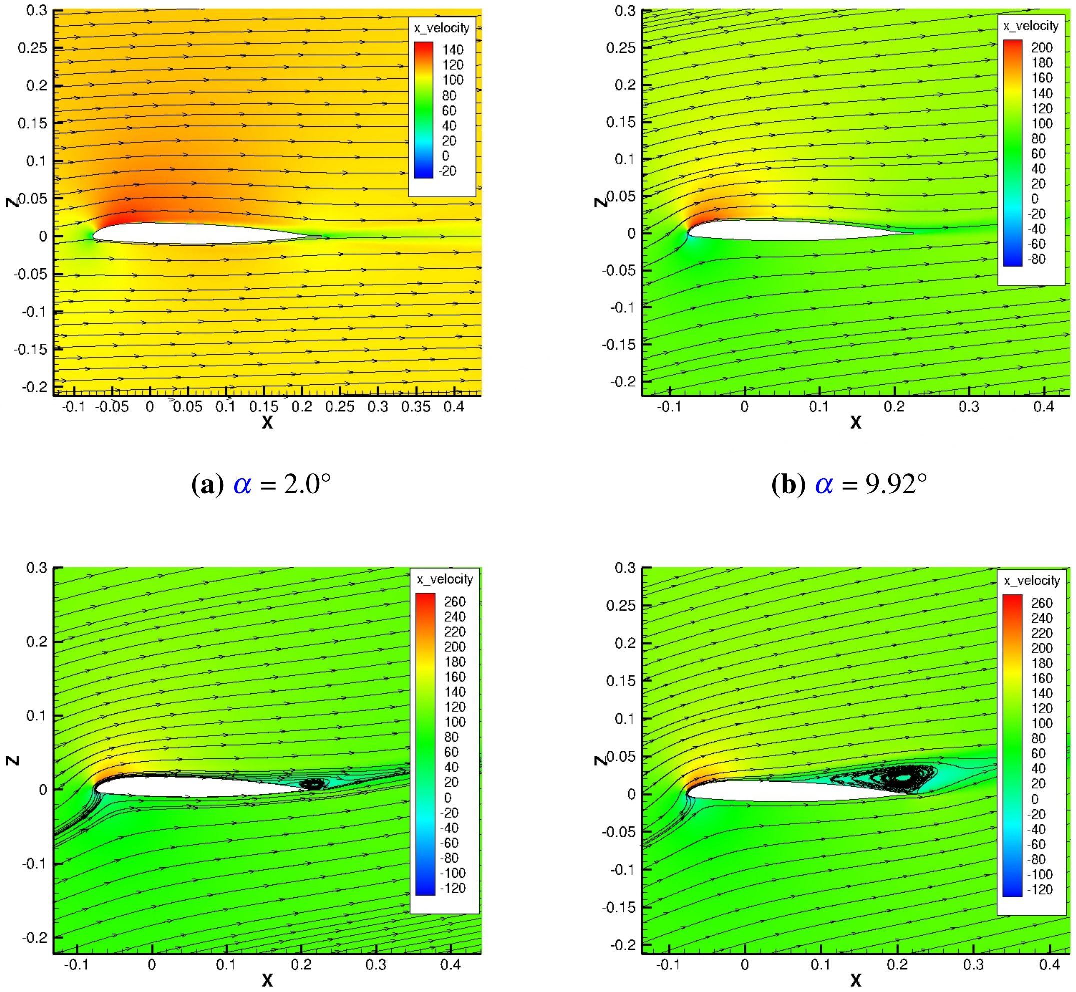

(a) $\alpha = 2.0°$

(b) $\alpha = 9.92°$

(c) $\alpha = 13.878°$

(d) $\alpha = 16.0°$

Figure 5.14: Axial velocity contours and flow streamlines at four different AoA, computed with SAE

5.3.3 Computational Cost

After results description, also computational cost plays an important role in CFD analysis and should be considered. In tab. 5.2 and 5.3 computational cost are presented, respectively using the grids *Coarse Mesh* and *Fine1*. It has been already pointed out that, in order to respect y^+ costraints, two different grids have been created for the two turbulence models, with a different first layer height. Nevertheless, comparison between computational time of Spalart-Allmaras Model with Edwards modification (SAE) and RSM is still possible, since the number of grid points of both grids is still of the same order. In tab. 5.2 it is highlighted that excellent convergence is reached in every computation. It is also observed that the number of iterations required using RSM is at least twice as high as what needed by SAE, and this value even increases for high AoA. Thus, the computational time is really different: for example, at α = 9.92° SAE model requires about 5 minutes to get convergence, while RSM results in a computational time of 40 minutes. Hence, the importance of the turbulence model choice is evident. In tab. 5.3 where*Fine1* grid is considered, the same tendency is pointed out and above considerations are equally valid. What it should be remarked is that the computational time is generally doubled due to the increase in number of elements. Furthermore, at high AoA the RSM shows a worse convergence, and residual does not go below the value of $1x10^{-5}$.

Table 5.2: Computational cost comparison at different AoA, using SAE and RSM with *Coarse Mesh*

COMPUTATIONAL COST WITH GRID *Coarse Mesh*				
ANGLE OF ATTACK	0°	5.97°	9.92°	13.878°
RESIDUAL CONVERGENCE REACHED				
SAE	$1x10^{-6}$	$1x10^{-6}$	$1x10^{-6}$	$1x10^{-6}$
RSM	$1x10^{-6}$	$1x10^{-6}$	$1x10^{-6}$	$1x10^{-6}$
NUMBER OF ITERATIONS				
SAE	5325	6243	7597	8674
RSM	10812	14793	25800	26086
COMPUTATIONAL TIME [S]				
SAE	225	265	322	368
RSM	990	1355	2364	2390

Table 5.3: Computational cost comparison at different AoA, using SAE and RSM with *Fine1*

COMPUTATIONAL COST WITH GRID *Fine1*				
ANGLE OF ATTACK	0°	5.97°	9.92°	13.5°
RESIDUAL CONVERGENCE REACHED				
SAE	$1x10^{-6}$	$1x10^{-6}$	$1x10^{-6}$	$1x10^{-6}$
RSM	$1x10^{-6}$	$1x10^{-6}$	$5x10^{-6}$	$1x10^{-5}$
NUMBER OF ITERATIONS				
SAE	10351	7634	9400	11920
RSM	12786	17543	26313	30000
COMPUTATIONAL TIME [S]				
SAE	553	385	478	595
RSM	1662	2281	3420	3900

6 Dynamic Stall CFD Predictions

In this chapter flow unsteady conditions and airfoil oscillation are introduced. Therefore, the airloads prediction becomes a dynamic problem, where unsteadiness in the flow and grid movement have to be considered, through a series of expedients and further setting of new parameters. The type of grid movement adopted is a rigid body motion, where no grid deformation is introduced and basically the flow direction changes with time. A python script is then used to rotate the coordinate system in order to provide flow pictures hereinafter presented. Besides this, it is evident that when the computation starts and the first timestep is solved, the airfoil is perceived in a static position since no previous timestep gives informations about dynamism in the movement. This situation produces an odd value of the lift coefficient, which clearly affects the first part of the cycle in fig. 6.1. In order to overcome the problem, in this thesis every computation performs three periods, and only the airolads of the last period are exhibited. Thus, the effect of static initial conditions are removed, and the solution describes with more accuracy both the slope of the initial part of the cycle, eliminating the c_l error marked in figure, and also position and magnitude of the two lift peaks.

6.1 Temporal Discretization

Several time stepping schemes are available in TAU to perform unsteady computations. The approach which is currently the most widespread in complex flow problems is the *Dual-Time Stepping Scheme*. A comprehensive survey may be found in the review papers of SHUEN et al. [62] and MERKLE et al. [52] This procedure, which has been succesfully adopted in many recent works, is here employed with a second order backwards difference operator.
In CFD analysis, unsteady problems are computed defining a timestep size (Δt), and discretizing the period of the oscillating cycle (T_{cycle}) with a certain number of physical timesteps (n_t = $T_{cycle}/\Delta t$). The Dual-Time scheme involves an inner iteration loop in pseudotime that is wrapped by an outer loop stepping through physical time. Thus, the flowfield at each physical time level may be treated as a steady-state problem in pseudotime, with appropriate source terms to provide an influence of the flow history on the current time level. In this way, the pysical timestep size is not affected by the stiffness of the system, whereas convergence of the inner iterations in pseudotime is optimized by any convergence enhancement technique normally used for steady flows.

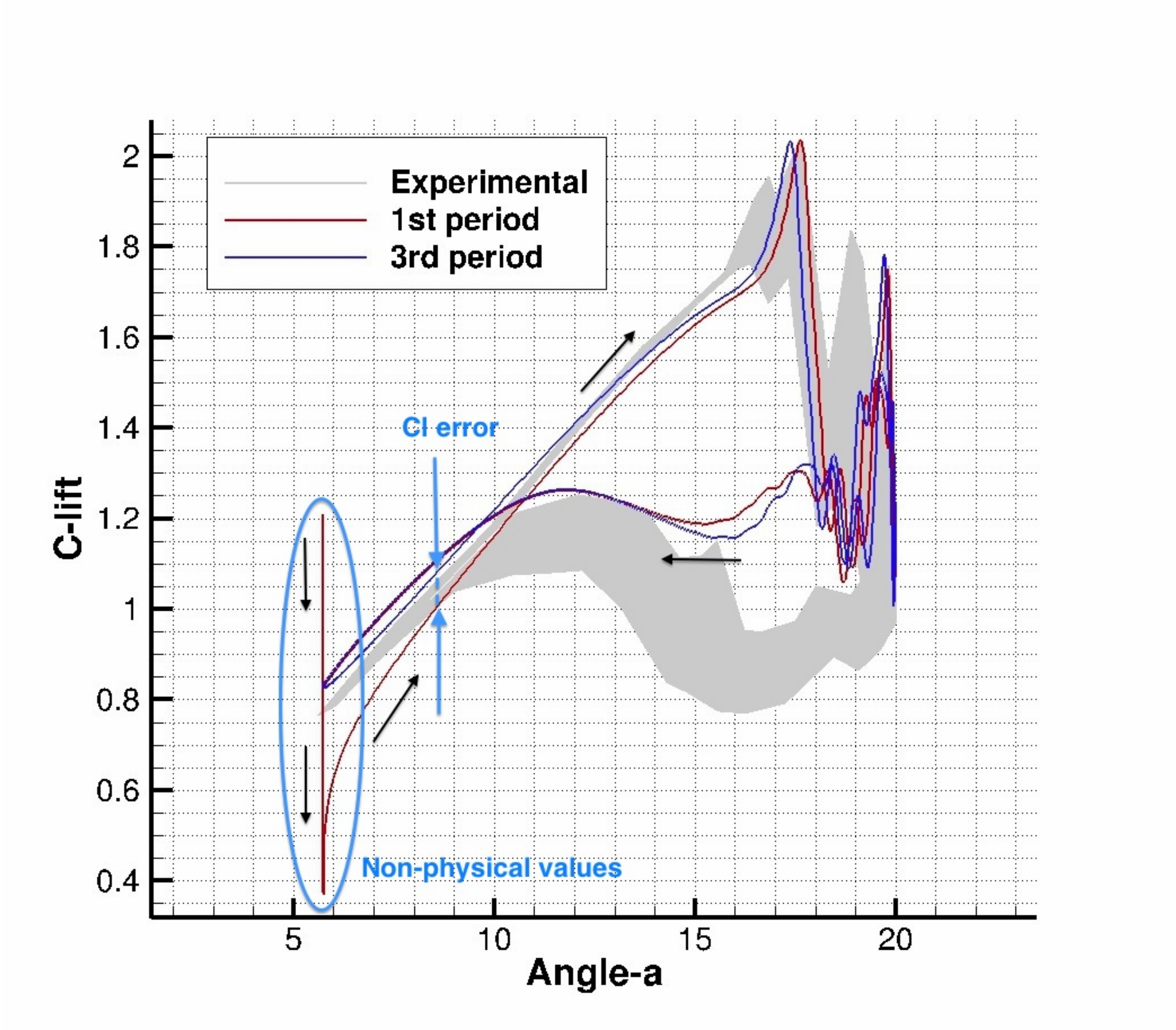

Figure 6.1: Influence of the initial conditions: comparison between the first and the third period

6.1.1 Temporal Resolution Study

A study of the ideal temporal discretization is necessary in every kind of unsteady flows prediction. Moreover, during dynamic stall a wide range of time scales are present and the temporal resolution, as well as the timestep convergence, plays a key role in the accuracy of the solution.
In order to study the ideal temporal resolution necessary to reach temporal convergence for the entire dynamic stall period, several timestep sizes have been adopted in different models computed. The number of inner iterations is set to an high value; this choice is possible mainly thanks to the computational power available. Therefore, the number of inner iterations used in this thesis is 5000, value arbitrarily selected considering the number of iterations needed to reach convergence in steady computations. It should be immediately pointed out that this value may be significantly reduced in a practical approach, with a consequent saving of time. Effectively, the temporal convergence is reached already using 600 subiterations with the Spalart-Allmaras turbulence model. The main reasons to employ a such high number of inner iterations are listed in the following:

- First, an excellent convergence at each time step is reached ($1\text{x}10^{-6}$), ensured by the individual convergence of lift, drag and pitching moment.

- Second, the number of inner iterations necessary for a temporal convergence is different for each turbulence model. Imposing a high number allows to use the same setting for both turbulence models.

- Third, logic would dictate that when the number of physical timestep increases, the number of inner iterations should decrease in order to have the same computational time. Keeping a permanent high number of inner iterations leads to a real analysis of the physical timestep influence.

At this stage should be made clear that in this thesis accuracy is privileged compared to practical characteristics such as time taken or computational effort.

In this temporal resolution study, the number of the physical timesteps assumes four different values: 500, 1000, 1500 and 2500. As apparent in fig. 6.2, the first model already correctly describes the phenomenon, capturing both the first and second stall peaks. When the n_t increases at a value of 1000, the improvement in the first stall prediction is equal to $\approx 2\%$, so practically negligible. Conversely, a better second stall prediction is noticed, with an improvement in the c_l peak prediction of $\approx 8\%$. Also the reattachment phase better matches the curve of experimental data. Further increases in the number of timesteps show that computations converge in time to the same solution, proving a certain independence from the temporal resolution. The number of physical timestep adopted to perform unsteady conputation is 1500, also in order to provide a certain safety margin in the use of RSM.

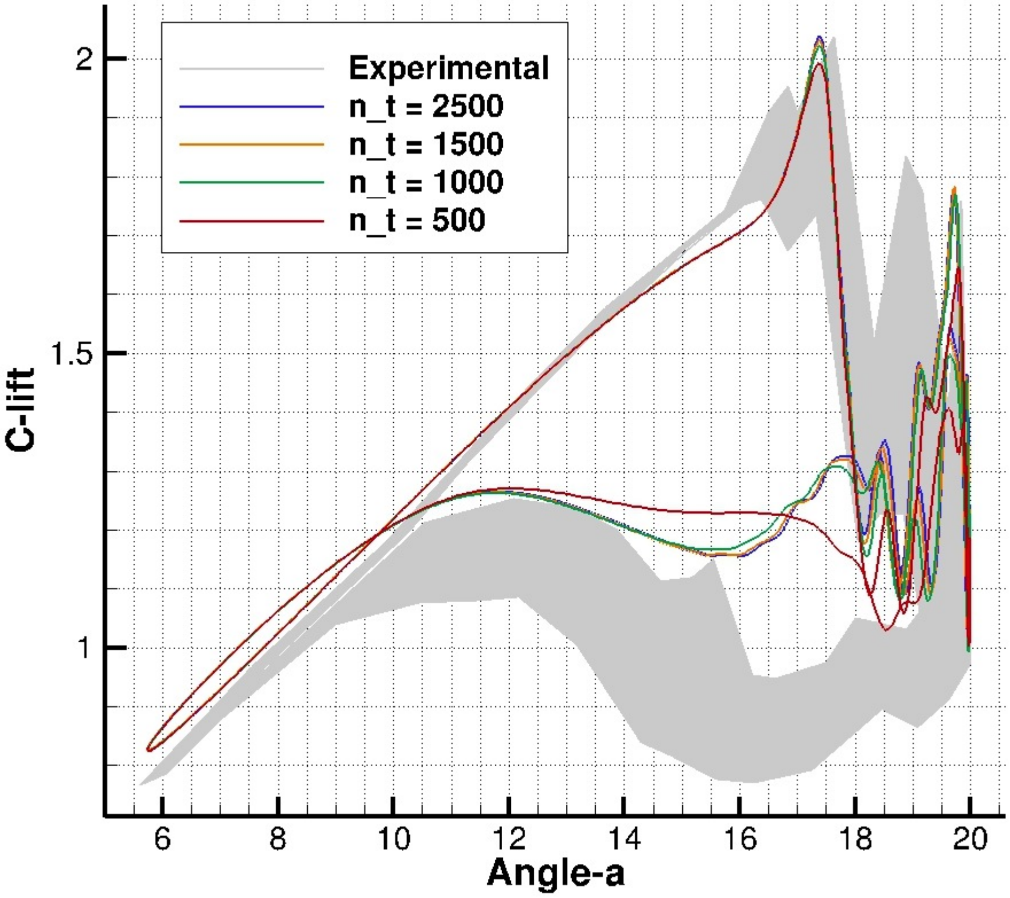

Figure 6.2: Lift coefficient prediction with different timestep values, using the *Coarse Mesh* with SAE

6.2 Results

As already mentioned in the previous chapter, all grids defined in section 5.1.1 are computed also under unsteady conditions. In fig. 6.3 the three grids are compared, adopting the Spalart-Allmaras model with Edwards modification. It may be immediately noticed that the *Coarse Mesh* seems to give an accurate prediction of the phenomenon, in spite of the scant number of elements. In fig. 6.3a, both the c_l magnitude and the AoA at which the first stall occurs match the experimental data, and also the second stall event is clearly defined. After these considerations, the first mesh shows a completely different behavior during the flow reattachment. When the AoA begins to decreases a sudden c_l peak is visible and, after that, all coefficient values deviate considerably from experimental data, suggesting a failure in reattachment description.

Comparing this result with the *Fine1* grid, fig. 6.3a shows that the grid refinement improves the accuracy of reattachment prediction, while the second stall peak decreases significantly. The computation with the *Fine2* reveals a convergence to the latest solution. This may be observed also in fig. 6.3b, where the pitching moment coefficient is displayed. The c_m negative peak describing second stall event is considerably reduced using the finest grids, and the flow reattachment is predicted with less oscillations. This discrepancy between the two results is completely unexpected, since from a refinement of the grid an improvement in all aspects of the solution should derive. This behavior respect to the grid resolution suggests that the excellent prediction obtained with the first mesh might be the outcome of a lucky circumstance, at least as regards the second stall. This is probably caused by a failure to capture and solve the smallest vortices, which play a fundamental role after the main stall event. In particular as previously mentioned, since some flow features occurring during the multiple vortex shedding after main stall and during flow reattachment take place inside the structured grid, the higher surface resolution on the airfoil of *Fine1* grid turns out to be necessary for a correct prediction. For these motivations, *Coarse Mesh* results are discarded and only the *Fine1* is considered as reliable. Concerning the *Fine2* grid, as previously stated during steady computations, it does not exhibit a sufficient quality improvement to justify the higher number of elements used. At this point, it should be highlighted the really good accuracy in airloads prediction during first stall, that, expecially regarding the pitching moment coefficient, has been extremely difficult to get in previous works.

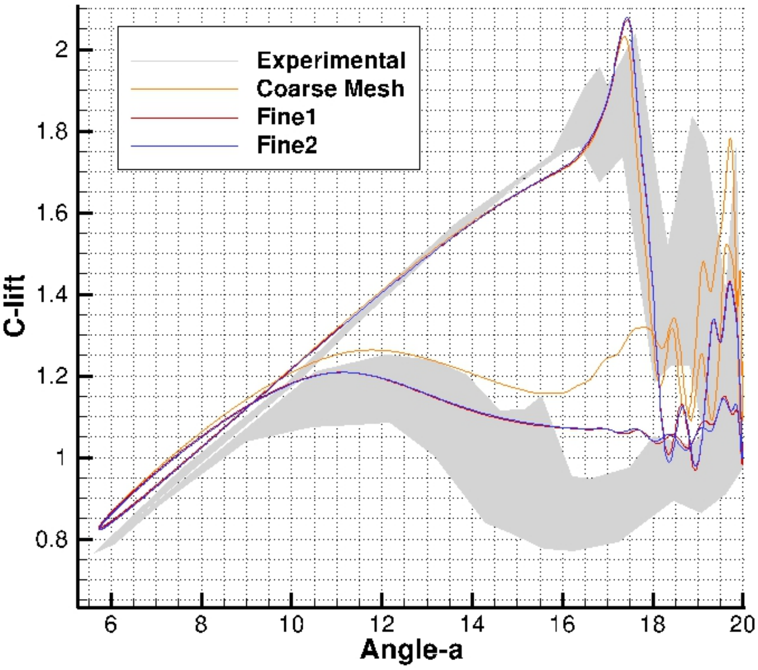

(a) Lift coefficient versus AoA

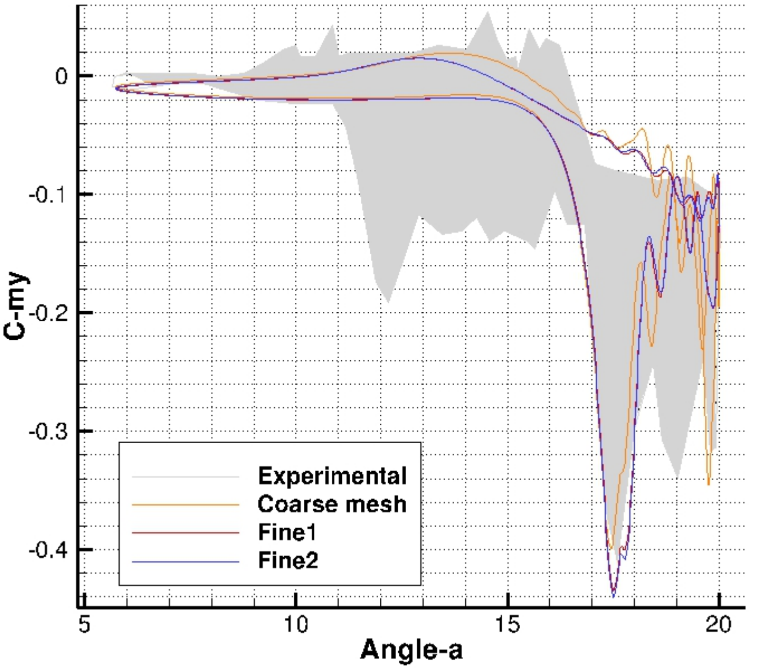

(b) Pitching moment coefficient versus drag coefficient

Figure 6.3: Lift and pitching moment coefficients prediction with different grids, computed with SAE

6.2.1 Rotational Correction

Concerning the one-equation RANS closures, the key ingradient in this class of model is the adoption of the linear Boussinesq stress-strain hypothesis in correlating mean velocity field gradients to the fluid stress. There are well-known deficiencies of this hypothesis [70], particularly with respect to flows which experience mild to severe streamline curvature influences, adverse pressure gradients, system rotation and three-dimensional effects. SPALART and SHUR proposed a modification to the Spalart-Allmaras model to account for streamline curvature and system rotation [63]. The approach involves second-order derivatives of the velocity field. In short, the Spalart-Allmaras model with rotational correction (SARC) consists of a modification to the source term that is multiplied by a rotation function, provided in literature [16][32].

The definition of the SARC as vortical correction model solving the dynamic stall problem leads to some considerations, and a comparison between airloads predicted with and without rotational correction is shown in fig. 6.4. As may be seen in fig. 6.4a, the AoA at which both the first and second stall occur decreases compared to previous computations, as well as the magnitude of both lift coefficient peaks. This prediction, altough different from the previous one, anyway turns out to be in agreement with experimental cycles. A further improvement is also introduced in the description of the flow reattachment. Regarding the pitching moment coefficient, the mainly difference is a prediction of the first c_m drop at a lower AoA. This first stall anticipation worse fits with experimental data, which in all measurements are more in agreement with the model without rotational correction, as visible in fig. 6.4b.

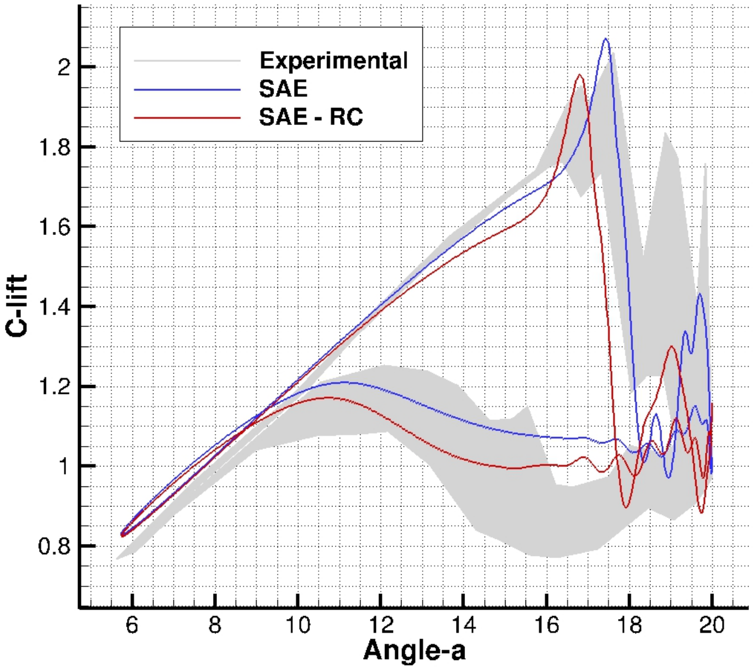

(a) Lift coefficient versus AoA

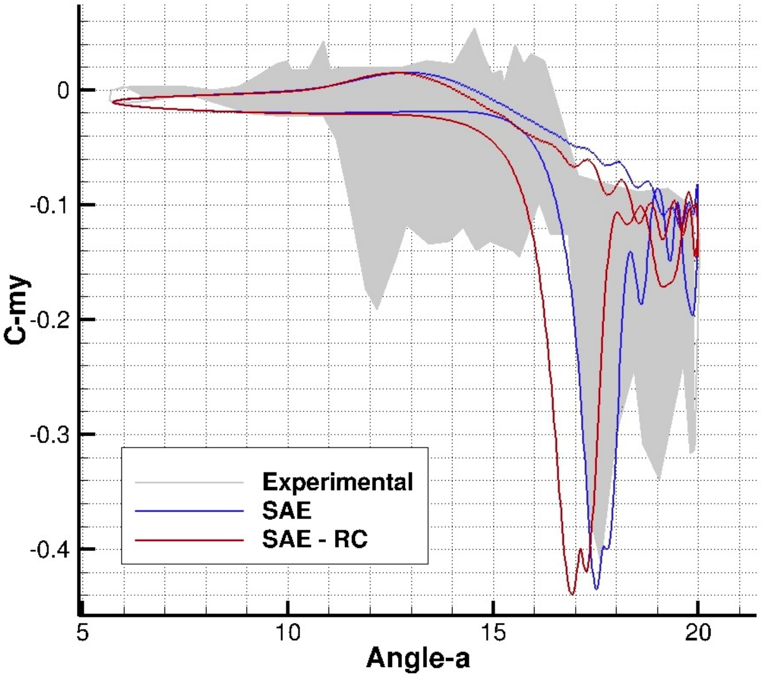

(b) Pitching moment coefficient versus drag coefficient

Figure 6.4: Results of Spalart-Allmaras model with and without rotational correction

6.2.2 Reynolds Stress Model

Obtaining good results with RSM has proved to be a difficult task. Results with the *Coarse Mesh* show that, despite the good prediction obtained under quasi-static conditions, the low number of elements are not sufficient to describe the flow behavior after the first stall, resulting in a non-physical lift coefficient trend. In fig. 6.5a prediction with RSM is shown and the lift coefficient is marked with different colours depending on whether the AoA increases or decreases. In the first part of the cycle it may be notice that the magnitude of the first stall event is slightly under-predicted, while second stall is strongly over-predicted. Moreover, when the AoA begins to decrease an unexpected peak in the lift coefficient is visible, and a further high c_l value is again predicted at about 16°. Then, the lift coefficient gets back to normal values and reattachment occurs. The peaks observed can not find a physical explanation, implying a totally wrong prediction. Computing *Fine1* and *Fine2* grids reveals a tendency to fail after the first stall event, resulting in residuals divergence. In fig. 6.5b the first period of both grids is plotted. The *Fine1* diverge once the AoA begins to decrease, describing also unreal peaks magnitude, since second stall leads to higher c_l values than first stall. The *Fine2* computation even failed in the description of the second stall event. Thus, a new evaluation of the analysis parameters is necessary and the validation under steady condition is brought into question, at least concerning prediction with RSM. This is not surprising: it should be remembered that the unsteady dynamic stall phenomenon assumes completely different characteristics than the static stall, both in terms of flow complexity and higher computational effort required.

What emerges from in-depth analysis of different setting, study of single parameters influence and computation of several models, can be summarized with the following considerations:

- As mentioned during the steady validation, the upwind scheme is often unsuitable with complex flow problems. Solving dynamic stall, it leads to large problems of instabilities, while it is clear that the central scheme provides the right stability, thanks to the artificial dissipation inside the scheme, with an accuracy good enough for an accurate prediction.

- Multigrid method exhibits strong incompatibilities with the unsteady solution in dynamic stall. Accelerating the convergence with this technique leads to an incomplete resolution of the flowfield, that is necessary to correctly describe full separation and reattachment.

- Convergence at each single timestep is of primary importance. Second stall event is correctly described only if minimum residual parameter is set to 10^{-6}.

Altough these considerations, models computed until this point are unable to describe the fully separated flow and the reattachment process, even if an appreciable prediction of the second stall event is observed. Hence, a modification of the grid turns out to be necessary: two different strategies have been adopted and are presented below.

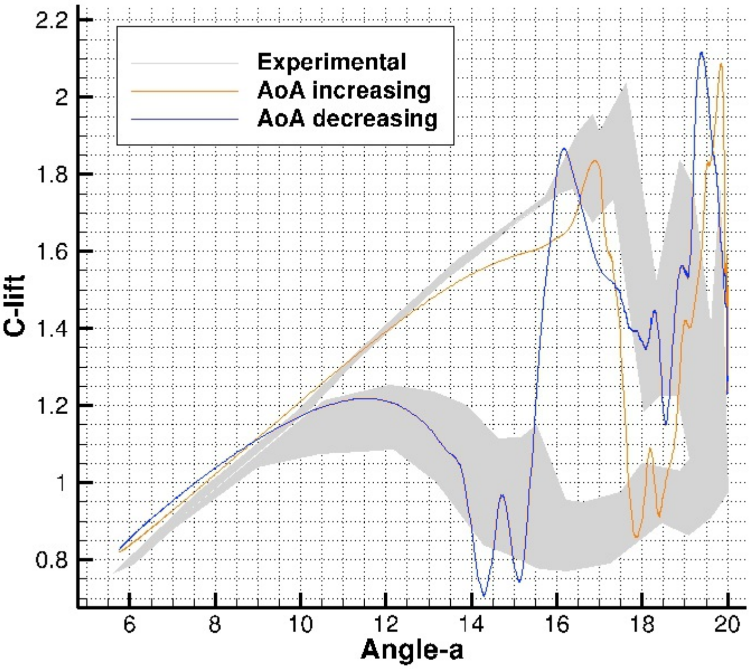

(a) Prediction of RSM using the *Coarse Mesh*

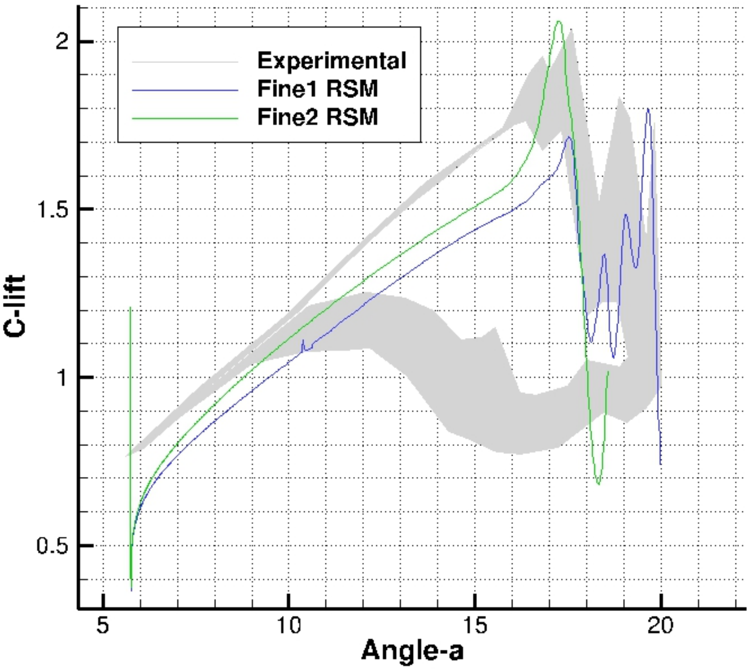

(b) First period prediction of RSM with *Fine1* and *Fine2* grids

Figure 6.5: Different failures in RSM first period prediction using all grids

Increase in grid points

The observation that grids created until now might be not fine enough to correctly describe a such complex phenomenon like dynamic stall when associated to equally complex RSM is more than plausible. In fact, previous grids failed in the prediction of flow behavior after flow separation, where small vortices appear. It is logical to think that a further grid refinement might better describe the flowfield in these conditions. Thus, the first strategy evaluated is the definitive increase in number of grid points. In order to obtain a grid with a good quality, the modification of some meshing parameters is necessary, taking into account what previously observed in section 5.1.

First, a different definition of the high concentration region around the airfoil is employed. As shown in fig. 6.6, it has been used a trapezoidal area, which better follows the phenomenon evolution. This choice allows refinement where the flow is affected by separation, that is downstream the airfoil, with a bigger element size where high spatial resolution is not necessary. Second a high number of grid points is set, giving particular attention to the spatial discretization near the trailing edge. The properties of the new grid generated, defined as *Fine3*, are reported in tab. 6.1.

Here, it is important to highlight that this grid leads to prohibitively high computational times, despite the available computational power. Performing three entire oscillating periods required a running time of about 14 days. Several further adjustments have been made to smooth the grid and overcome divergence problems and the final plot is reported in fig. 6.7. As visible, *Fine3* grid results during upstroke are quite good, with a noticeable c_l over-prediction in first stall, but a really good description of second stall event, both in terms of magnitude and position. Nevertheless, at the end the trend of the lift coefficient shows again a failure in predicting the reattachment process, with the presence of the two non-physical peaks as what observed with the *Coarse Mesh*.

Table 6.1: Characteristics of *Fine3* grid computed with RSM

GRID CHARACTERISTICS	
PARAMETER	Fine3
Surface resolution	0.25%
Number of nodes (2D)	745688
Number of elements (2D)	2084526
Computational time (50 iterations)	4.35 [s]

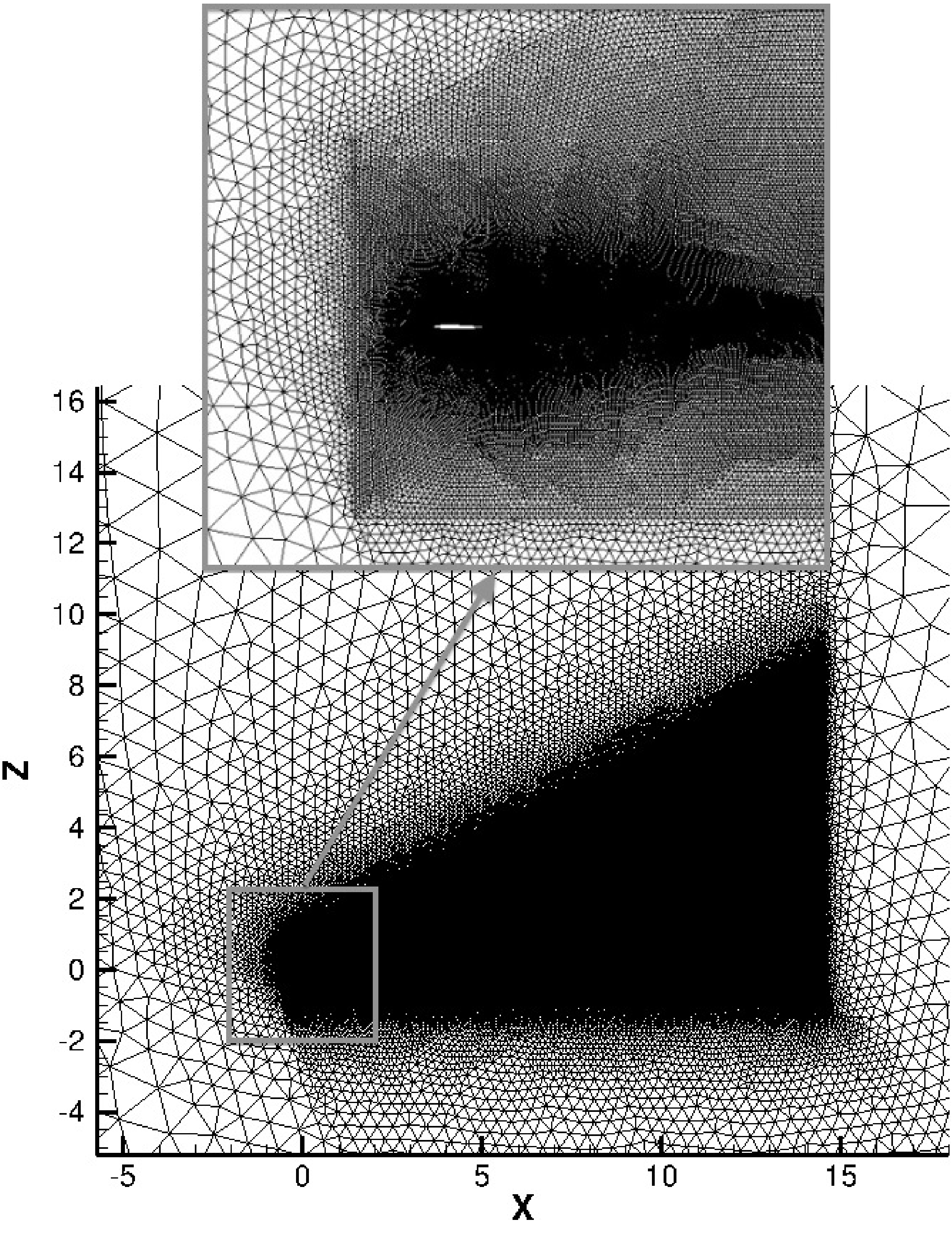

Figure 6.6: Outer field definition in grid *Fine3*

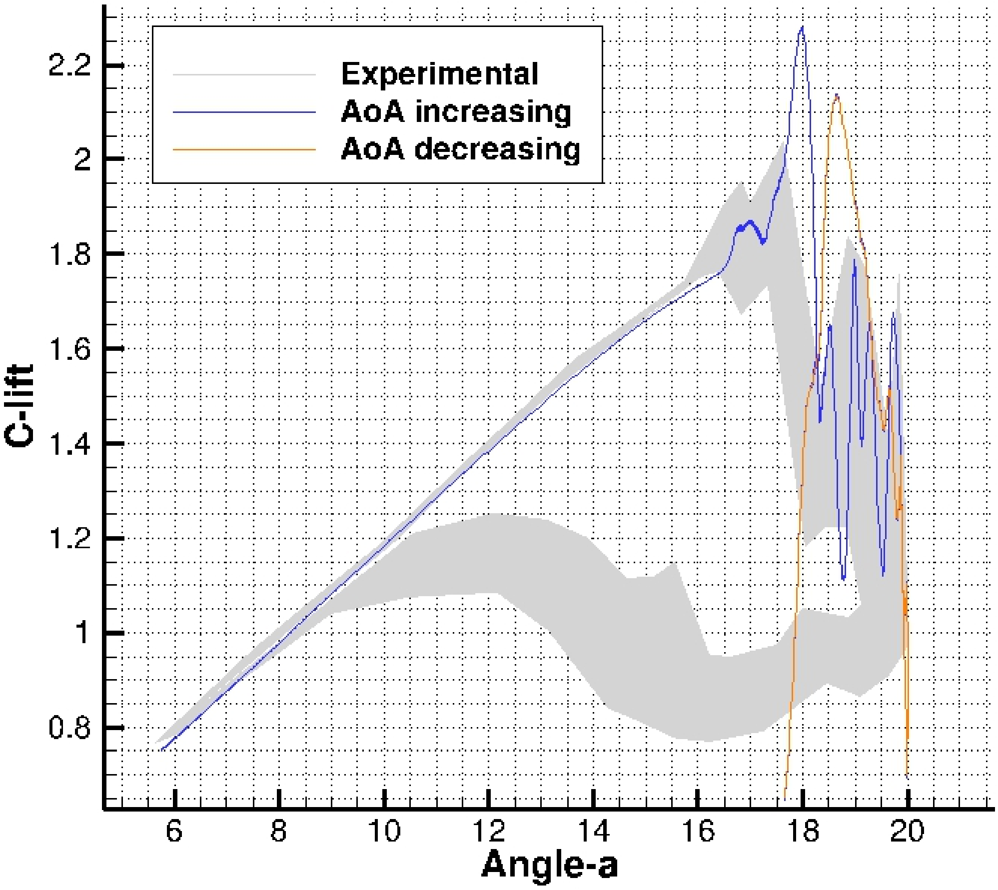

Figure 6.7: Outer field definition in grid *Fine3*

Height Variation of the Structured Region

Last results show that an acceptable solution have been obtained in dynamic stall prediction also using RSM, but problems occur computing the reattachment. As previously mentioned several times during this thesis, particular flow features occurring during second stall and especially reattachment are located very near the airfoil surface. Thus, this region is dicretized with structured elements, in order to solve such complex flow configuration. Repetetive failures in reattachment prediction might suggest that the structured region is not wide enough to fulfill this task. Hence, the second strategy is the height increase of the structured region through modifying the layers height ratio, with a resulting final thickness approximately twice the one of *Fine1* grid. This is clearly visible in fig. 6.8 and 6.9, where details of leading edge and trailing edge of both grids are shown. The outer field is the same of grid *Fine3*, except for the number of grid points which has been considerably reduced to prevent excessive computational time. Even so, the grid is much finer than *Fine3*, with a elements concentration more focused where it is necessary, thanks to the trapezoidal area already defined. The new grid created, named *Fine4*, has the properties reported in tab. 6.2.

Results with *Fine4* grid are plotted in fig. 6.10, comparing airloads prediction with what previously obtained using Spalart-Allmaras model with Edwards modification. In fig. 6.10a, when first stall occurs the lift coefficient shows an over-prediction of the magnitude and a slightly delay of the event to an higher angle of attack. Conversely, second stall description exhibits a very good accuracy, much better than SAE prediction. During downstroke the curve trend is similar to experimental results, although numerical values are higher and the reattachment path is different. Concerning the pitching moment coefficient, fig. 6.10b shows again an over-prediction of the two stall negative peaks, with the first one particularly evident. It is well known that getting c_m good results is a much more difficult task compared with c_l prediction. Nevertheless, except for first stall magnitude, results have an acceptable quality in the prediction of second stall and reattachment process.

Table 6.2: Characteristics of *Fine4* grid computed with RSM

GRID CHARACTERISTICS	
PARAMETER	Fine4
Surface resolution	0.25%
Number of nodes (2D)	304236
Number of elements (2D)	764764
Computational time (50 iterations)	1.73 [s]

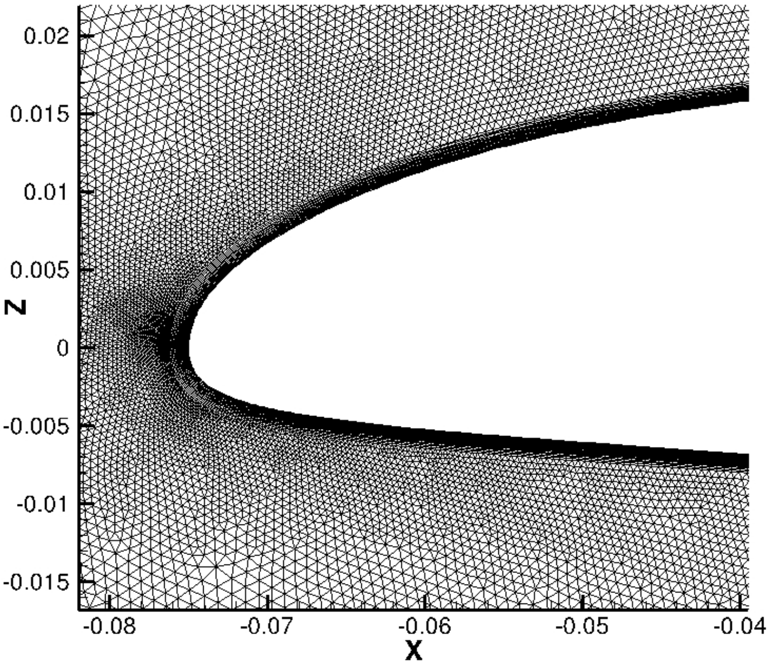

(a) *Fine1*

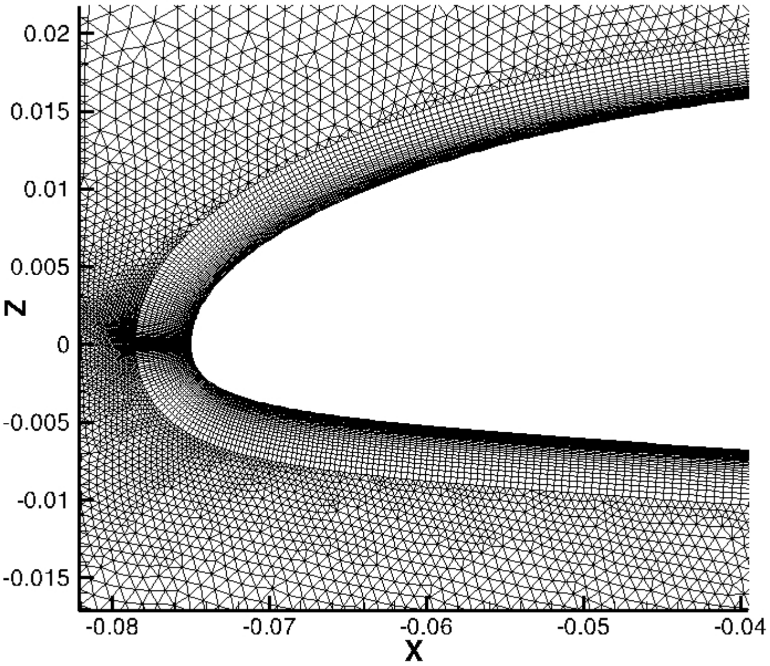

(b) *Fine4*

Figure 6.8: Leading edge details of *Fine1* and *Fine4* grids

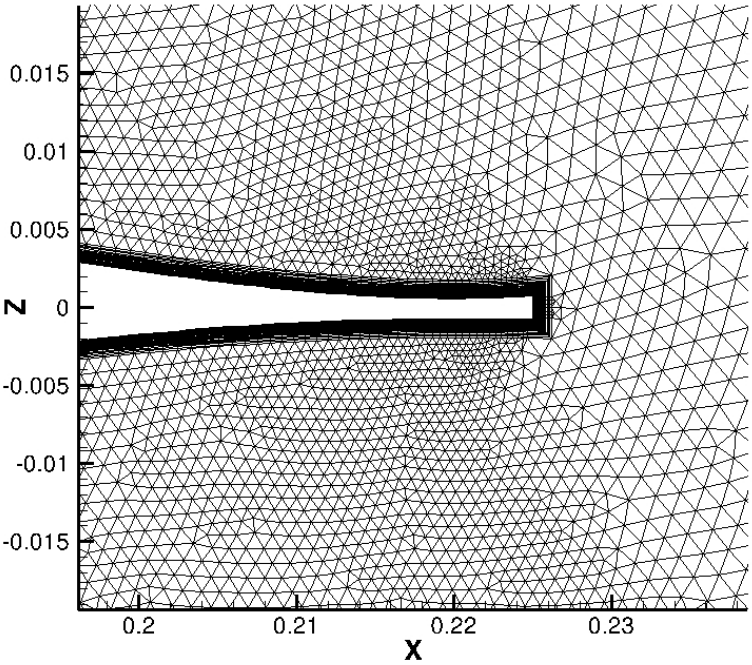

(a) *Fine1*

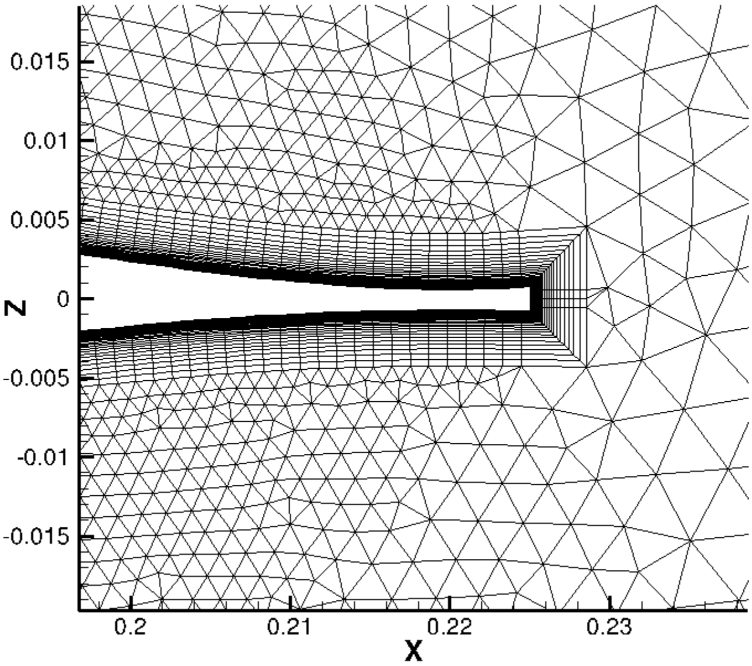

(b) *Fine4*

Figure 6.9: Trailing edge details of *Fine1* and *Fine4* grids

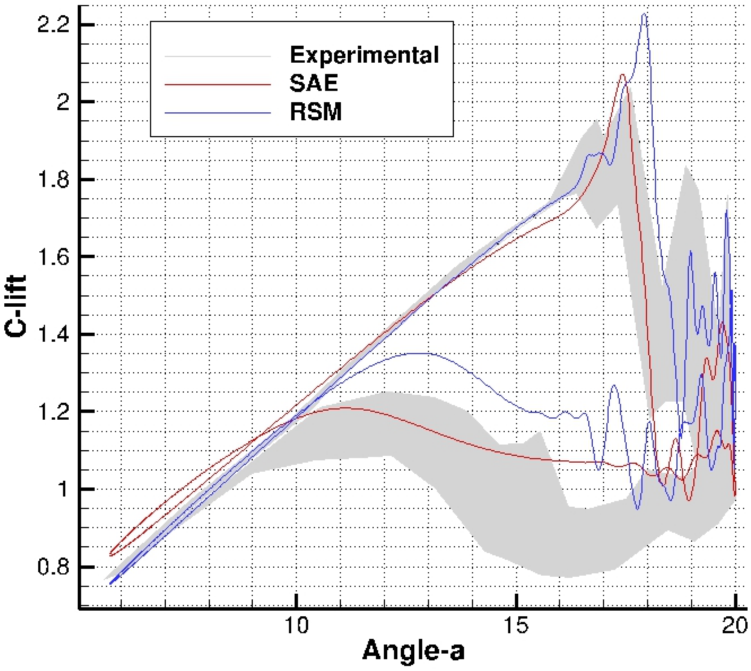

(a) Lift coefficient versus AoA

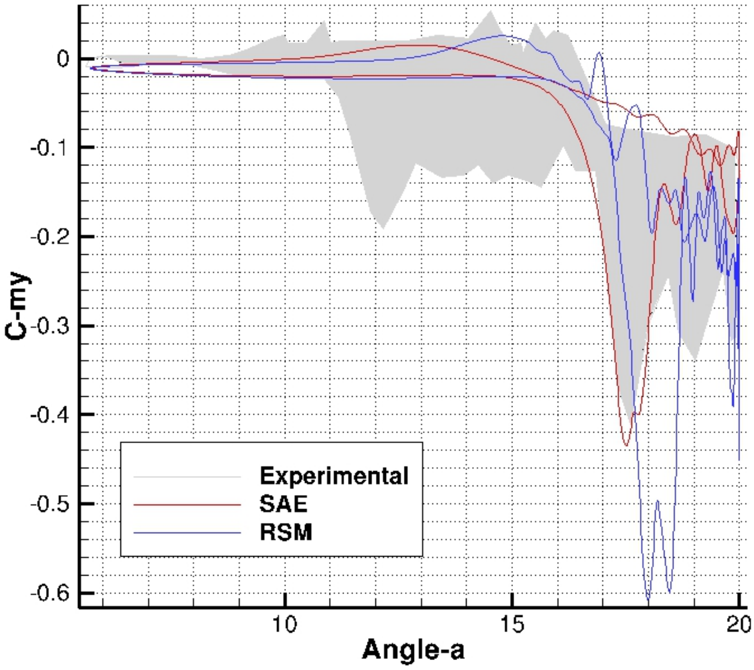

(b) Pitching moment coefficient versus drag coefficient

Figure 6.10: Lift and pitching moment coefficients prediction with *Fine4* grid computed with RSM

6.2.3 Flow behavior

Flow features occurring during dynamic stall have been described in detail during chapter 2. In this section results with RSM are graphically shown in terms of Mach number field and flow streamlines, pointing out in fig. 6.11 the different stages of the phenomenon.
In fig. 6.12, the flowfield is shown at an AoA much higher than the static stall angle, but it is evident that the flow is still well attached to the airfoil surface. Focusing on the leading edge region, it is possible to notice the generation of the leading edge vortex (LEV), which causes the delay of separation onset and the extra-lift visible at stage 1 in fig. 6.11. With a further increment of the AoA, this vortex quickly grows and spreads over the airfoil while the lift coefficients continuosly increases, as shown at stages 2 in fig. 6.13. When the LEV reaches the trailing edge and detaches from the airfoil, a sudden drop in c_l occurs at point 3. After this event, at stage 4 several small vortices arise and separate, causing various c_l oscillations. Among these, a second quite strong vortex causes second stall at stage 5 in fig. 6.14, with a consequent evident c_l peak. Afterwards, the maximum oscillation amplitude is achieved and AoA starts decreasing. At this point, marked as stage 6, the flow is fully separated and the lift coefficient repeatedly oscillates. At stage 7 the reattachment process begins, as clearly visible in fig. 6.15, evolving without any noteworthy characteristic until complete reattachment.

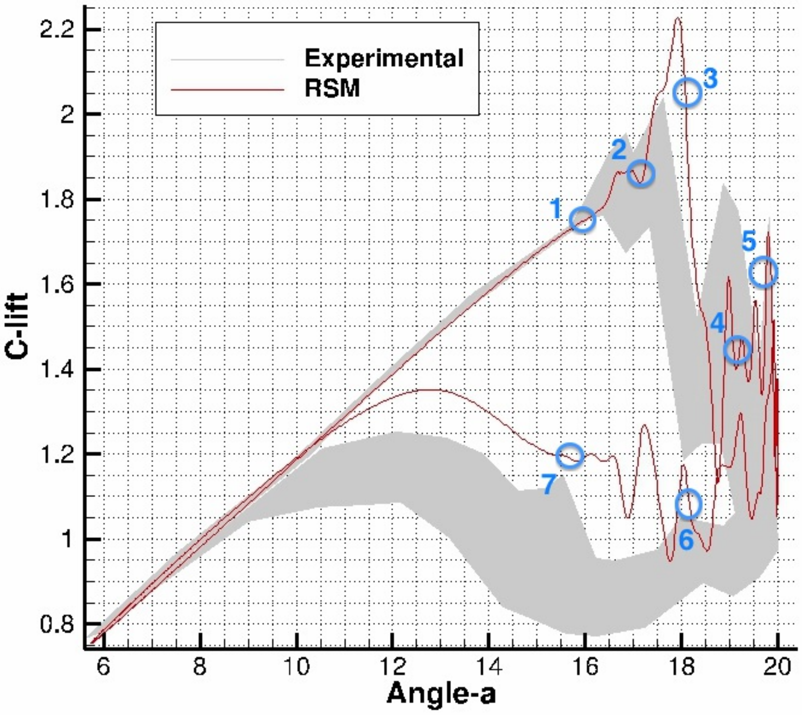

Figure 6.11: Different dynamic stall stages on lift coefficient curve

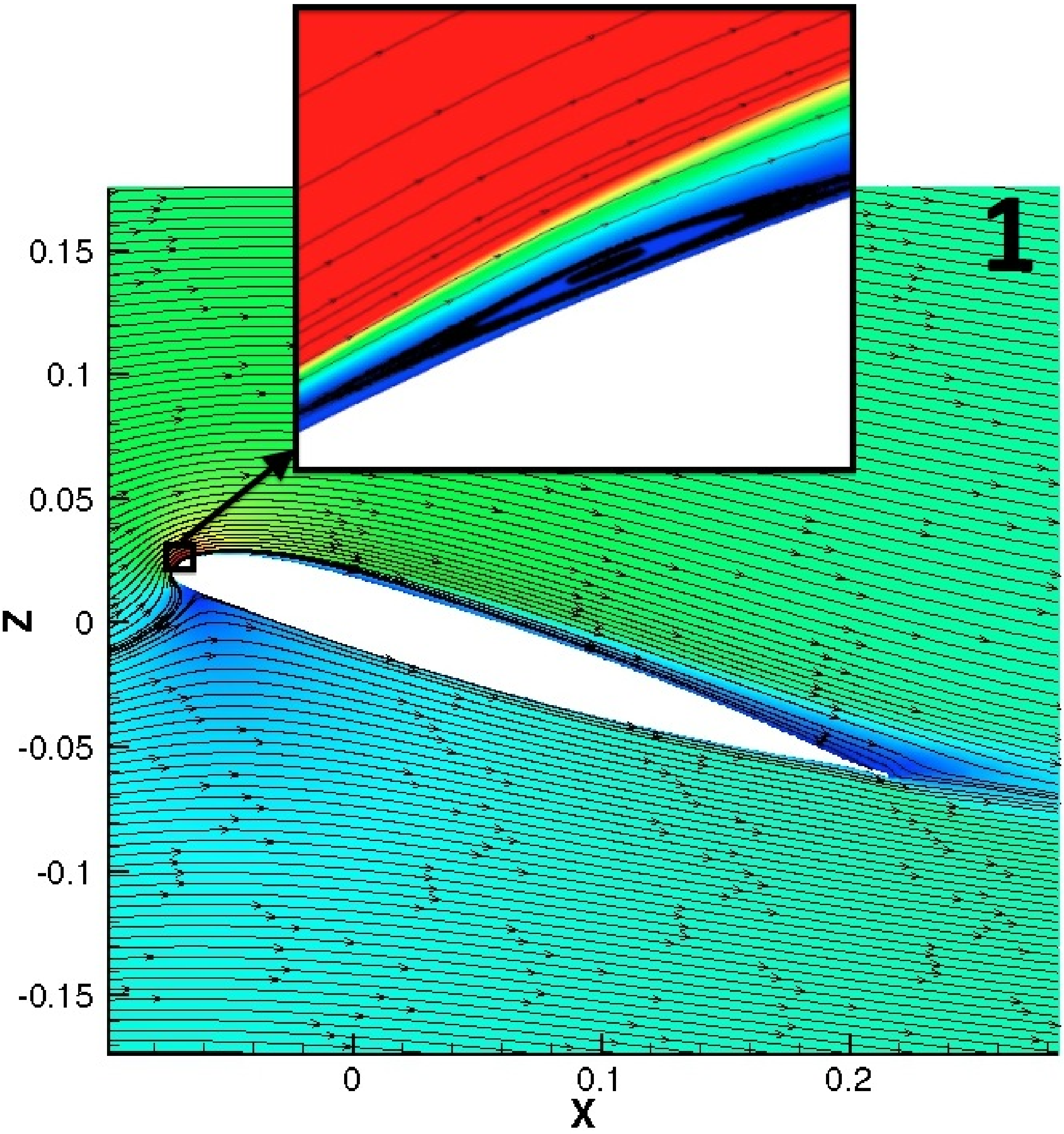

Figure 6.12: Flowfield during upstroke with a detail of the LEV formation

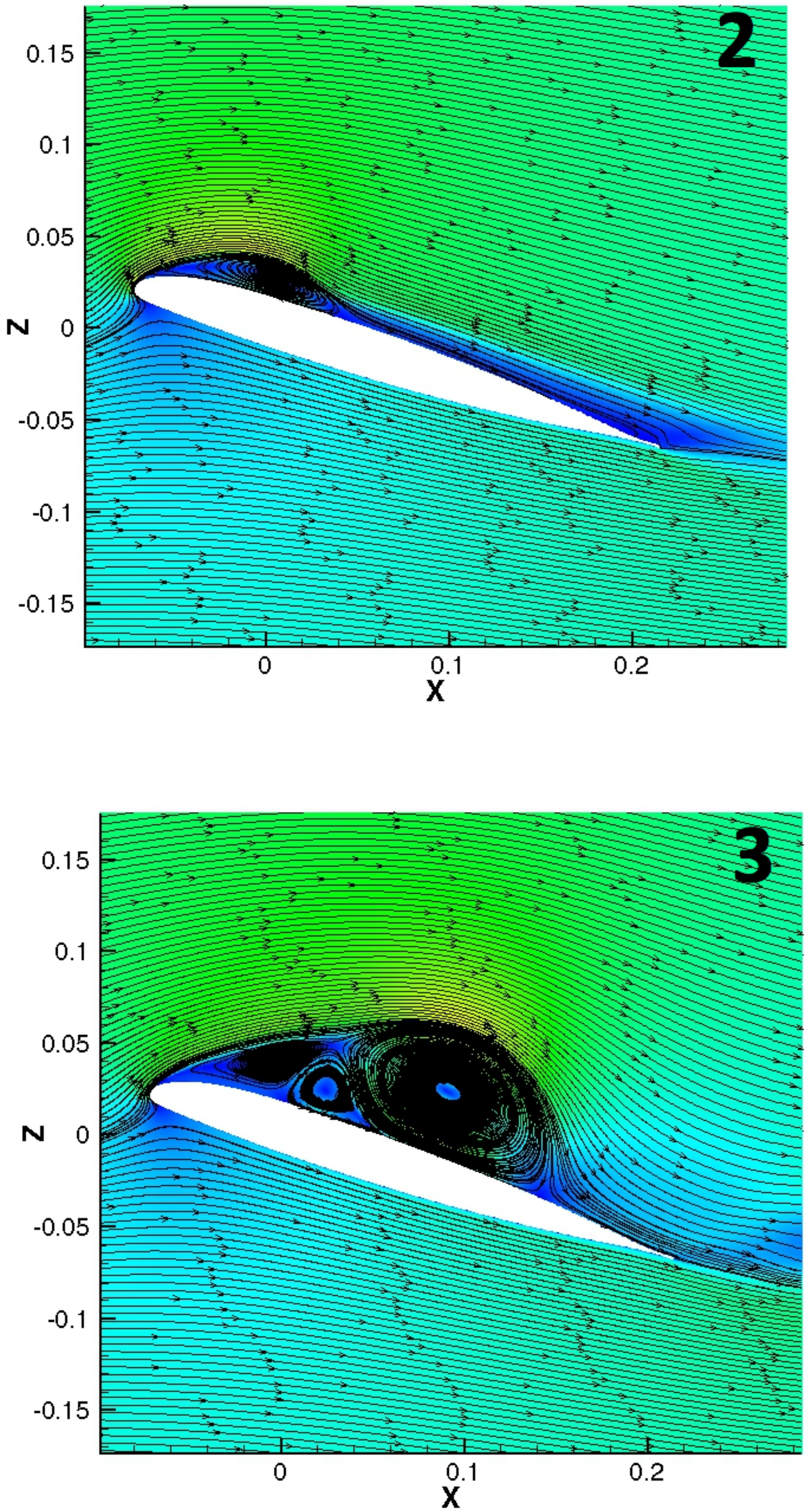

Figure 6.13: LEV growth and spread from leading edge towards trailing edge

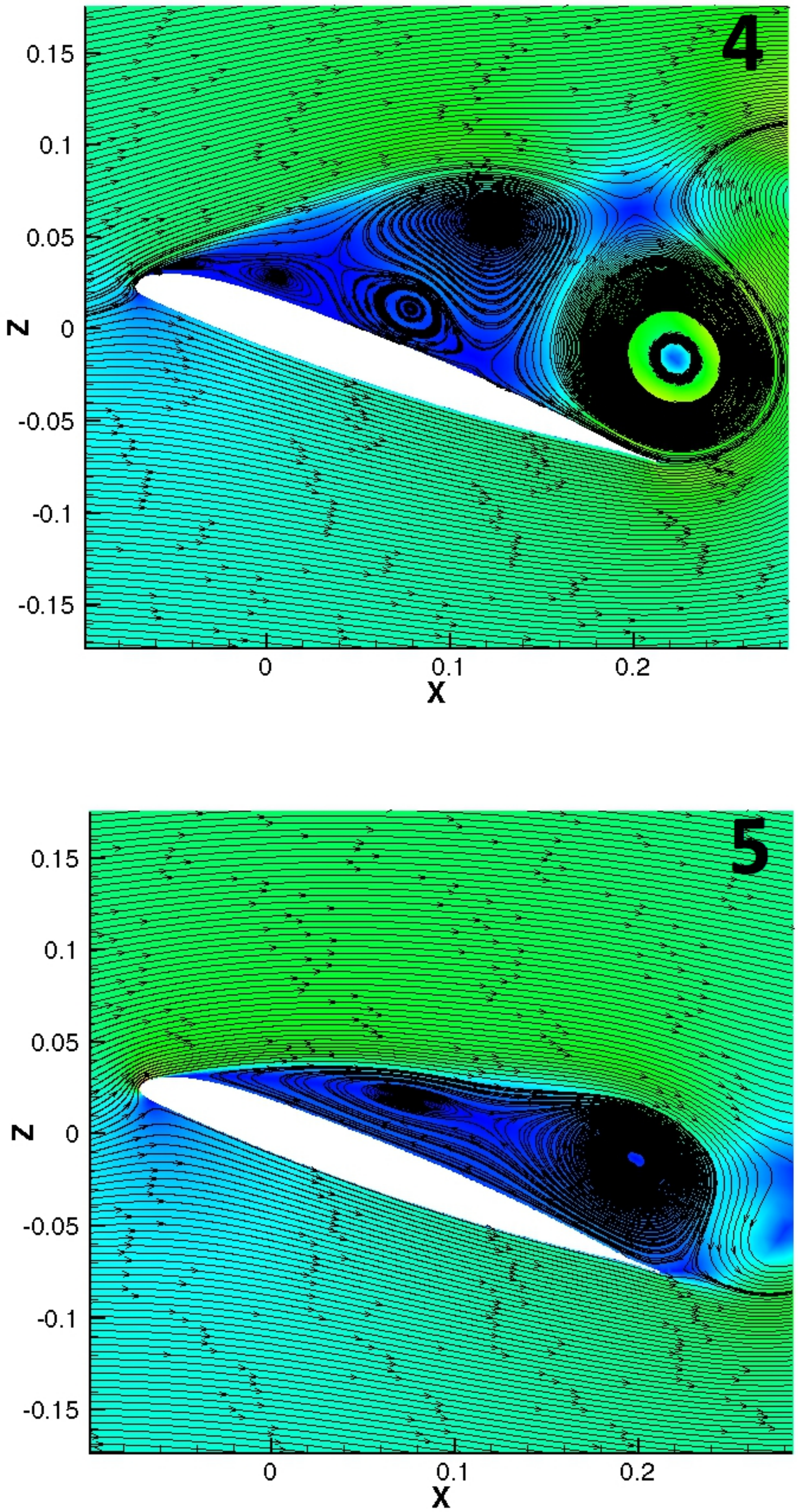

Figure 6.14: Flow evolution and second stall vortex generation

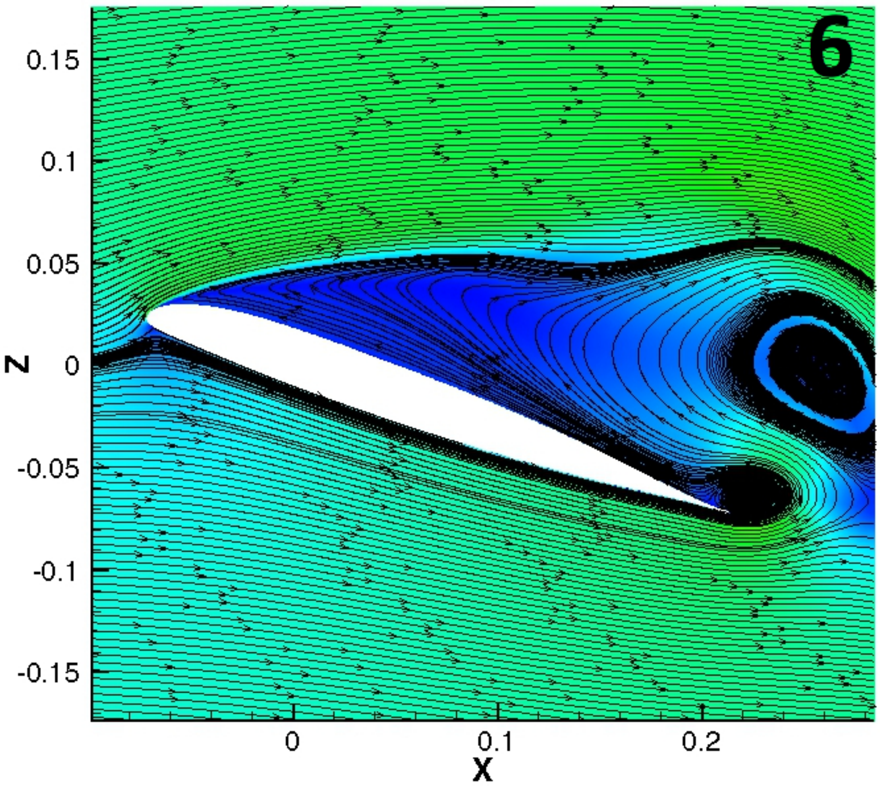

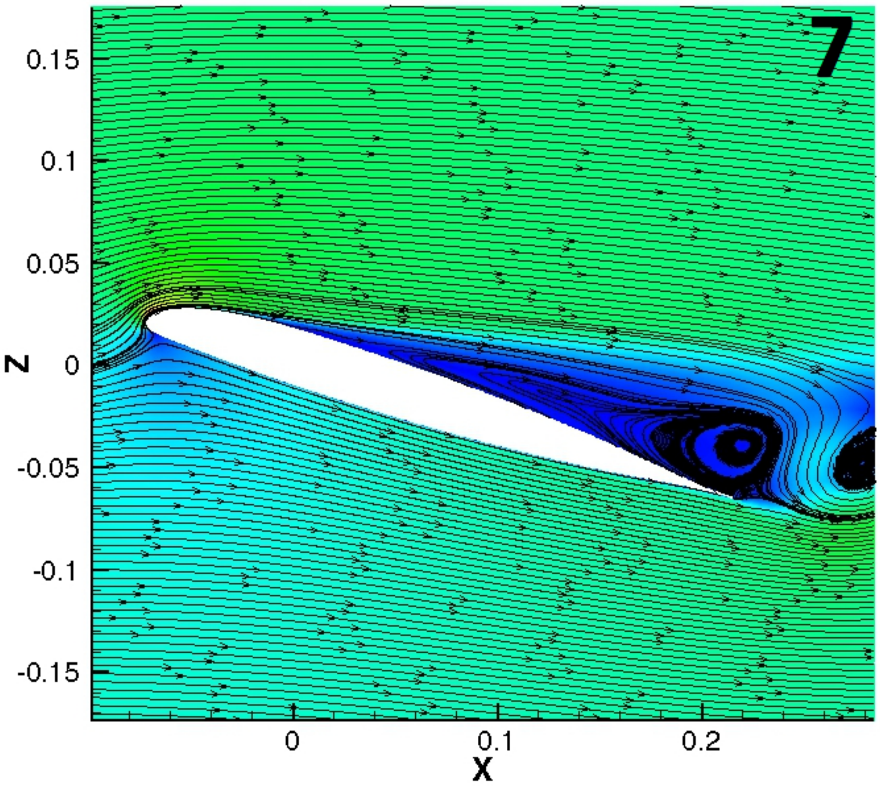

Figure 6.15: Fully separated flow and reattachment process

6.2.4 Computational cost

It has been already pointed out analyzing steady results that computational cost is of particular importance in CFD. This is even more true managing unsteady computations, where computing time can last really long. For practical purposes the only parameter which is worth to show is the computational time. The number of iterations results quite useless to make a comparison due to the excessive high values, while the convergence should be report at each timestep. However, residual behavior has been checked during each computation, ensuring always an excellent convergence. In tab. 6.3 a comparison among computational times of every model computed is presented. Values shown are in hours per computation, or rather the time necessary to perform three oscillating periods. The only direct comparison between turbulence models is possible with the *Coarse Mesh*, even though it should be noted that final results were not acceptable. Hower, it is evident the higher computational time required by RSM to get convergence, more than double compared to SAE. In general, SAE computations are appreciable for a quite fast convergence, especially regarding the grid *Fine1*. Conversely, as already mentioned, grid refinnement needed by RSM leads to long waiting time, especially in the case of *Fine3* grid. The *Fine4* may be considered a good compromise between improvement produced by RSM and acceptable computational time.

Table 6.3: Computational time comparison between SAE and RSM using different grids

COMPUTATIONAL TIME [h]		
GRID	SAE	RSM
Coarse Mesh	23	60
Fine1	30	-
Fine2	39	-
Fine3	-	290
Fine4	-	133

7 Transition Prediction

Accurate prediction of laminar to turbulent transition is important in many engineering situations, as the drag and heat transfer associated with a turbulent boundary layer is approximately double that of a laminar one. For this reason modern rotor blade airfoils are designed to have significant amount of laminar flow, decreasing drag compared to turbulent airfoils. Numerical and experimental investigations have shown that boundary layer transition can strongly affect the dynamic stall characteristics of rotor blade airfoils [68]. Hence, it is evident that the influence of transition from laminar to turbulent must be considered to achieve an accurate prediction of dynamic stall.

7.1 Transition in Dynamic Stall

Simulating fully turbulent flow has shown that quite good correspondences exist between experiment and calculation. Thanks to a close look into the very details of the numerical calculations, it was found that the development and extension from rear to front of the turbulent separation area plays the most important role in the dynamic stall onset process [68]. Without a leading edge separation bubble, the increasing amount of vorticity created at the airfoil leading edge is forced to spread out into the outer flow. Then, vorticity accumulates to a concentrated vortex which in the further course of the cycle starts to move downstream [68]. The displacement effect of the turbulent separation area is the main cause of dynamic stall onset. Nevertheless, when free transition is considered, local modifications of these events have been observed and special flow features occur at the leading edge during the higher AoA [13]. For stall initiated at the leading edge a quantitive agreement with experimental data is less favourable; EKATERINARIS et al. provided a good experimental and numerical evidence, showing that in this case the flow is sensitive to the state of the boundary layer (laminar, transitional or fully turbulent) immediately ahead the separation point, visible in fig. 7.1 [18]. In particular, a leading edge separation bubble develops and transition from laminar to turbulent takes place along this bubble: in fig. 7.2 the three fundamental points S (laminar separation), T (transition) and R (turbulent reattachement) are marked. The bubble is then fluctuating during upstroke and produces local clockwise and anticlockwise additional vorticity which is mixing with the main stream of vorticity. This mixing process keeps the vorticity layer closer to the airfoil surface and delays dynamic stall onset [68].

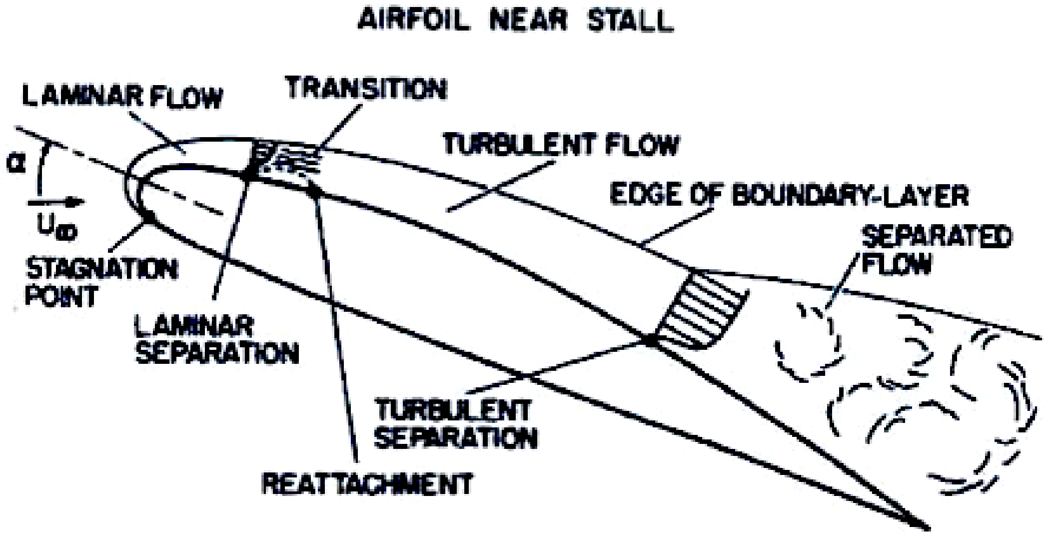

Figure 7.1: Schematic view of the flow transition in the boundary layer when airfoil is near stall [44]

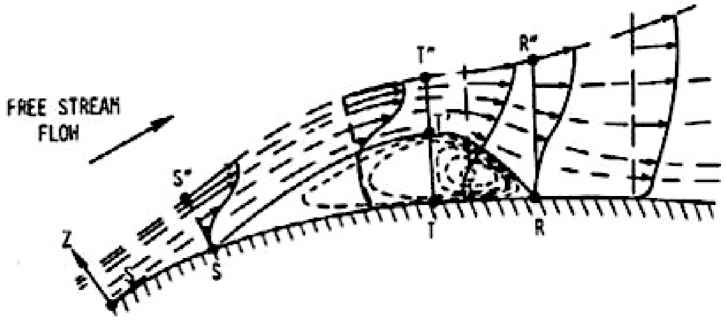

Figure 7.2: Visualization of a leading edge separation bubble within the boundary layer, with flow streamlines and velocity distribution [44]

A comprehensive study adding transition module in the TAU parameter file has been carried out by DLR, using different turbulence models [58]. Simulations were conducted adopting a laminar boundary layer code with an e^N database method for Tollmien-Schlichting instabilities, relevant for bidimensional pitching airfoil. Results have shown that during upstroke the influence of boundary layer transition on prediction is small. Lift is altered only marginally and transition location moves slightly with increasing AoA, leading to nearly fully turbulent flow on the airfoil upper side at AoA higher than $\alpha \approx 9°$. The only really noticeable difference is visible during downstroke, when reattachment is shifted to lower AoA. In this work a further step in transition modelling is done with the employment of the γ-Re_θ transition model, on which this chapter focuses.

7.2 The γ-Re_θ Transition Model

Altough transitional boundary layer flows are important un many CFD applications, modern unstructured, parallel CFD codes do not lend themselves to traditional correlation-based methods for transition prediction. These methods are based on non-local variables such as momentum thickness or boundary layer edge location, which can be expensive, impractical, or even practically impossible to evaluate [40]. Inclusion of transition within simulations based upon solution of the RANS equations is still a challenging task. Transition physics, mathematical tools for boundary layer stability analysis and progress made in transition prediction were reviewed by MALIK, who identified four instability modes: Tollmien-Schlichting, Gortler, cross-flow and Mack [41]. The relative importance of the individual instability modes for pitching airfoils and wings is poorly understood yet. For pitching two-dimensional airfoils only the Tollmien-Schlichting instability is relevant and can be solved using the γ-Re_θ transition model.
The γ-Re_θ transition model, introduced by MENTER et al. [51], presented for the first time a correlation-based approach to transition modeling that was specifically designed for modern CFD codes. Unfortunately, the model has not gained wide acceptance in the CFD community because two critical correlations ($Re_{\theta c}$ and F_{length}) were deemed proprietary and have remained unpublished by the original authors, even as their model has been refined in subsequent publications [35][36]. These functions have been empirically derived by many authors. Briefly, the γ-Re_θ transition transport model combines a modified Menter-SST k-ω turbulence model with two additional transport equations for transition prediction, one for the intermittency γ and one for the Reynolds number based on momentum thickness at the transition point $Re_{\theta t}$. The intermittency represents the fraction of time the flow is turbulent at a fixed position in the flow field. It is zero in case of laminar flow and one in case of turbulent flow. In the transition region γ varies in between zero and one [16]. The transport equation for $Re_{\theta t}$ is controlled by an empirical transition criterion, which is only valid outside of the boundary layer. Inside the boundary layer, the information about transition onset is transported by convection and diffusion terms. The complete theoretical formulation and the relevant literature may be found in the TAU technical documentation [16]. As aforamentioned, the main advantage is that the model is based on local variables, which allows for transition prediction within a RANS solver. The basic Reynolds-number ratio correlates local quantities to non-local boundary layers quantities, enabling transition prediction without special efforts like integration along lines or special search-algorithms [15]. Concerning the two empirical functions $Re_{\theta c}$ and F_{length}, many approaches are implemented in TAU: by Menter-Langtry (default), Suluksna, Pettersson, Misaka and Krause.
The application of the γ-Re_θ model requires a suitable resolution of the flow field. For the grid wall resolution, $y^+ < 1$ is highly recommended, since the wall normal resolution of the boundary layer needs to be high enough to solve the velocity gradient properly [15]. Thus, the *Fine4* grid previously created for the use of RSM is adopted, according to this condition. Furthermore, it is necessary to define two general parameters for this model: the initial/farfield turbulence intensity (Tu_{ff}) and the initial/farfield ratio of turbulent to molecular viscosity (μ_t/μ). As explicitly reported in the TAU user guide, "using the default values for the γ-Re_θ

model will lead to wrong transition locations" [15]. The turbulence intensity assumes a key role and needs to be adjusted so that near the airfoil the exact value from wind tunnel experiment is achieved. These two parameters must be correctly calibrated, with the main purpose to take into account the decay of turbulence intensity in the farfield due to the characteristics of the two-equation turbulence model. By defining the turbulence intensity at the farfield boundary and the ratio μ_t/μ, the turbulence intensity near the airfoil (Tu) may be obtained from the following equation:

$$Tu = (Tu_{ff}^2(1+\frac{3}{2}Tu_{ff}^2U_\infty\rho x\beta\frac{1}{\mu\frac{\mu_t}{\mu}})^{-\frac{\beta^*}{\beta}})^{\frac{1}{2}} \tag{7.1}$$

where U_∞ is the freestream velocity, β^* and β are constants from the turbulence model and x is the distance from the farfield boundary to the airfoil. Through the variation of the ratio μ_t/μ the decay of turbulence intensity is influenced.
For this problem, it was found that reliable result are obtained using the following values:

General turbulent intensity (Tu_{ff}): 0.000717

General ratio mue-t/mue-l (μ_t/μ): 5.0

Moreover, it should be remembered that, similar to the application of the two-equation turbulence models and RSM, it is reccomended to switch off the multigrid scheme for the turbulence/transition equations and the eigenvalue correction [15].

7.3 Results

A restart has been performed from the solution with RSM at the end of the second cycle, in order to compute only the third oscillating period and reduce the running time. Moreover, this strategy allows starting already from a good solution, with a consequent fast convergence without affecting the results obtained with the four-equation model. To also ensure a better temporal resolution, the number of physical timesteps has been increased to n_t = 1800, resulting in a computational time anyway lower than the previous model. Airloads prediction is shown in fig. 7.3. In both pictures is visible a slight delay of the whole phenomenon: fist and second stall occur at higher AoA, while complete reattachment takes place at lower AoA. During upstroke results are very similar to RSM model. The only noticeable difference is a small decrease of the c_l peak and an increase of the c_m in correspondence to the first stall event. Moreover, the real improvement in the solution may be observed after the main stall, where the number of oscillations and peaks clearly decreases and instability in prediction is reduced. Also during the reattachment process, it is apparent that the γ-Re_θ model shows a quicker stabilization in the airloads trend, especially in fig. 7.3a. Furthermore, computed values of the lift coefficient are significantly closer to experimental data compared to RSM prediction.

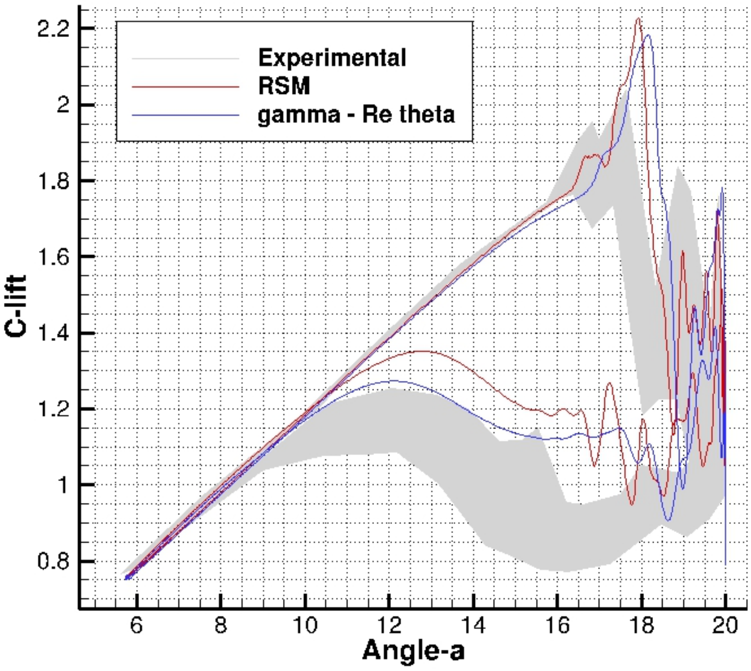

(a) Lift coefficient versus AoA

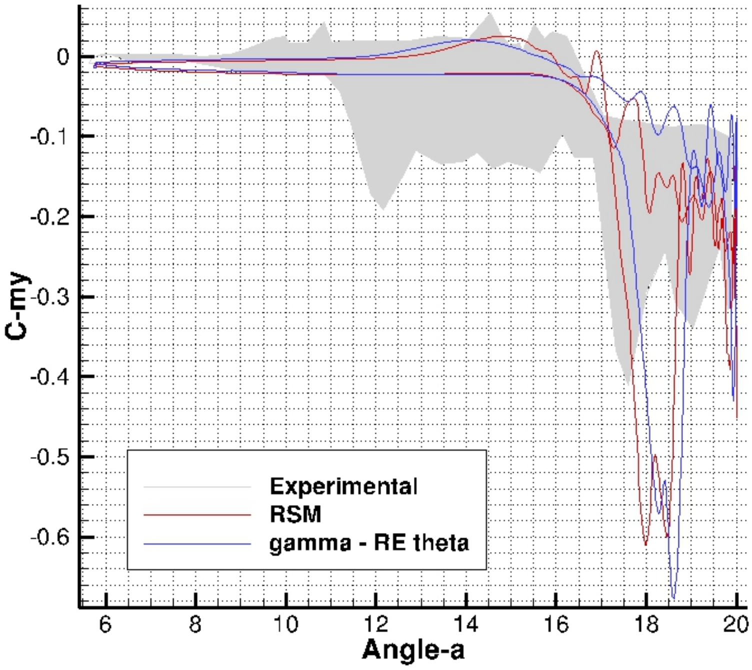

(b) Pitching moment coefficient versus drag coefficient

Figure 7.3: Lift and pitching moment coefficients prediction with γ-Re_θ transition model

7.3.1 The Skin Friction

As previously explained, the main purpose of adopting a transition model, like the γ-Re_θ, is the related possibility to have a description of the boundary layer transition, and especially in which point over the airfoil this transition takes place. A valid coefficient which can show this flow feature is the skin friction coefficient (c_f). In the following, skin friction and its coefficient are briefly defined, and then used to show transition evolution during dynamic stall.
Skin friction is caused from the interaction between the fluid and the skin of the body, and is directly related to the wetted surface, that is the surface area of the body in direct contact with the fluid. Skin friction is a component of the parasitic drag, which includes also the form drag and the interference drag [33]. Like the other components of parasitic drag, skin friction follows the drag equation and rises with the square of the velocity. The skin friction coefficient (c_f) is defined by:

$$c_f = \frac{\tau_\omega}{\frac{1}{2}\rho U_\infty^2} \tag{7.2}$$

where τ_ω is the local wall shear stress, ρ the fluid density and U_∞ the freestream velocity. As suggested by eq. (7.2), skin friction is caused by viscous drag in the boundary layer around the object. The boundary layer at the front of the object is usually laminar and relatively thin, but becomes turbulent and thicker towards the rear. As already stated at the beginning of this chapter, turbulent boundary layer leads to a higher drag compared to laminar boundary layer [36]. Thus, it is evident that the transition point over the surface may be easily located watching the skin friction coefficient behavior. In fact, the drag increase due to the flow transition from laminar to turbulent yields a further increase of drag and consequently an instant growth of c_f. In particular for an airfoil at a positive AoA, like the problem studied in this thesis, the above-mentioned behavior is observed on the suction side near the leading edge, where the leading edge separation bubble is noticed, and on the pressure side near the trailing edge.
In fig. 7.4 and 7.5, the skin friction coefficient behavior over both side of the airfoil is plotted at different AoA. In detail, the two c_f peak due to transition are clearly visible. It is also noticed that transition points change with the AoA, moving forward during upstroke and backward during downstroke. In fig. 7.6, the variations of transition positions are shown, presented as transition location normalized by the chord versus instant time normalized by the oscillation period. It is immediately noticed that the first value over the suction side is wrong predicted, since transition positions at the beginning and at the end of the period should be the same. Moreover, this odd value, probably caused by the restart from a previous solution computed with a different model, clashes with the curve trend. For these reasons it may be ignored. As visible, major changes affect the suction side, where transition moves between x/c $\approx$ 2% and x/c $\approx$ 18%. Conversely, on the pressure side changes are very small, with transition moving between x/c $\approx$ 90% and x/c $\approx$ 96%. It should be remarked that values reported in fig. 7.6 have been graphically acquired by the skin friction coefficient plot, therefore they are affected by a certain margin of error. Nevertheless, this is acceptable, since the purpose of this section is not the prediction of the exact transition position but the showing of its moving trend.

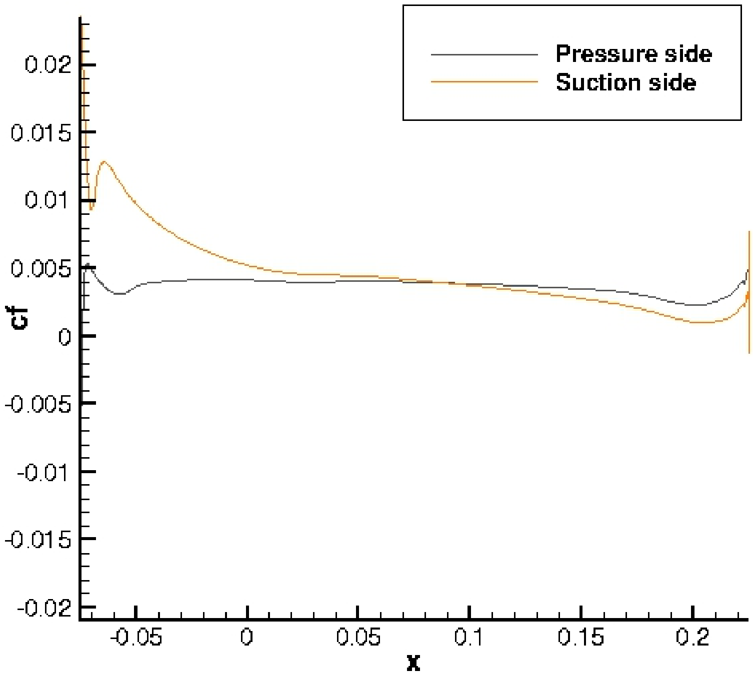

(a) Skin friction coefficient at $\alpha = 2.0°$

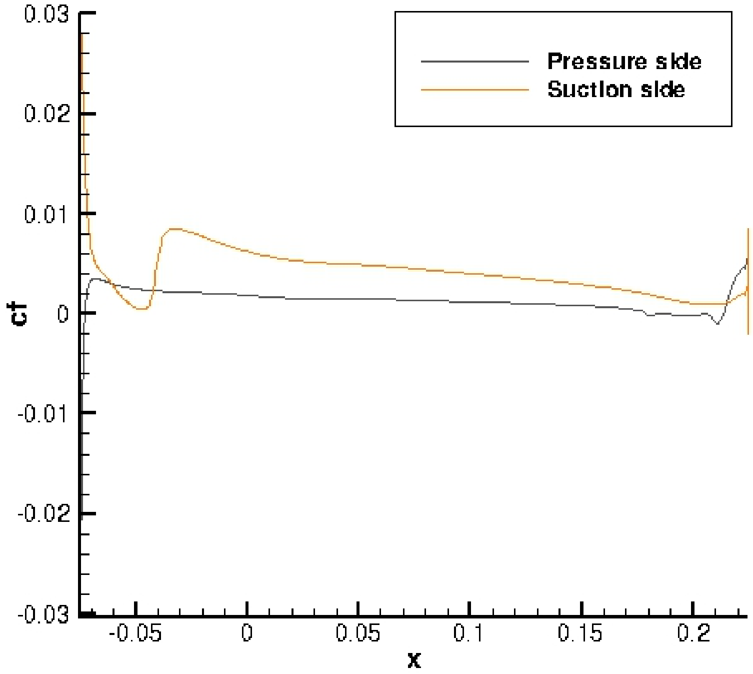

(b) Skin friction coefficient at $\alpha = 9.92°$

Figure 7.4: Skin friction coefficient plot versus position during upstroke

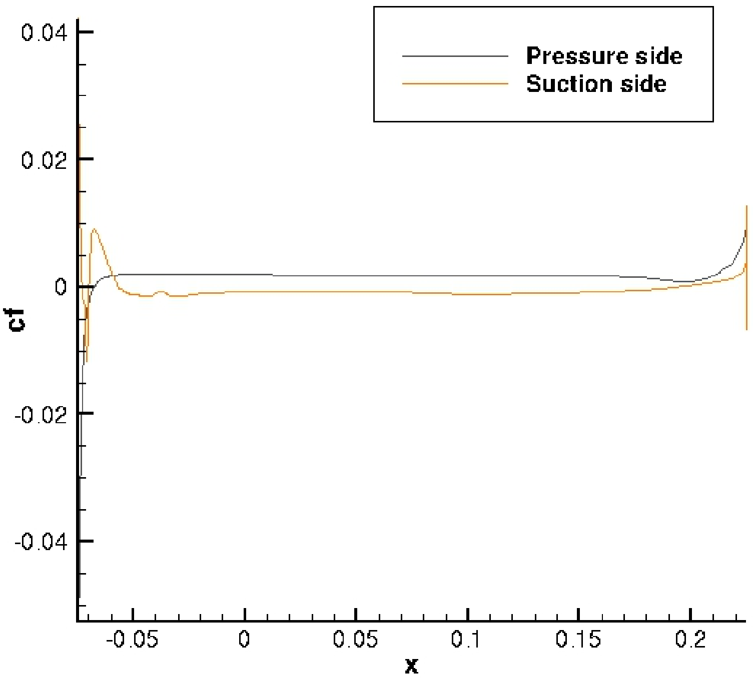

(a) Skin friction coefficient at α = 18.82°

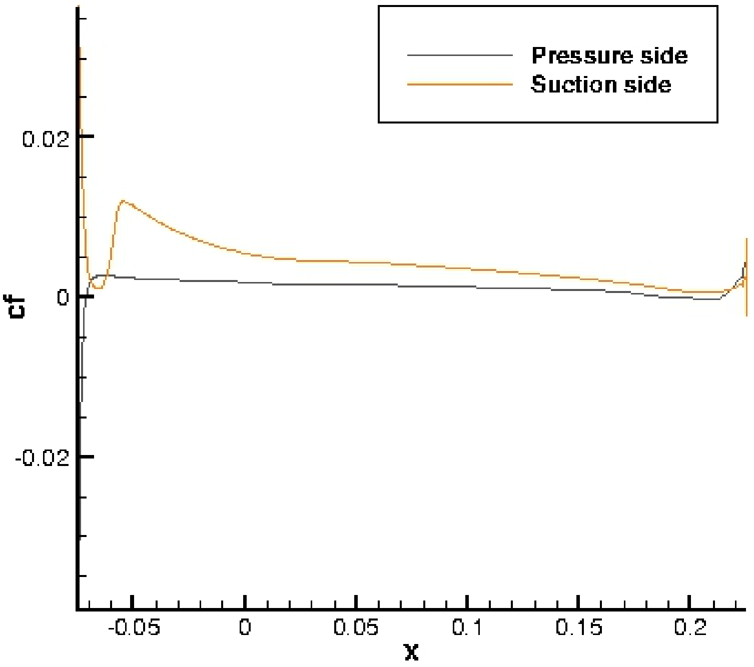

(b) Skin friction coefficient at α = 5.74 °

Figure 7.5: Skin friction coefficient plot versus position during downstroke

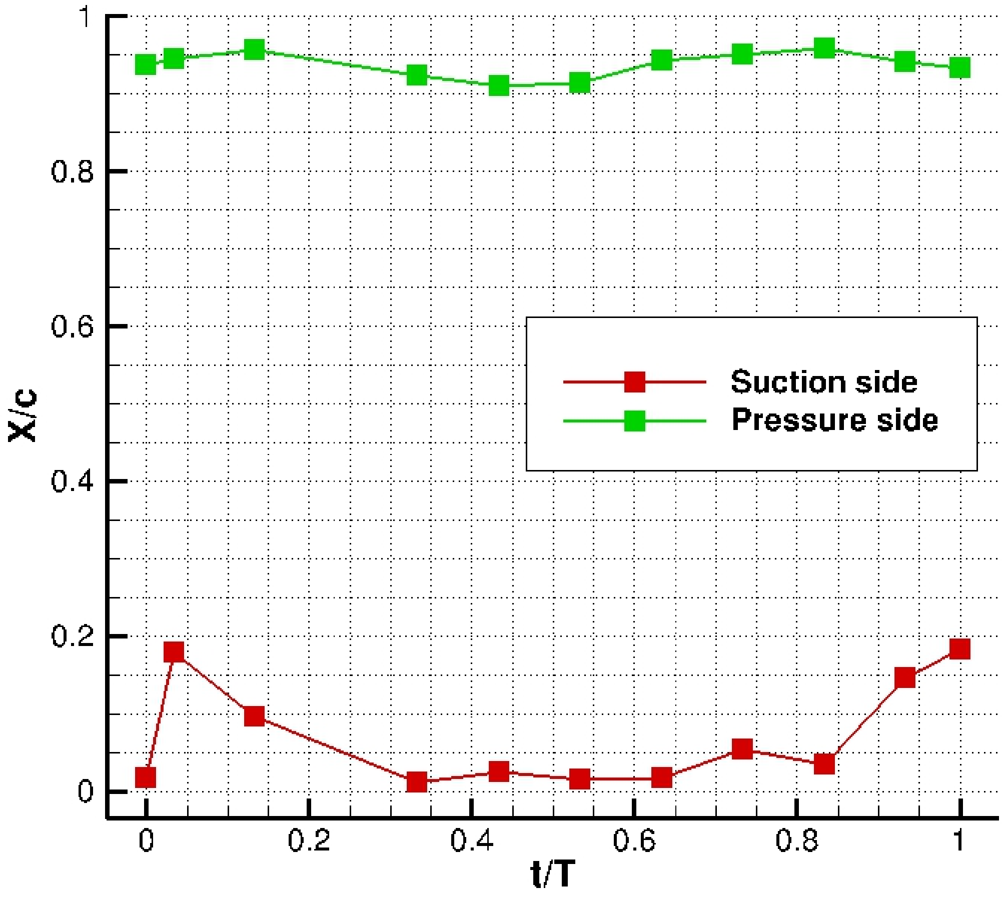

Figure 7.6: Location changes of the transition points on suction and pressure side

8 Summary and Conclusions

In this chapter results obtained in this thesis are summarized, and further considerations are reported.

8.1 Static CFD Analysis

The model of the airfoil OA209 has been validated for the static analysis using the DLR TAU computational fluid dynamics solver. Grid generation using the automatic grid generation tool of ANSYS ICEM-CFD software has shown some difficulties in spatial discretization, especially for the region near the trailing edge. Several grids have been computed through a grid resolution study, reaching a good grid independency with the grid called *Fine1*. Concerning the solver settings, the most stable and efficient solver configuration under steady conditions has proved to be the implicit backward Euler iterative scheme, associated with the central scheme for the convective flux discretization and the second-order Roe upwind scheme for the convective fluxes of the turbulence equations.

Computational results exhibit a difference in the prediction of the lift curve compared to experimental data, due to several wall effects in airfoil experiments. For this reason the linear region is not well captured by models used, which do not consider three-dimensional effects. Nevertheless, the maximum lift coefficient value has been correctly described by every model. In particular, the one-equation Spalart-Allmaras turbulence model shows a higher stability during computations, with an exact prediction of the airload coefficients trend. The more complex Reynolds Stress Model proves to be difficult to use in the practice, leading to the best results but only after several further modifications of grid and solver parameters.

8.2 Dynamic Stall Predictions

Good results have been achieved in this work regarding dynamic stall prediction. First of all, temporal resolution studies are performed in order to find the best temporal discretization to analysis this phenomenon. In particular, influence of the number of physical timestep has been investigated. Considering results obtained, previous static validation has proved to lead to excellent results in association with the Spalart-Allmaras model. It is remarkable that the best prediction in first stall event is achieved with this model. Both position and magnitude of the lift coefficient peak related to first stall are correctly described, and even more well-captured is the behavior of the pitching moment coefficient, which perfectly matches the experimental data. Conversely, a general under-prediction of the second stall event is visible in both airloads.

Concerning prediction with RSM, obtaining good results with this complex turbulence model has proved to be a difficult task. Validation under steady conditions is brought into question, and further modifications of grid and solver parameters have revealed to be necessary. Different strategies have been investigated, and at the end the increase of structured layers height has yielded good results. Airloads prediction with RSM shows a general over-prediction of the first stall event, especially regarding the pitching moment coefficient, while the second stall is very well-captured. A significant improvement compared to Spalart-Allmaras model is observed. However, it may be stated that computational cost considerably increases with the use of RSM.

8.3 Transition Prediction

The use of the γ-Re_θ transition model allows to have an outlook in considering also boundary layer transition from laminar to turbulent, whose importance for an accurate prediction has been highlighted. New results show a slight delay of the whole phenomenon and an equally slight better first stall prediction. Real improvements are observed in terms of stability in flow description after first stall event and during reattachment, with less oscillations in both lift and pitching moment coefficient predictions. Furthermore, location of transition point has been investigated through the study of the skin friction coefficient trend over both side of the airfoil. A tendency to move is evident, with transition point moving forward during upstroke and backward during downstroke.

8.4 Future Works

During this work, good results have been achieved in two-dimensional dynamic stall prediction. Nevertheless, it is obvious that dynamic stall during helicopter flight has more complex characteristics, as described at the beginning of this thesis. Future works can start from considerations here done in order to model the entire helicopter rotor, where also rotational and three-dimensional effects must be considered.

Furthermore, it is evident that an accurate knowledge of dynamic stall evolution allows the adoption of several expedients to improve blade performance. In particular, numerous passive and active dynamic stall control devices have been developed and investigated in order to gain the following achievements:

- Reduce the negative pitching moment peak
- Maintain or reduce the drag
- Maintain or increase the lift

Different strategies make use of droop nose [22], model deformation [12], leading edge slat [9], periodic excitation [25] or plasma actuators [54]. Moreover, GEISSLER et al. developed a very simple, retro-fit capable passive device, named Leading Edge Vortex Generator (LEVOG), that significantly improves the aerodynamic performance of a wing under dynamic stall conditions, with minor influence on the rest of the cycle [23]. Thus, it is evident that the configuration of the clean wing may experiences several changes, but the work carried out in this thesis represents an appreciable help in the prediction of these control devices effects.

Bibliography

[1] Retreating blade stall, http://www.dynamicflight.com.

[2] BEDDOES, T. S. A synthesis of unsteady aerodynamic effects stall hysteresis. *J. Vertica*, 1 (1976), 113–123.

[3] BEDDOES, T. S. Onset of leading edge separation effects under dynamic conditions and low mach number. *34th Annual Forum of the American Helicopter Soc.* (May 1978).

[4] BENEK, J. A., BUNING, P. G., AND STEGER, J. L. A 3-d chimera grid embedding technique. *AIAA 85*, 1523 (1985).

[5] BLAZEK, J. *Computational Fluid Dynamics: Principles and Application*, second edition ed. Elsevier, 2005.

[6] BOUSMAN, W. G. A qualitative examination of dynamic stall from flight test data. *Journal of the American Helicopter Soc. 43*, 4 (1998), 279–295.

[7] BOUSMAN, W. G. Airfoil dynamic stall and rotorcraft maneuvrability. Tech. rep., Army/NASA Rotorcraft Division,Army Aviation and Missile Command, Aeroflightdynamics Directorate (AMRDEC), Ames Research Center,, July 2000.

[8] BRANDT, A. Guide to multigrid development. multigrid methods i, 1981.

[9] CARR, L., AND MCALISTER, K. W. The effect of a leading-edge slat on the dynamic stall of an oscillating airfoil. *AIAA*, 1983-2533 (1983).

[10] CARTA, F. O. An analysis of the stall flutter instability of helicopter rotor blades. *Journal of the American Helicopter Soc. 12*, 4 (1967), 1–18.

[11] CARTA, F. O. Effect of unsteady pressure gradient reduction on dynamic stall delay. *J. of Aircraft 8*, 10 (1971), 839–840.

[12] CHANDRASEKHARA, M., WILDER, M., AND CARR, L. Unsteady stall control using dynamically deforming airfoils. *AIAA j. 36*, 10 (1998), 1792–1800.

[13] Cranfield University and Sheffield University. *Investigation of transition modelling for airfoil dynamic stall.*

[14] Davenport, F. J., and Front, J. V. Airfoil sections for rotor blades-a reconsideration. *America Helicopter Society 34th Annual National Forum* (May 1966).

[15] DLR. *TAU-Code User Guide*, release 2012.1.0 ed., 26 March 2012.

[16] DLR. Technical documentation of the dlr tau-code release 2012.1.0. Tech. rep., Institute of Aerodynamics and Flow Technology (Braunschweig), 2012.

[17] Edwards, J. R., and Chandra, S. Comparison of eddy viscosity-transport turbulence models for three-dimensional, schock-separated flowfields. *AIAA j. 34*, 4 (April 1996).

[18] Ekaterinaris, J. A., Srinivasan, G. R., and McCroskey, W. J. Present capabilities of prediciton two-dimensional dynamic stall. *AGARD CP* (1994).

[19] Ericsson, L. E. Comments on unsteady airfoil stall. *J. of Aircraft 4*, 5 (1967), 478–480.

[20] Ericsson, L. E., and Reding, J. P. Dynamic stall of helicopter blades. *Journal of the American Helicopter Soc. 17*, 1 (1972), 10–19.

[21] Ericsson, L. E., and Reding, J. P. Stall-flutter analysis. *J. of Aircraft 10*, 1 (January 1973).

[22] Geissler, W. Dynamic stall control by airfoil deformation. *19th European Rotorcraft Forum 9*, 1 (1993).

[23] Geissler, W., Dietz, G., Mai, H., Bosbach, J., and Richard, H. Dynamic stall and its passive control investigation on the oa209 airfoil section. Tech. rep., DLR-Göttingen.

[24] Green, R. B., and Galbraith, R. A. Dynamic recovery to fully attached airfoil flow from deep stall. *AIAA j. 33*, 8 (1995), 1433–1440.

[25] Greenblatt, D., and Wygnanski, I. Dynamic stall control by periodic excitation, part1: Naca 0015 parametric studies. *J. of Aircraft 38*, 3 (2001), 430–438.

[26] Isaacs, N. C. G., and Harrison, R. J. Identification of retreating blade stall mechanisms using flight test pressure measurements. In *45th Annual Forum of the American Helicopter Soc.* (Boston, MA, May 22-24 1989), American Helicopter Soc.

[27] JAMESON, A. Solution of the euler equations by a multigrid method. *Applied Mathematics and Computation 13* (1983), 327–356.

[28] JOHNSON, W., AND HAM, N. D. On the mechanism of dynamic stall. *Journal of the American Helicopter Soc. 17*, 4 (1972), 36–45.

[29] KAO, H. J., LIOU, M. S., AND CHOW, C. Y. Grid adaption using chimera composite overlapping meshes. *AIAA j. 32*, 942-949 (1994).

[30] KOREN, B. Multigrid and defect correction for the steady navier-stokes equations. *J. Computational Physics 87* (1990), 25–46.

[31] KRAMER, M. Increase in the maximum lift of an airfoil due to a sudden increase in its effective angle of attack resulting from a gust, 1932.

[32] KRISHNAN, V. *Advancing Detached Eddy Simulations*. PhD thesis, Arizona State University, August 2008.

[33] KUNDU, A. K. *Aircraft design*. Cambridge University Press, 2010.

[34] LAKSHMINARAYANA, B. Turbulence modeling for complex shear flows. *AIAA j. 14*, 12 (1986), 1900–1917.

[35] LANGTRY, R. B. *A Correlation-based Transition Model Using Local Variables for Unstructured Parallelized CFD codes*. PhD thesis, Institute of Thermal Turbomachinery and Machinery Laboratory, University of Stuttgart, 2006.

[36] LANGTRY, R. B., AND MENTER, F. R. Transition modeling for general cfd applications in aeronautics. *AIAA*, 522 (2005).

[37] LAUNDER, B. E. Second-moment closure: Present... and future? *Inter. J. Heat Fluid Flow 10*, 4 (1989), 282–300.

[38] LAUNDER, B. E., REECE, G. J., AND RODI, W. Progress in the development of a reynolds-stress turbulence closure. *J. Fluid Mechanics 68*, 3 (April 1975), 537–566.

[39] LEISHMAN, J. G. *Principles of Helicopter Aerodynamics*. Cambridge University Press, 2002.

[40] MALAN, P., SULUKSNA, K., AND JUNTASARO, E. Calibrating the γ-reθ transition model for commercial cfd. *47th AIAA Aerospace Science Meeting* (January 2009).

[41] MALIK, M. R. Boundary-layer transition prediction toolkit. *AIAA* (1997), 1904.

[42] MANRONGIU, C. Dynamic stall. CIRA.

[43] MARTINELLI, L. *Calculation of Viscous Flows with a Multigrid Method.* PhD thesis, Princeton University, 1987.

[44] MARY, I., GLEIZE, V., AND LAURENT, C. Qdns of a flow around a oa209 blade profile at stall incidence, December 2011.

[45] MCALISTER, K. W., AND CARR, L. W. Water tunnel visualization of dynamic stall. *J. of Fluids Engineering 101* (Sept. 1979), 376–380.

[46] MCCROSKEY, W. J. Inviscid flowfield of an unsteady airfoil. *AIAA j. 11*, 8 (1973), 1130–1136.

[47] MCCROSKEY, W. J. Some current research in unsteady fluid dynamics. *J. of Fluids Engineering ASME*, 99 (1975), 8–38.

[48] MCCROSKEY, W. J., CARR, L. W., AND MCALISTER, K. W. Dynamic stall experiments on oscillating airfoils. *AIAA j. 14*, 1 (1976), 57–63.

[49] MCCROSKEY, W. J., MCALISTER, K. W., CARR, L. W., PUCCI, S. K., LAMBERT, O., AND INDERGAND, R. F. Dynamic stall on advanced airfoil sections. In *36th Annual Forum of the American Helicopter Soc.* (May 13-15 1980), American Helicopter Soc.

[50] MCHUGH, F. J., CLARK, R., AND SOLOMAN, M. Wind tunnel investigation of rotor lift and propulsive force at high speeds-data analysis. Tech. Rep. CR 145217-1, NASA, October 1977.

[51] MENTER, F. R., LIKKI, R. B., SUZEN, S. R., HUANG, Y. B., AND VÖLKER, S. A correlation-based transition model using local variables part 1 - model formulation. In *Proceedings of the ASME Turbo Expo, Power for Land Sea and Air* (June 2004), vol. ASME GT2004-53452.

[52] MERKLE, C. L., AND ATHAVALE, M. M. Time-accurate unsteady incompressible flow algorithms based on arificial compressibility". *AIAA* (1987), 87–1137.

[53] P. BOWLES, T. C., AND MATLIS, E. Stall detection on a leading-edge plasma actuated pitching airfoil utilizing onboard measurement. Center for Flow Physics and Control (FlowPAC), University of Notre Dame, 47th AIAA Aerospace Sciences Meeting and Exhibit.

[54] POST, M., AND CORKE, T. Separation control using plsama actuators: Dynamic stall vortex control on oscillating airfoil. *AIAA j. 44*, 12 (2004), 3125–3135.

[55] R. A. GALBRAITH, A. J. N., AND SETO, L. Y. On the duration of low speed dynamic stall.

[56] R. M. SCRUGGS, J. F. N., AND SINGLETON, R. E. Analysis of flow reversal delay for a pitching foil. *AIAA 12th AIAA Aerospace Sciences Meeting* (1974), 74–128.

[57] RICHTER, K. Dynamic stall suppression. In *69th US/German MoU on Helicopter Aeromechanics* (September 2012), no. DLR AS-HE.

[58] RICHTER, K., PAPE, A. L., KNOPP, T., COSTES, M., GLEIZE, V., AND GARDNER, A. D. Improved two-dimensional dynamic stall prediction with structured and hybrid numerical methods. *Journal of the American Helicopter Soc. 56*, 042007 (2011).

[59] RIZZI, A. The engineering of multiblock/multigrid software for navier stokes flows on structued meshes. *Computers and Fluids 22* (1993), 341–367.

[60] ROSSOW, C. C. Efficient computation of inviscid flow fields around complex configurations using a multiblock multigrid methods. *Appl. Numerical Methods 8* (1992), 735–747.

[61] SCHWAMBORN, D., GERHOLD, T., AND HEINRICH, R. The dlr tau-code: Recent applications in research and industry. In *European Conference on Computational Fluid Dynamics* (The Netherlands, 2006).

[62] SHUEN, J. S., CHEN, K. H., AND CHOI, Y. H. A coupled implicit method for chemical non-equilibrium flows at all speeds. *Journal of Computational Physics 106* (1993), 306–318.

[63] SHUR, M. L., STREETS, M. K., TRAVIN, A. K., AND SPALART, P. R. Turbulence modeling in rotating and curved channels: Assessing the spalart-shur correction. *AIAA j. 38*, 5 (2000), 784–792.

[64] SLOMSKI, J. F., AND GORSKI, J. J. Numerical simulation of circulation control airfoils as affected by turbulence models. In *40th Aerospace Sciences Meeting and Exhibit* (January 2002), AIAA, Ed.

[65] TELIONIS, D. P. Calculations of time-dependent boundary layers. *Symposium on Unsteady Aerodynamic* (1075), 115–190.

[66] THOMPSON, J. F., AND WEATHERILL, N. P. Aspects of numerical grids generation: Current science and art. *AIAA 93*, 3539 (1993).

[67] TOTAH, J. A critical assessment of the uh-60 main rotor blade airfoil data. In *11th AIAA Applied Aerodynamics Conference* (August 1993).

[68] W. Geissler, H. H. Investigation of dynamic stall onset. Tech. rep., German Aerospace Centre (DLR), 2006.

[69] Wang, S., Ingham, D. B., Ma, L., Pourkashanian, M., and Tao, Z. Numerical investigations on dynamic stall of low reynolds number flow around oscillating airfoils. *Elsevier online journal* (May 2010).

[70] Wilcox, D. C. *Turbulence Modeling for CFD.* DCW Industries, Inc., 1994.